

**Development of a Flexural Yielding Energy Dissipation Device for Controlled
Rocking Masonry Walls**

By

Jeff (Jie Fei) Li

B. Eng., E.I.T.

A Thesis Submitted to the School of Graduate Studies

in Partial Fulfillment of the Requirements

For the Degree of Master of Applied Science

McMaster University

© Copyright by Jeff Li

September 2019

MASTER OF APPLIED SCIENCE (2019)

McMaster University

(CIVIL ENGINEERING)

Hamilton, Ontario

Title: Development of a Flexural Yielding Energy
Dissipation Device for Controlled Rocking Masonry
Walls

Author: Jeff (Jie Fei) Li, B. Eng. (McMaster University)

Supervisors: Dr. Lydell Wiebe
Dr. Mohamed Ezzeldin

Number of pages: xviii, 129

Lay Abstract

Controlled rocking masonry walls can be a cost-efficient alternative to traditional masonry shear walls because of their enhanced performance, specifically to reduce and localize structural damage induced by seismic loads. However, a controlled rocking wall requires additional energy dissipation devices or post-tensioning techniques to compliment the rocking wall to achieve the desired performance.

This thesis explores and improves a type of energy dissipation device for controlled rocking masonry walls and aims to provide detailed design specifications for professional engineers. A design and considerations from previous studies are discussed, followed by the experimental validation, and finally new design equations are proposed for this type of reliable, flexural energy dissipation device.

Abstract

Steel flexural yielding arms can be an effective energy dissipation device for several seismic force resisting systems, including controlled rocking masonry walls. In controlled rocking masonry walls, uplift of the wall from the foundation is allowed in a way that can localize damage and minimize post-earthquake residual drifts. However, along with other modes of failure, sliding of the rocking walls can increase drifts and damage if not adequately addressed. Controlled rocking systems have different alternatives to prevent sliding, which include the use of additional mechanical components (e.g. metal stoppers) at the corners to resist lateral forces while allowing the wall rocking motion. However, these mechanical components hinder the constructability of the wall in some cases. The use of an energy dissipation device (i.e. steel flexural yielding arm) to also prevent the wall sliding mechanism has not been fully explored to date. The development of an easily replaceable energy dissipation device with the ability to simultaneously resist sliding demands is expected to maintain the overall performance of controlled rocking masonry walls, while also enhancing post-earthquake repairability.

The objective of the current study is to experimentally investigate the effect of axial forces on the behaviour of steel flexural yielding arms under cyclic loading. In this respect, the study first presents a description of the experimental program, test setup, and instrumentation. Next, the experimental results of the tested specimens are discussed in terms of the effect of axial forces on the load, displacement, and energy dissipation capacities of the tested devices. Finally, new design equations that account for axial forces are proposed and verified against the experimental data along with a finite element model.

Based on the results, recommendations are given for the further development of externally attached and replaceable flexural yielding arms for controlled rocking masonry walls.

Keywords: Controlled Rocking Masonry Walls; Energy Dissipation Device; Flexural Yielding; Seismic Design; Base Shear.

Acknowledgements

First, I would like to thank my parents, my mom, my dad, my brother and my sister for always supporting me. I am grateful to you for everything that I have. Second, I would like to express my gratitude to my supervisor, Dr. Lydell Wiebe, for all his guidance and teachings in the final year of my bachelor's degree and throughout my master's degree.

I am also thankful for Dr. Mohamed Ezzeldin, who was a tremendous influence assisting me throughout my graduate career. I would also like to thank Paul Heerema and Kent Wheeler, for everything that I have learned, needed, and more at my time in the ADL. This would not have been possible without you. In addition, I want to thank my peers, and all the staff and Faculty who have contributed to my memories and lessons here at McMaster. In particular, the seismic design team that sparked my interests as an earthquake engineer and my lunch peers at the ADL. It would not have been the same without you.

The most special thank you goes to my partner Alice, for her love, support, time and encouragement. Thank you for being there every step of the way. I am the most indebted to you.

Finally, I would like to acknowledge the financial support I received from the Department of Civil Engineering and the Canadian Masonry Design Centre, for providing me with this opportunity.

Table of Contents

1	Introduction.....	1
1.1	Behaviour of CRMWs with EDDs.....	2
1.2	Literature Review – EDDs for Controlled Rocking Systems	5
1.3	Objective of Current Study	12
2	Device Description.....	14
2.1	Device Parameters and Boundary Conditions.....	14
2.2	Design Considerations.....	15
2.3	Design Equations.....	17
2.4	Design Equations with Axial Load	19
2.5	Preliminary Design.....	20
3	Experimental Program	22
3.1	Description of Specimens.....	22
3.2	Test Setup.....	23
3.3	Instrumentation.....	26
3.4	Loading Protocol – Displacement Protocol	26
3.5	Loading Protocol – Axial Compression Protocol	26
3.6	Damage Sequence	28
3.6.1	Damage Sequence in <i>Phase I</i>	29

3.6.2	Damage Sequence in <i>Phase II</i>	32
3.6.3	Test Observations for All Specimens	35
3.7	Qualitative Discussion of Observations – Experimental Data	36
3.7.1	Qualitative Discussion of Observations – Forces in <i>Phase I</i>	40
3.7.2	Qualitative Discussion of Observations – Forces in <i>Phase II</i>	41
3.7.3	Qualitative Discussion of Observations – Displacements in <i>Phase I</i>	42
3.7.4	Qualitative Discussion of Observations – Displacements in <i>Phase II</i>	43
3.8	Quantitative Discussion of Test Results – Forces and Displacements	44
3.8.1	Quantitative Discussion of Test Results - Forces in <i>Phase I</i>	44
3.8.2	Quantitative Discussion of Test Results – Forces in <i>Phase II</i>	45
3.8.3	Quantitative Discussion of Test Results – Displacements in <i>Phase I</i>	45
3.8.4	Quantitative Discussion of Test Results – Displacements in <i>Phase II</i>	45
3.9	Discussion of Test Results - Design Parameters	46
3.9.1	Effect of L	46
3.9.2	Effect of b/t	48
3.10	Quantitative Discussion of Test Results – Energy Dissipation Capacities	50
3.11	New Proposed Design Equations for Strength	53
4	Numerical Modeling	56
4.1	Description of the Model	56

4.2	Discussion of Analytical Results.....	58
5	Conclusions.....	67
5.1	Performance of Flexural Arms without Axial Loads.....	67
5.2	Performance of Flexural Arms with Axial Loads.....	68
5.3	Force Capacity of Flexural Arms.....	68
5.4	Displacement Capacity of Flexural Arms.....	70
5.5	Future Research Recommendations.....	71
5.5.1	Maximum Actuator Displacement.....	72
5.5.2	Empirical Estimates of Displacement Capacity.....	72
5.5.3	Theoretical Estimates of Displacement Capacity.....	72
5.5.4	Axial Compression Force.....	73
5.5.5	Design Equations.....	73
5.5.6	Numerical Modeling.....	73
6	References.....	75
	Appendix A – Coupon Test Data.....	80
	Appendix B – Material Model in ABAQUS.....	95
	Appendix C – Reference Wall from Yassin.....	97
	Appendix D – Damage Sequence of All Specimens.....	98
	Appendix E – Strain Gauge Data.....	111

Appendix F – Sample Derivations – Phase I	118
Appendix G – Sample Derivations – Phase II	120
Appendix H – Full Cyclic FEA Hysteresis Loops	122
Appendix I – Numerical Approximate of the <i>Phase II</i> Yield Location.....	129

List of Figures

Figure 1 - Hysteretic Responses: (a) Conventional Fixed Base Wall; (b) Rocking with Post-tensioning and/or EDDs (Holden et al., 2002).....	2
Figure 2 – Detailed Hysteretic Response of a Rocking Wall with Dissipators (Toranzo et al., 2004)	4
Figure 3 - Force-Strain Characteristics of an Axial Dissipator (Restrepo and Rahman, 2007)	6
Figure 4 - Axial BRB; (a) Only Dissipator Front and Side View; (b) In Case Front, Side and Top View; (c) Load-Deformation Response (Toranzo, 2002).....	6
Figure 5 –(a) (b) Two Designs of Cantilever Arms and Their Load-Displacement Responses; (c) Cantilever Arms when Installed in the Rocking Wall (Toranzo, 2002).....	8
Figure 6 - Steel Slit Damper; (a) Specimen Section Parallel to Loading Direction; (b) Specimen Section Parallel to Loading Direction; (c) Load-Displacement Response (Chan and Albermani, 2008)	9
Figure 7 - Comb Teeth Damper; (a) Specimen Section Parallel to Loading Direction; (b) Load-Displacement Response (Garivani et al., 2016)	9
Figure 8 - Butterfly Fuse;(a) Specimen Section Parallel to Loading Direction;(b) Load-Displacement Response (Ma et al., 2010)	10
Figure 9 - ADAS Device; (a) Specimen Section Perpendicular to Loading Direction; (b) Specimen Section Parallel to Loading Direction; (c) Load-Deformation Response (Aiken et al., 1993)	11

Figure 10 - TADAS Device; (a) Deformation of Device to Lateral Loads; (b) Specimen Section Perpendicular to Loading Direction; (c) Load-Deformation Response (Saeedi et al., 2017)	11
Figure 11 - Masonry Rocking Wall with Flexural Arm Attached from Foundation Plate	15
Figure 12 - Flexural Arm with Parameters	15
Figure 13 - Example Design Detail of a Flexural Arm.....	21
Figure 14 - Test Setup and Instrumentation.....	24
Figure 15 - Photo of Test Setup	24
Figure 16 - Photo of Test Setup During Testing.....	25
Figure 17 – Displacement Loading Protocol	28
Figure 18 - Photos of specimen SL-L1-6.0.....	31
Figure 19 - Progression on Yielding on Specimen L-L1.2-6.0.....	32
Figure 20 - Photos of specimen SL-L1-6.0A.....	35
Figure 21 - Test Photos of Specimen S-L1-7.5A: (a) Local Buckling (34 mm); (b) Global Buckling (47 mm); (c) Failure (47 mm)	35
Figure 22 - Experimental Load Displacement Loops for Aspect Ratio.....	38
Figure 23 - Experimental Load Displacement Loops for Length	39
Figure 24 - Cumulative Energy Dissipated per Volume of Yielding Steel to Aspect Ratio and L	50
Figure 25 - Cumulative Displacement at Failure to Aspect Ratio and L.....	51
Figure 26 - Meshing Details for the Flexural Device in ABAQUS.....	56

Figure 27 - Buckling Shape of SL-L1-6.0A; (a) Experimental (90 mm); (b) ABAQUS Result (90 mm)	57
Figure 28 - Buckling Shape of L-L0.8-6.0; (a) Experimental (90 mm); (b) ABAQUS Result (90 mm).....	57
Figure 29 - Hysteresis Plots for S-L1-7.5 and S-L1-7.5A	60
Figure 30 - Hysteresis Plots for SL-L1-6.0 and SL-L1-6.0A	61
Figure 31 - Hysteresis Plots for S-L1-5 and S-L1-5A	62
Figure 32 - Hysteresis Plots for S-L1-4.3 and S-L1-4.3A	63
Figure 33 - Hysteresis Plots for L-L0.8-6.0 and L-L0.8-6.0A.....	64
Figure 34 - Hysteresis Plots for L-L1.2-6.0 and L-L1.2-6.0A.....	65
Figure 35 - Hysteresis Plots for L-L1.4-6.0 and L-L1.4-6.0A.....	66
Figure 36 - Stress-Strain Curve for S-L1-7.5.....	81
Figure 37 - Stress-Strain Curve for S-L1-7.5.....	81
Figure 38 - Stress-Strain Curve for S-L1-7.5A.....	82
Figure 39 - Stress-Strain Curve for S-L1-7.5A.....	82
Figure 40 - Stress-Strain Curve for SL-L1-6.0	83
Figure 41 - Stress-Strain Curve for SL-L1-6.0	83
Figure 42 - Stress-Strain Curve for SL-L1-6.0A	84
Figure 43 - Stress-Strain Curve for SL-L1-6.0A	84
Figure 44 - Stress-Strain Curve for S-L1-5.0.....	85
Figure 45 - Stress-Strain Curve for S-L1-5.0.....	85
Figure 46 - Stress-Strain Curve for S-L1-5.0A.....	86

Figure 47 - Stress-Strain Curve for S-L1-5.0A.....	86
Figure 48 - Stress-Strain Curve for S-L1-4.3.....	87
Figure 49 - Stress-Strain Curve for S-L1-4.3.....	87
Figure 50 - Stress-Strain Curve for S-L1-4.3A.....	88
Figure 51 - Stress-Strain Curve for S-L1-4.3A.....	88
Figure 52 - Stress-Strain Curve for L-L0.8-6.0	89
Figure 53 - Stress-Strain Curve for L-L0.8-6.0	89
Figure 54 - Stress-Strain Curve for L-L0.8-6.0A	90
Figure 55 - Stress-Strain Curve for L-L0.8-6.0A	90
Figure 56 - Stress-Strain Curve for L-L1.2-6.0	91
Figure 57 - Stress-Strain Curve for L-L1.2-6.0	91
Figure 58 - Stress-Strain Curve for L-L1.2-6.0A	92
Figure 59 - Stress-Strain Curve for L-L1.2-6.0A	92
Figure 60 - Stress-Strain Curve for L-L1.4-6.0	93
Figure 61 - Stress-Strain Curve for L-L1.4-6.0	93
Figure 62 - Stress-Strain Curve for L-L1.4-6.0A	94
Figure 63 - Stress-Strain Curve for L-L1.4-6.0A	94
Figure 64 - ABAQUS Material Properties Curve Fitting using Coupon Test Data	95
Figure 65- ABAQUS Material Properties Curve Fitting using Coupon Test Data	96
Figure 66 - Sample Calculations for Reference Wall	97
Figure 67 - Test Photos of S-L1-7.5	98
Figure 68 - Test Photos of S-L1-7.5A	99

Figure 69 - Test Photos of S-L1-6.0	100
Figure 70 - Test Photos of S-L1-6.0A	101
Figure 71 - Test Photos of S-L1-5	102
Figure 72 - Test Photos of S-L1-5A	103
Figure 73 - Test Photos of S-L1-4.3	104
Figure 74 - Test Photos of S-L1-4.3A	105
Figure 75 - Test Photos of L-L0.8-6.0	106
Figure 76 - Test Photos of L-L1.2-6.0	107
Figure 77 - Test Photos of L-L1.2-6.0A	108
Figure 78 - Test Photos of L-L1.4-6.0	109
Figure 79 - Test Photos of L-L1.4-6.0A	110
Figure 80 - SG Data for S-L1-7.5 and S-L1-7.5A	111
Figure 81 - SG Data for SL-L1-6.0 and SL-L1-6.0A	112
Figure 82 - SG Data for S-L1-5.0 and S-L1-5.0A	113
Figure 83 - SG Data for S-L1-4.3 and S-L1-4.3A	114
Figure 84 - SG Data for L-L0.8-6.0	115
Figure 85 - SG Data for L-L1.2-6.0 and L-L1.2-6.0A	116
Figure 86 - SG Data for L-L1.4-6.0 and L-L1.4-6.0A	117
Figure 87 - Hysteresis Plots for S-L1-7.5 and S-L1-7.5A	122
Figure 88 - Hysteresis Plots for SL-L1-6.0 and SL-L1-6.0A	123
Figure 89 - Hysteresis Plots for S-L1-5 and S-L1-5A	124
Figure 90 - Hysteresis Plots for S-L1-4.3 and S-L1-4.3A	125

Figure 91 - Hysteresis Plots for L-L0.8-6.0 and L-L0.8-6.0A..... 126

Figure 92 - Hysteresis Plots for L-L1.2-6.0 and L-L1.2-6.0A..... 127

Figure 93 - Hysteresis Plots for L-L1.4-6.0 and L-L1.4-6.0A..... 128

Figure 94 - Approximate Plot of Location of Maximum Bending Stress..... 129

List of Tables

Table 1 - Test Matrix with Geometric Parameters and Mean Coupon Test Data.....	23
Table 2 - Test Matrix with Results	37
Table 3 - Comparison of Engineering Parameters in Phase II, Expressed in Percentages of Phase I Performance.....	46
Table 4 - Summary of Performances for all Specimens	48
Table 5 - Summary of Proposed Changes to Force Design Equations	54
Table 6 - Material Test Data	80

List of Acronyms

ADAS – Added Damping and Stiffness

BRB – Buckling Restrained Brace

CRMW – Controlled Rocking Masonry Wall

EDD – Energy Dissipation Device

LVDT – Linear Variable Differential Transformer

SG – Strain Gauge

TADAS – Triangular Added Damping and Stiffness

List of Symbols

A	cross section of yielding fuse at $x = 0.5L$
a	width of yielding fuse (at $x = 1.0L$)
b	width of yielding fuse (at $x = 0L$)
E	Young's modulus of steel
h	distance from bolt hole to fuse link start
I	second moment of inertia
L	length of yielding fuse
M_y	yield moment of fuse cross-section
M_p	plastic moment of fuse cross-section
P	axial force
Q_y	fuse yield strength
Q_p	fuse peak strength
t	thickness of fuse plate
w	width of section
Δ	displacement of actuator
Δ_y	yield displacement
σ_y	yield stress
σ_u	ultimate stress

1 Introduction

Several research studies have been conducted to enhance the seismic performance of conventional masonry walls (i.e. with fixed base) in the last decades (e.g., Sveinsson et al., 1985; Matsumura, 1986; Kaminosono et al., 1988; Shing et al., 1990; Voon and Ingham, 2006; Seif Eldin and Galal, 2017; Ezzeldin et al. 2017). However, these walls are being limited in their seismic applications due to the extensive damage observed following seismic events (EERI, 2005). Fig. 1a presents the typical hysteretic response of a conventional fixed base wall as cracks form in the tensile regions of the wall when subjected to lateral loadings, leading to damage. To address this, recent studies have demonstrated that controlled rocking masonry walls (CRMWs) with energy dissipation devices (EDDs) and/or post-tensioning strands can be an effective and economic alternative to replace conventional masonry walls (e.g., Toranzo, 2002; Toranzo et al., 2004; Laursen and Ingham, 2004; Chancellor et al., 2014). This is mainly due to the unique ability of CRMWs to uplift from their foundation when subjected to lateral loads, creating a “flag-shaped” hysteresis, as shown in Fig. 1b and discussed in more detail subsequently in Section 1.1. In general, the controlled rocking mechanism yields a seismic force resisting system with high self-centering ability and low residual drifts, thus minimizing damage during seismic events.

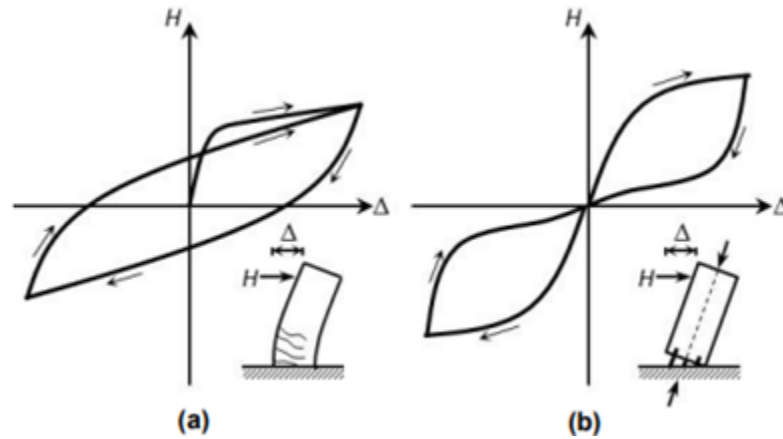


Figure 1 - Hysteretic Responses: (a) Conventional Fixed Base Wall; (b) Rocking with Post-tensioning and/or EDDs (Holden et al., 2002)

1.1 Behaviour of CRMWs with EDDs

Figure 2 shows the progression of the hysteretic response of a rocking wall using EDDs (Toranzo et al., 2004). As seen in Fig. 2 (step 1), free rocking walls (without post-tensioning strands or EDDs) are associated with limited overturning moment resistance and hysteretic energy dissipation capacity. Therefore, a rocking system relies primarily on supplemental EDDs and/or post-tensioning strands to control lateral drifts and minimize structural damage (Makris and Roussos, 1998; Priestley et al., 1999; Holden et al., 2002; Laursen and Ingham, 2004; Toranzo et al., 2004; Restrepo and Rahman, 2007). This behaviour is depicted first by Fig. 2 (step 2, 3, and 4), as the rocking wall starts to uplift (rocking motion) when the overturning moment demand becomes higher than the overturning moment resistance created due to gravity loads. During this stage (decompression) is when the dissipators are engaged due to the imposed displacement demand caused by the wall uplift. Since the uplift displacement is governed by the overturning moment resistance, the additional overturning moment resistance from EDDs can be used to directly control lateral drifts, similar to a stiff spring (Fig. 2 (step 4, 5, and 6)). Furthermore, as shown in Fig. 2

(step 7, 8, and 9), EDDs can also minimize impact action during unloading as the wall needs to yield the dissipator back to its initial condition shown in Fig. 2 (step 10). In general, the use of replaceable EDDs is favored due to their ease of replaceability after a seismic event, thus complimenting the enhanced performance that can be achieved when such rocking systems are adopted (Vargas and Bruneau, 2006).

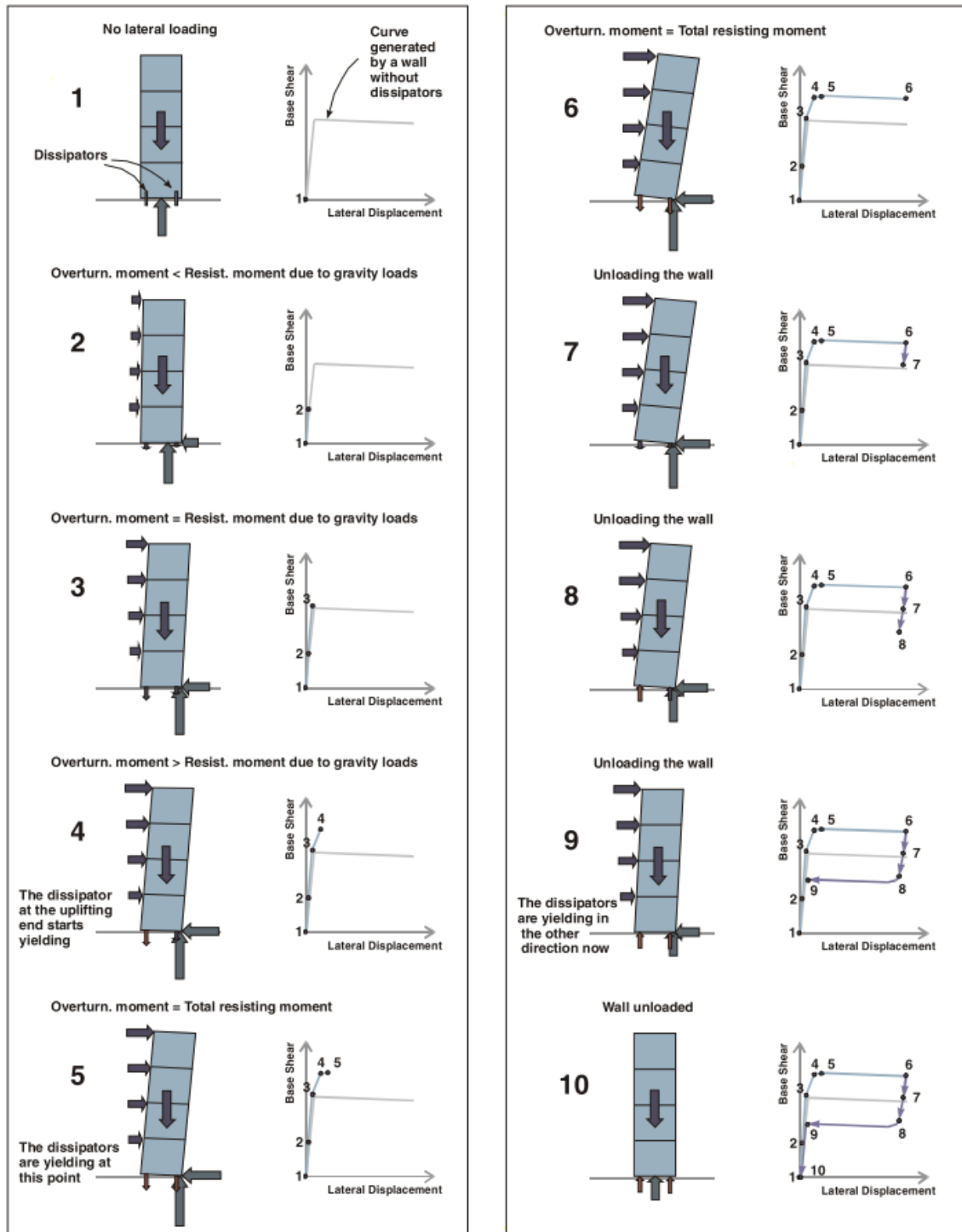


Figure 2 – Detailed Hysteretic Response of a Rocking Wall with Dissipators (Toranzo et al., 2004)

1.2 Literature Review – EDDs for Controlled Rocking Systems

Several EDDs with adequate ductility and energy dissipation capacities are currently available; however, to date, a limited number of devices have been investigated and adopted for rocking walls. One of the main EDDs comes in the form of a steel axial yielding bars anchored at the base of the walls, as shown in Fig. 3 (Holden et al., 2002; Laursen and Ingham, 2004; Restrepo and Rahman, 2007). As can be seen in the figure, these axial yielding devices are typically made with tapered reinforcement bars to ensure their yielding in a well-defined region, but they are still prone to unexpected fractures at high displacement demands (Holden et al., 2002; Laursen and Ingham, 2004; Restrepo and Rahman, 2007). In general, these studies demonstrated that steel axial devices performed well to achieve “flag-shaped” hysteretic response by adding supplemental damping to the controlled rocking wall; however, due to the embedded nature of these devices, they cannot be assessed or replaced if severely damaged following a seismic event. To address this, Toranzo (2002) adopted an externally attached version in the form of a miniature buckling restrained brace (BRB), but the device was unable to sustain the desired deformations without unintended buckling. As seen in Fig. 4, this led to unpredictable response in the compression region caused by the development of large friction forces between the body of the steel dissipator and the grout in the case (Toranzo, 2002).

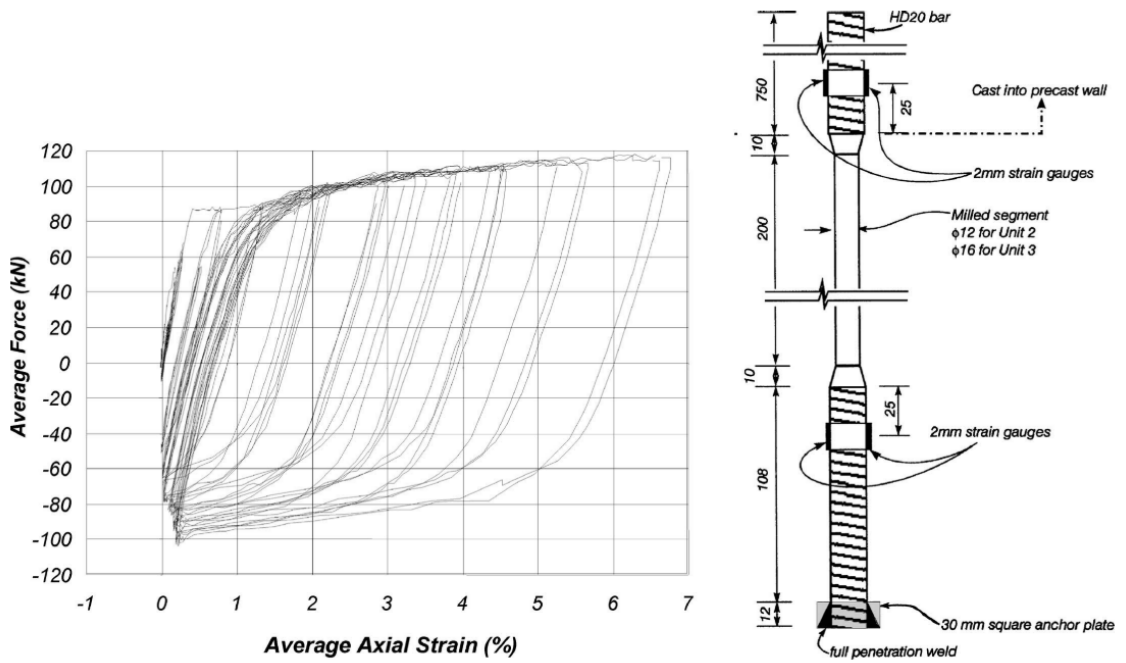


Figure 3 - Force-Strain Characteristics of an Axial Dissipator (Restrepo and Rahman, 2007)

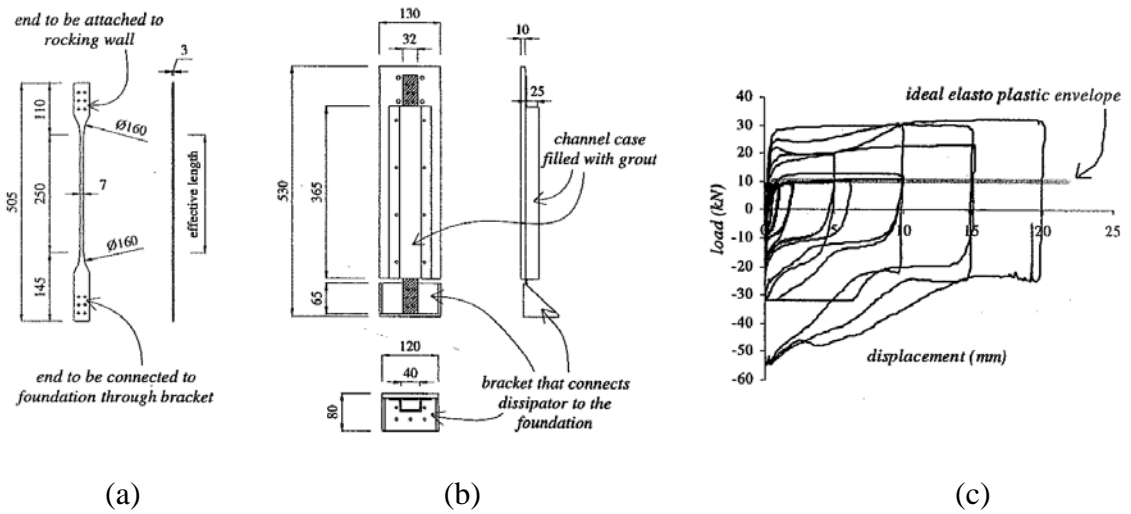
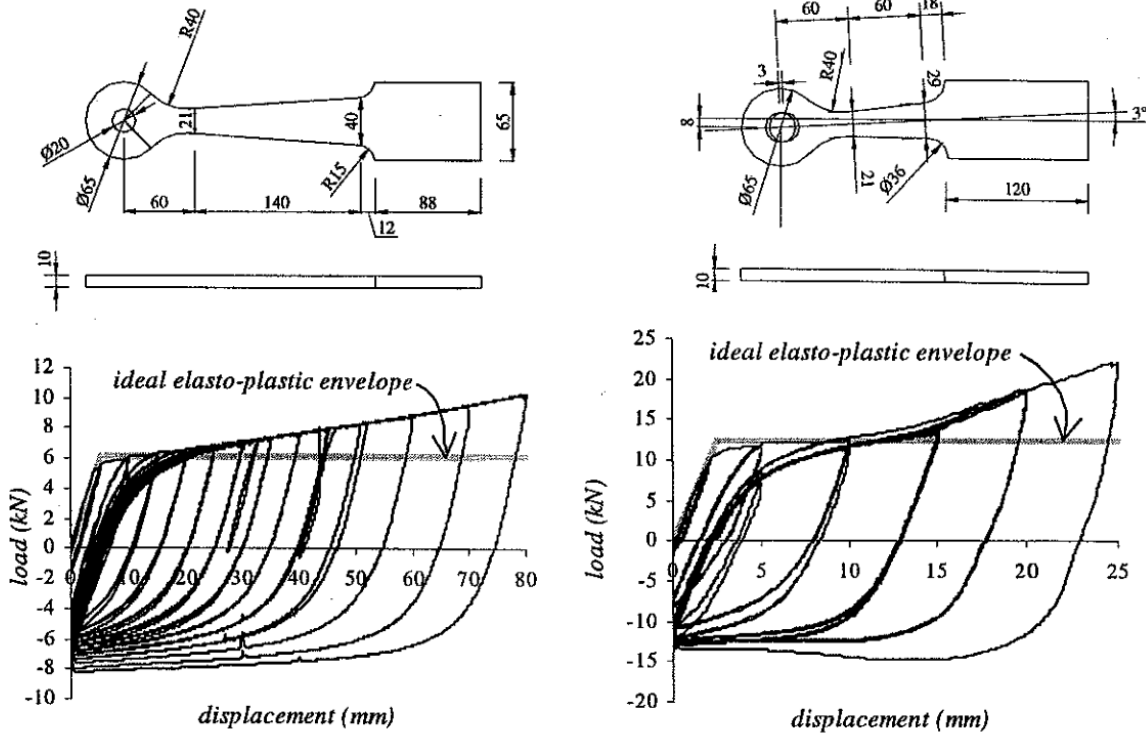


Figure 4 - Axial BRB; (a) Only Dissipator Front and Side View; (b) In Case Front, Side and Top View; (c) Load-Deformation Response (Toranzo, 2002)

On the other hand, few studies have explored the viability of external attached steel cantilever arms, shown in Fig. 5, as EDDs in rocking walls (Toranzo, 2002; Toranzo et al.,

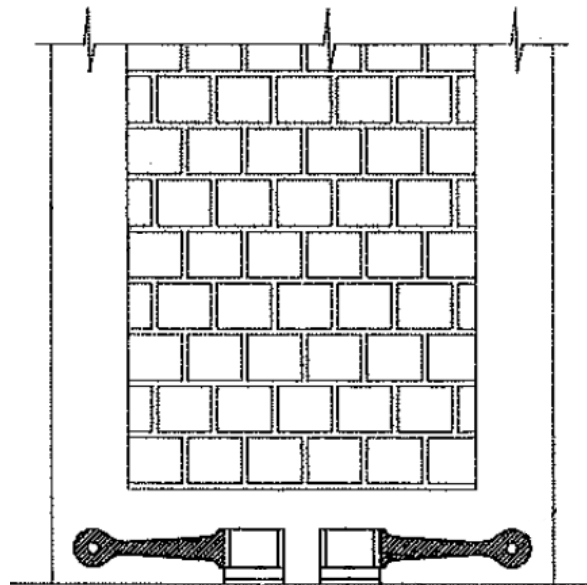
2009). In these previous studies, two cantilever arm designs were proposed and validated under quasi-static cyclic loading, before they were tested in a rocking wall under dynamic loading (Toranzo, 2002). In addition to their ease of accessibility and repairability following a seismic event, the experimental results showed that steel cantilever arms can achieve reliable performance with no complications. Furthermore, the planar geometry of the cantilever arms makes them more suitable for space-constrained applications (Ma et al., 2010). The pure flexural yielding behaviour of such arms was also observed to be more reliable than that of steel axial yielding bars in medium to large displacement cycles. However, the design requirements of these cantilever arms were not clearly outlined, and no guidance was represented regarding the influence of critical geometric parameters on the performance of such arms (Toranzo, 2002).

Although limited research has been conducted on steel cantilever arms as EDDs, many studies on other flexural yielding devices have demonstrated the effect of different parameters on the overall performance (e.g., Chan and Albermani, 2008; Ma et al., 2010; Garivani et al., 2016). For example, as shown in Figs. 6, 7 and 8, steel slit dampers, comb-teeth dampers, and butterfly fuses were also designed to yield uniformly through the configurations of triangular/rectangular/parabolic steel plates when subjected to strong-axis bending (Chan and Albermani, 2008; Ma et al., 2010; Garivani et al., 2016). However, these previous studies focused on in-plane assemblies of multiple smaller links, which may not be feasible in further space-constrained applications.



a)

b)



c)

Figure 5 –(a) (b) Two Designs of Cantilever Arms and Their Load-Displacement Responses; (c) Cantilever Arms when Installed in the Rocking Wall (Toranzo, 2002)

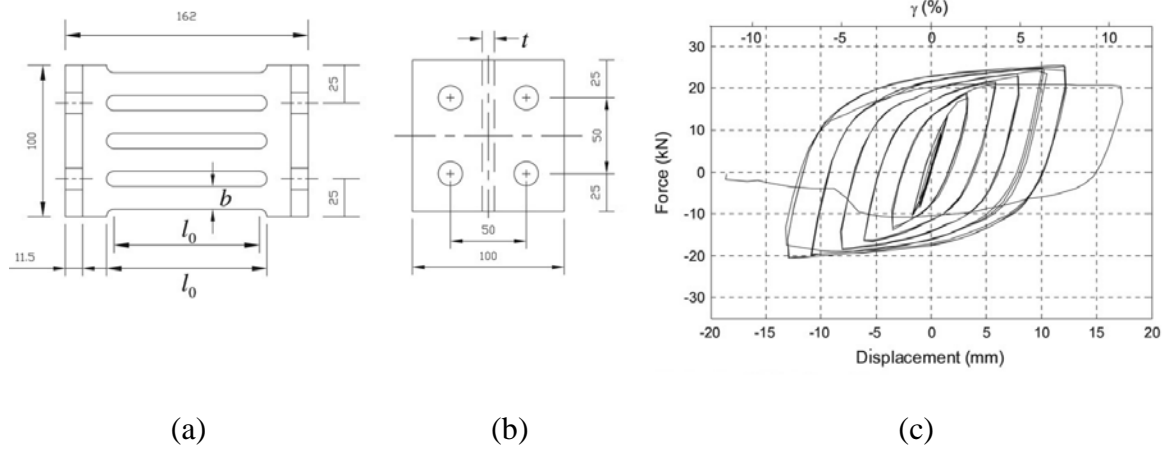


Figure 6 - Steel Slit Damper; (a) Specimen Section Parallel to Loading Direction; (b) Specimen Section Parallel to Loading Direction; (c) Load-Displacement Response (Chan and Albermani, 2008)

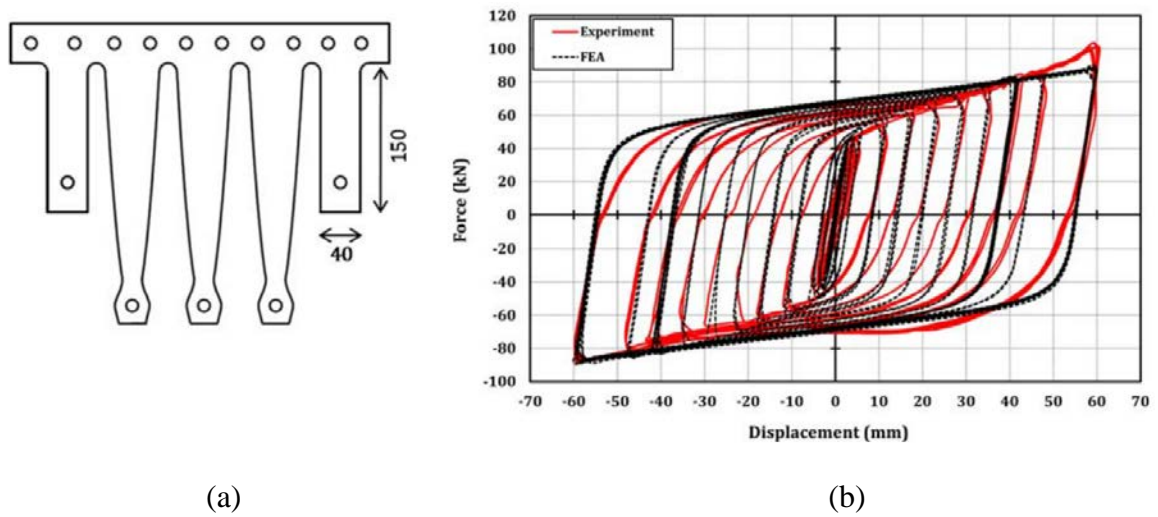


Figure 7 - Comb Teeth Damper; (a) Specimen Section Parallel to Loading Direction; (b) Load-Displacement Response (Garivani et al., 2016)

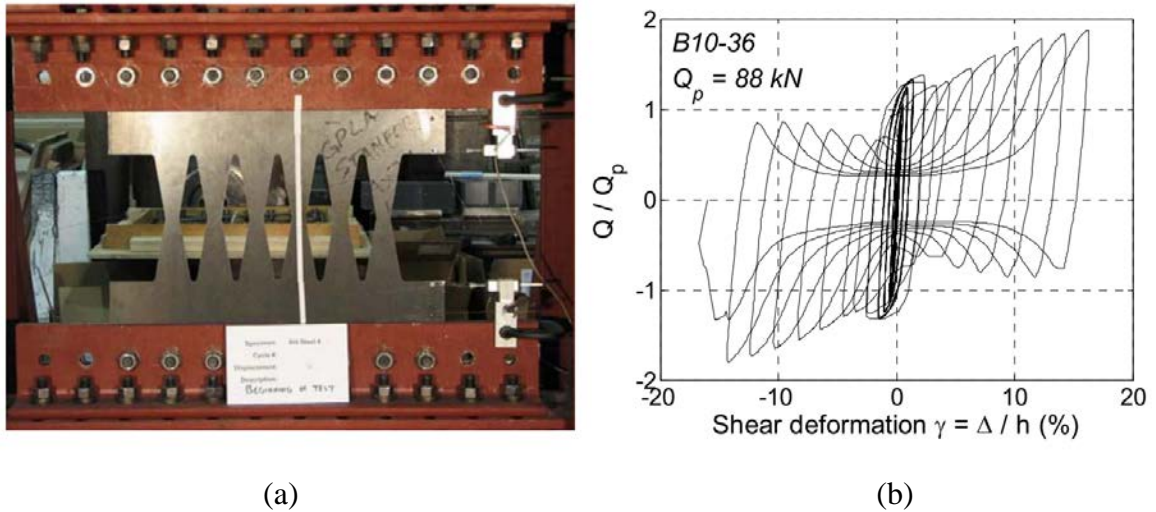


Figure 8 - Butterfly Fuse;(a) Specimen Section Parallel to Loading Direction;(b) Load-Displacement Response (Ma et al., 2010)

Alternatively, as shown in Figs. 9 and 10, added damping and stiffness (ADAS) and triangular-ADAS (TADAS) devices were designed to yield uniformly throughout the assemblies of X or triangle steel plates when subjected to weak-axis bending (Bergman and Goel, 1987; Xia and Hanson 1992; Aiken et al., 1993; Tsai et al., 1993; Garivani et al., 2016; Saeedi et al., 2017). Numerous previous studies have demonstrated that triangular-like configurations were superior to other configurations by facilitating a more uniform distribution of yielding, thus minimizing stress concentrations (Bergman and Goel, 1987; Kobori et al., 1992; Xia and Hanson 1992; Tsai et al., 1993; Chan and Albermani, 2008; Ma et al., 2010; Garivani et al., 2016). In general, such flexural devices showed high ductility and energy dissipation capacities, however, they were constrained by space due to their large assembly sizes.

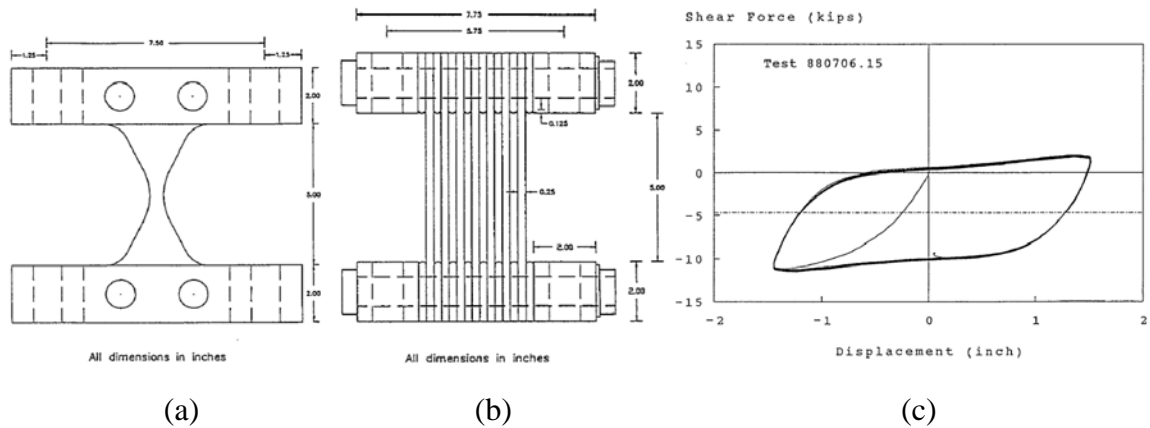


Figure 9 - ADAS Device; (a) Specimen Section Perpendicular to Loading Direction; (b) Specimen Section Parallel to Loading Direction; (c) Load-Deformation Response (Aiken et al., 1993)

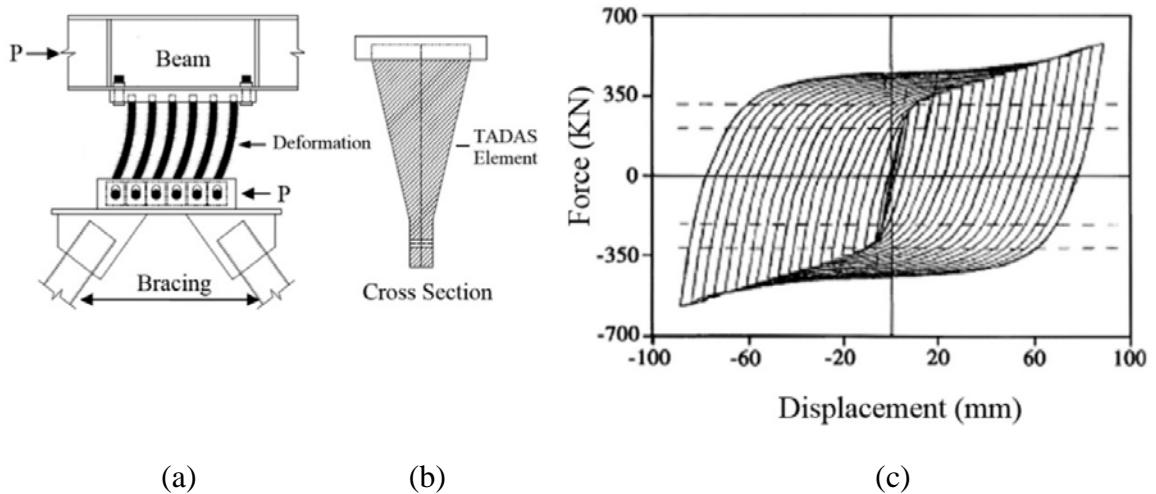


Figure 10 - TADAS Device; (a) Deformation of Device to Lateral Loads; (b) Specimen Section Perpendicular to Loading Direction; (c) Load-Deformation Response (Saeedi et al., 2017)

In general, strong-axis flexural yielding devices are stiffer than their weak-axis counterparts due to the corresponding bending mechanisms, thus leading to higher energy dissipation capabilities. In addition, both types of flexural devices can be designed to align their moment capacities with the shape of the moment diagram, possibly leading to a uniform yielding pattern and reduced inelastic stress concentrations; however, the strong-

axis devices were vulnerable to buckling at high displacement demands (Bergman and Goel, 1987; Xia and Hanson 1992; Tsai et al., 1993; Toranzo, 2002; Toranzo, 2009; Ma et al., 2010; Garivani et al., 2016).

1.3 Objective of Current Study

Although several configurations of flexural devices have been studied in the past, there is a lack of experimental and numerical data for the performance of simple tapered cantilever arms. Additionally, multiple studies have recommended that axial compression on flexural devices should be avoided by design to prevent premature buckling and consequently premature failure. Therefore, all previous studies did not include axial compression on their corresponding devices (Chan and Albermani, 2008; Ma et al., 2010; Garivani et al., 2016). As such, bridging such gaps is a necessary step to facilitate the adoption of these devices in rocking walls.

Therefore, the main objective of the current study is to experimentally and numerically investigate the behaviour of externally attached flexural (cantilever) arms, designed specifically for CRMWs, under both cyclic displacement and axial compression loadings simultaneously that simulate seismic demands. In this respect, the study first presents the device description and design considerations in Chapter 2. Next, Chapter 3 describes the experimental program and test setup, and provides information about the different configurations used to investigate the influence of arm length L , aspect ratio b/t , and axial compression force P . Afterwards, the experimental results of the tested arms are presented in terms of their corresponding load-displacement responses and energy dissipation capacities. Finally, mechanics-based equations (Chapter 3) and finite element

models are developed and validated against the experimental results presented in the current study (Chapter 4), before concluding remarks and recommendations in Chapter 5.

2 Device Description

2.1 Device Parameters and Boundary Conditions

Figure 11 shows the intended layout of a typical flexural arm device and its connection to a rocking masonry wall, while the key geometric parameters that influence the displacement and force capacities of the device are shown in Fig. 12. As can be seen in Fig. 11, the base of the arm is bolted to a plate that is fixed to the foundation, while the head of the arm is pinned to the wall. An example of similar detailing considerations can be found in Toranzo et al. (2009), but complete connection details are beyond the scope of the current study. In general, the flexural arm dissipates energy through strong-axis flexural yielding as the wall uplift imposes a shear displacement, Δ , leading to a reaction force/moment on the arm. The pinhead (pinned) and the bolt group (fixed) represent the boundary conditions of the flexural arm, thus governing the device behaviour associated with both global and local buckling modes. Unlike traditional rocking walls, which usually require additional mechanical stoppers to prevent their sliding, the current assembly allows for the flexural arm to resist all the base shear demands through the pin connection(s), which may provide more architectural flexibility.

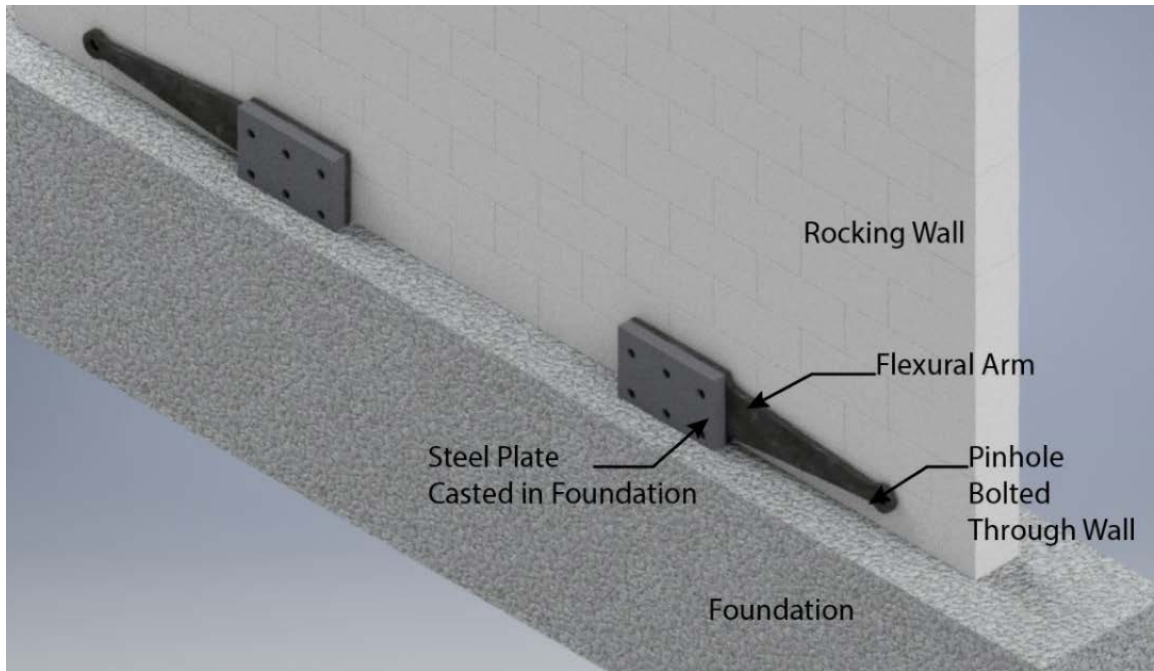


Figure 11 - Masonry Rocking Wall with Flexural Arm Attached from Foundation Plate

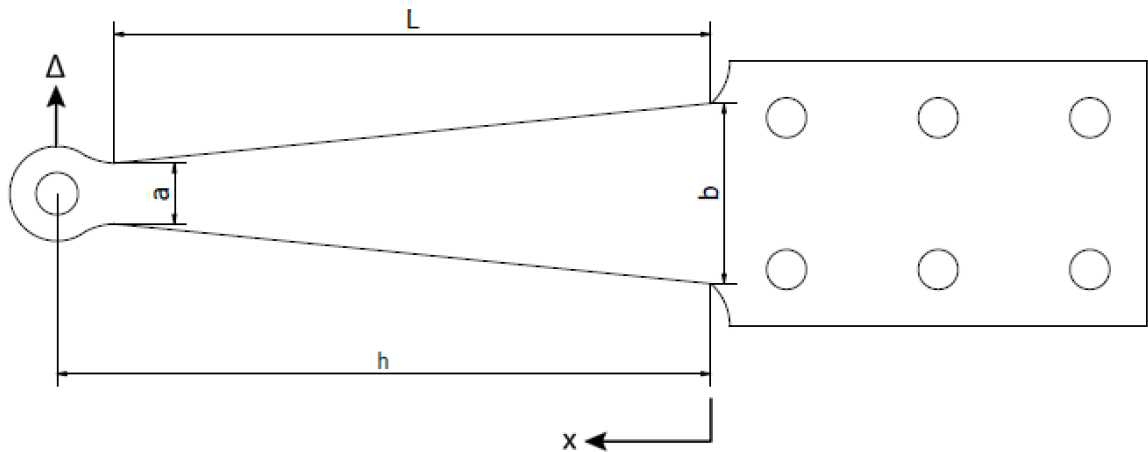


Figure 12 - Flexural Arm with Parameters

2.2 Design Considerations

As discussed in Chapter 1 and shown in Figs. 6, 7, and 8, devices similar to the flexural arm considered herein have been studied in the past but mainly in a series of multiple configurations (Chan and Albermani, 2008; Ma et al., 2010; Garivani et al., 2016; Kobori

et al., 2017). Experimental tests conducted by Kobori et al. (2017) and Ma et al. (2010) showed that if tapered flexural links made from thicker plates were geometrically proportioned to initiate yielding away from regions of curvature change, they are then capable of full hysteretic behaviour at larger displacements. In addition, Chan and Albermani (2008) also found that large plastic strain concentrations were the cause of specimen failure by fracture after loading cycles at large displacements. Lastly, Garivani et al. (2016) mentioned as well that it is crucial to detail the shape of the links to avoid unwanted stress concentrations (Chan and Albermani, 2008; Ma et al., 2010; Garivani et al., 2016; Kobori et al., 2017).

Therefore, since no full design guidelines have been established for the flexural arm, the initial design of the current device extrapolated the recommendations reported by these previous studies on similar strong-axis flexural devices. For example, designs which can result in plastic hinges closer to regions of curvature change (closer to a or b) should be generally avoided, unless detailed specifically. This is achieved by changing a and b values, which varies the point of maximum bending stress along the length of the yielding fuse (Ma et al., 2010). Previous studies have also shown that if the aspect ratio of the arm (b/t) is limited between 2 and 9, a stable hysteretic behaviour (i.e. before buckling initiation) can be achieved up to a shear deformation (Δ/L) of 30% (Chan and Albermani, 2008; Ma et al., 2010). Therefore, the aspect ratio of the arms tested in the current study was set to be around 6 as a median value to avoid any premature buckling failures. Note that, usually the term b/t is usually called slenderness, but it is referred to as aspect ratio hereafter in the

current study. Finally, since the current study aims at 3% drift of a model wall, the target displacement (47 mm) and yield force (22.5 kN) of the arm were calculated using trigonometry and equilibrium of forces, respectively, to achieve the desired wall overturning moment resistance at that drift (Yassin, personal communication, 2018). A figure of the reference wall can be found in Appendix C.

2.3 Design Equations

The geometry of the flexural arms considered in the current study resembles that of the cantilever arms tested by Toranzo (2002), as well as half of a single cut-out of the butterfly fuses designed by Ma et al. (2010) but with different boundary conditions. No specific design guidelines for displacement or force capacities were identified for cantilever arms, but Ma et al. (2010) proposed an optimal fuse shape, and derived strength and stiffness equations for the butterfly fuses based on the assumed flexural behaviour. Thus, similar procedures were first used to obtain the optimal fuse shape for the current device. More specifically, the desired location of the maximum bending stress (or the desired location of the plastic hinge formation) should be at $x = 0.5L$, away from regions of curvature change, thus results in a ratio $a/b = 1/3$. This a/b ratio was kept constant for all specimens in an effort to place the location of maximum bending stress at $x = 0.5L$. In addition, the flexural arm should be proportioned such that all points along the outer extreme fibre of the device yield simultaneously, based on the stress at the extreme fibre as defined in Equation (1). Ma et al. (2010) highlighted that although satisfaction of such relationship would result in the perfect simultaneous yielding in the way of an hourglass-shaped fuse with parabolic

edges, straight fuse edges were still selected to simplify the overall design and fabrication process.

$$\sigma(x) = \frac{M(x) w(x)/2}{I(x)} = \frac{\left(M_o \frac{x}{L}\right) \left(\frac{(b-a)x}{L} + a\right) / 2}{\frac{1}{12} \left(\left(\frac{(b-a)x}{L} + a\right)^3 t\right)} \quad (1)$$

where $M(x)$, $w(x)$, and $I(x)$ = bending moment, width and moment of inertia of a section, respectively, that is at distance x from the horizontal centerline of a device shown in Fig. 12. Therefore, Eq. (1) can be used to find the stress at the extreme fibre at any location along the length and subsequently determine the location and magnitude of the maximum bending stress. The yield and plastic strength prediction equations of the current devices are presented in Eqs. (2) and (3), respectively, but detailed derivations of these equations can be found in Ma et al. (2010). These strength equations serve to be one of the preliminary procedures on designing the current flexural device. More detailed derivation procedures can be found in Appendix F.

$$Q_{yt} = \frac{4}{27} \frac{b^2 t \sigma_y}{L} \quad (2)$$

$$Q_{pt} = \frac{6}{27} \frac{b^2 t \sigma_y}{L} \quad (3)$$

where b = width of fuse link start section, t = thickness of fuse plate, σ_y = yield stress of steel, and L = length of fuse link.

2.4 Design Equations with Axial Load

An approximate method was used to estimate the effects of axial load on the flexural arm output strength, as shown in Eqs. (4), (5) and (6). Careful considerations must be taken when using these equations as many assumptions were made to simplify the derivation and expedite the process, thus making it an approximate method. Aside from the derivation process, these equations first assume, that the additional axial stress would cause the flexural arm to yield first in the compression fibre by using a simple stress-profile. Second, the nominal plastic strength Q_{pt} ($= 1.5Q_y$) is assumed to be reached at $1.5\Delta_y$, where the yield displacements were obtained experimentally after the specimens tested in *Phase I*. More information about *Phase I* and *Phase II* will be discussed later in Chapter 3. Furthermore, the yielding location is assumed to stay the same at $x = 0.5L$ by keeping the ratio $a/b = 1/3$. These assumptions will be compared to experimental findings to check for its validity. More detailed derivation procedures can be found in Appendix G.

$$Q_{yt,axial} = \frac{4}{27} \frac{b^2 t \sigma_{y,a}}{L} - \frac{P \Delta_y}{L} \quad (4)$$

$$Q_{pt,axial} = \frac{6}{27} \frac{b^2 t \sigma_{y,a}}{L} - \frac{P 1.5\Delta_y}{L} \quad (5)$$

$$\sigma_a(x) = \frac{M(x)w(x)/2}{I(x)} + \frac{P}{w(x)t} \quad (6)$$

where b = width of fuse link start section, t = thickness of fuse plate, $\sigma_{y,a}$ = yield stress of steel including axial compression at $x = 0.5L$, L = length of fuse link, P = axial load, Δ_y = yield displacement, and A = cross section of yielding fuse at $x = 0.5L$.

2.5 Preliminary Design

Ma et al. (2010) showed that for an aspect ratio of $b/t = 6$, the in-plane flexural fuse could sustain a shear deformation (Δ/L) of 14% before buckling initiation. Therefore, the preliminary value for arm length ($L = 335$ mm) was determined by using 47 mm as the target displacement before buckling initiation for a flexural arm with an aspect ratio of $b/t = 6$. Furthermore, by using Eq. (2) and assuming grade 50W steel, the remaining geometric variables were determined ($b = 95$ mm, $a = 32$ mm, and $t = 15.875$ mm). All geometric values were rounded up or down to facilitate manufacturing, material acquisition, and force capacity. For example, this resulted in the adjustment of the arm length from 335 mm to 315 mm, to achieve the target yield strength requirement of 22.5 kN using Eq. (2), while satisfying all strength capacity checks and limiting areas of curvature change. Figure 13 shows the geometrical configurations of the control arm (i.e. specimen SL-L1-6.0), which was selected as the reference point for all other arms tested in the current study, as will be discussed in the following sections.

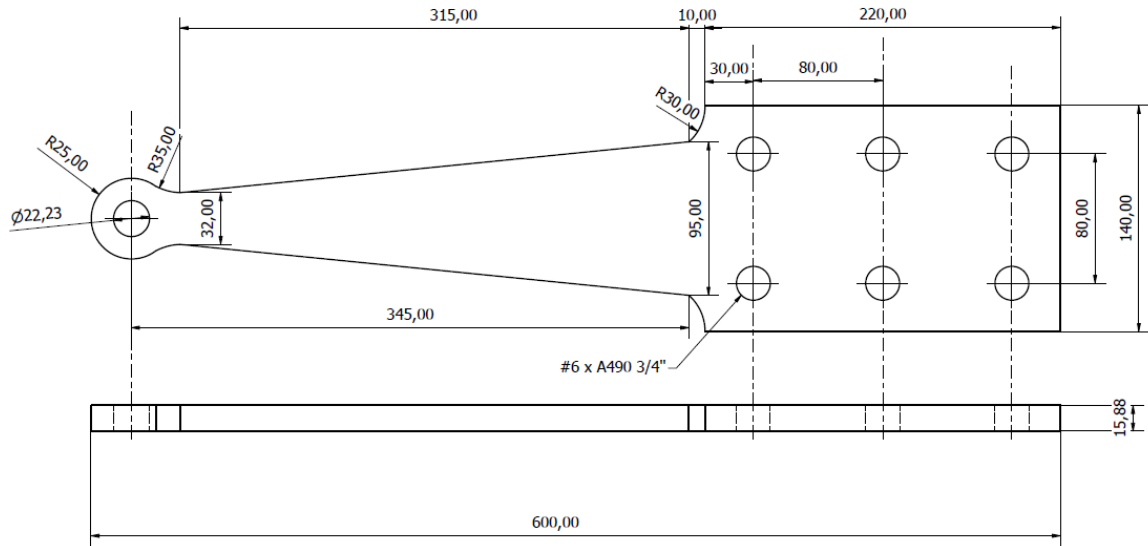


Figure 13 - Example Design Detail of a Flexural Arm

The pinhead and bolt group of the flexural arm were designed not to yield under the expected loads. As such, the pinhead was detailed primarily to resist bearing failure, net section fracture, and block shear. Meanwhile, the bolt group was mainly governed by bolt strength, imposed moment on the bolt group, bearing failure and bolt size/spacing. Overall, conservatism in strength was prioritized after using minimal geometric sizes to further propagate the advantage of using these flexural devices for space-constrained applications. Finally, the curvature of the transition areas between the pinhead, yielding portion, and bolt group were selected to reduce the effects of any abrupt curvature changes. This was recommended in previous studies to improve the ductility of the devices and minimize the likelihood of premature fracture by avoiding unintended formation of stress concentrations (Chan and Albermani, 2008; Ma et al., 2010; Garivani et al., 2016; Kobori et al., 2017).

3 Experimental Program

3.1 Description of Specimens

Fourteen half-scale steel flexural arms were tested under displacement controlled quasi-static fully-reversed cyclic loading. As can be seen in Table 1, the test matrix aims to investigate the influence of the aspect ratio, b/t , and arm length, L , either with or without axial compression loads, on the arm performance. These parameters were selected herein as they contributed the most to displacement and force capacities of similar devices as reported by Ma et al. (2010). The arms used to investigate the effects of the aspect ratio are identified with S as the first letter, while those used to investigate the effects of the arm length are denoted by L. The identification SL means that the same data point was used for both aspect ratio and length data sets. Similarly, A as the last letter indicates the presence of axial compression forces and corresponds to a respective axial compression stress at the cross-section of intended yielding/buckling ($x = 0.5L$). The tested arms were fabricated from 50W steel plates using water jet cutting technology to avoid residual stresses caused by heat cutting methods. In addition, from each plate, two coupons were cut and used for uniaxial tests in accordance with ASTM Standard E8 (ASTM, 2003) and the results are summarized in Table 1, and full coupon test data can be found in Appendix A. Finally, all specimens in both S and L series were tested first without axial compression forces in *Phase I*, while specimens in *Phase II* were tested with axial compression force as will be explained in more detail in Section 3.4.

Table 1 - Test Matrix with Geometric Parameters and Mean Coupon Test Data

		ID	L (mm)	b/t	b (mm)	t (mm)	F _y (MPa)	F _u (MPa)
Aspect Ratio	No Axial (Phase 1)	S-L1-7.5	315	7.5	95	12.7	508	545
		SL-L1-6.0	315	6.0	95	15.875	400	555
		S-L1-5.0	315	5.0	95	19.05	400	562
		S-L1-4.3	315	4.3	95	22.225	400	563
	Axial (Phase 2)	S-L1-7.5A	315	7.5	95	12.7	380	480
		SL-L1-6.0A	315	6.0	95	15.875	390	539
		S-L1-5.0A	315	5.0	95	19.05	392	552
		S-L1-4.3A	315	4.3	95	22.225	399	563
Length	No Axial (Phase 1)	L-L0.8-6.0	255	6.0	95	15.875	385	480
		SL-L1-6.0	315	6.0	95	15.875	400	555
		L-L1.2-6.0	380	6.0	95	15.875	392	551
		L-L1.4-6.0	440	6.0	95	15.875	392	542
	Axial (Phase 2)	L-L0.8-6.0A	255	6.0	95	15.875	395	549
		SL-L1-6.0A	315	6.0	95	15.875	390	539
		L-L1.2-6.0A	380	6.0	95	15.875	395	555
		L-L1.4-6.0A	440	6.0	95	15.875	392	549

3.2 Test Setup

The test setup was secured to the laboratory structural floor by four pretensioned 2.5-inch bolts, as shown in Figs. 14 to 16. The test specimens were installed to the test platform by six A490 0.75-inch bolts and the test assembly was made of 1-inch 50W plates. The cyclic displacement was applied using a hydraulic actuator with a capacity of 120 kN and a maximum stroke of 90 mm in each direction, located to the north of the pinhole. Axial compression forces were applied using a hydraulic actuator with a capacity of 120 kN, located to the east of the pinhole. The two actuators were supported vertically at both ends to avoid unintended out-of-plane loading on the specimen.

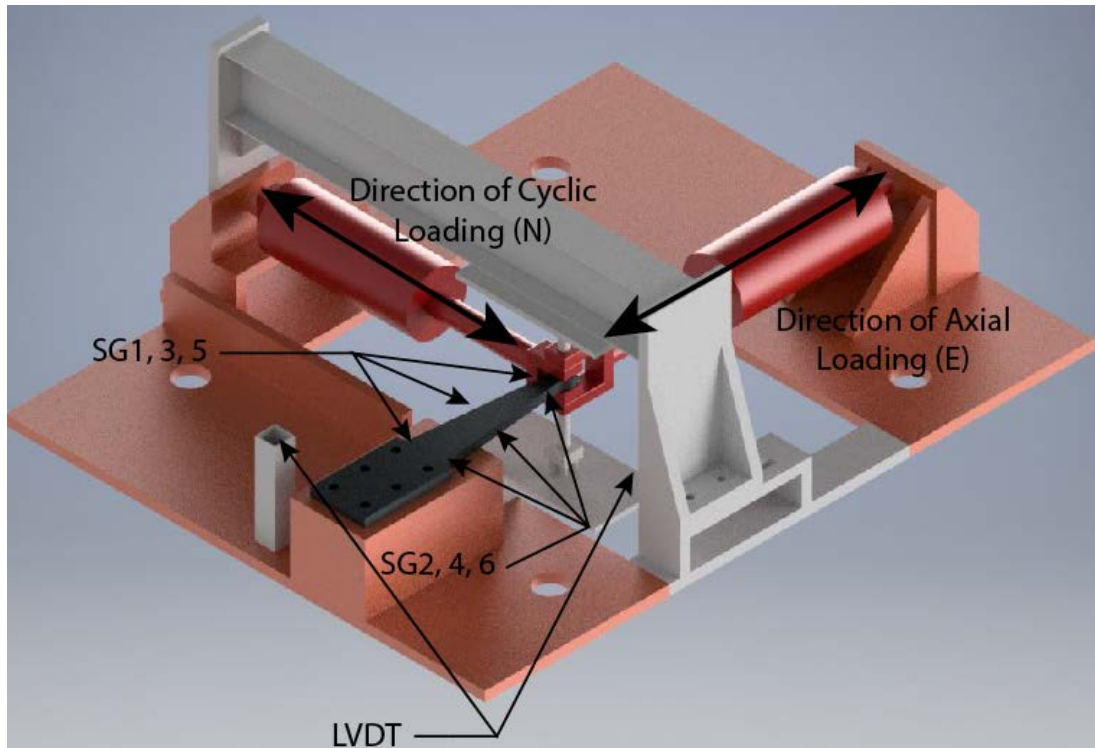


Figure 14 - Test Setup and Instrumentation

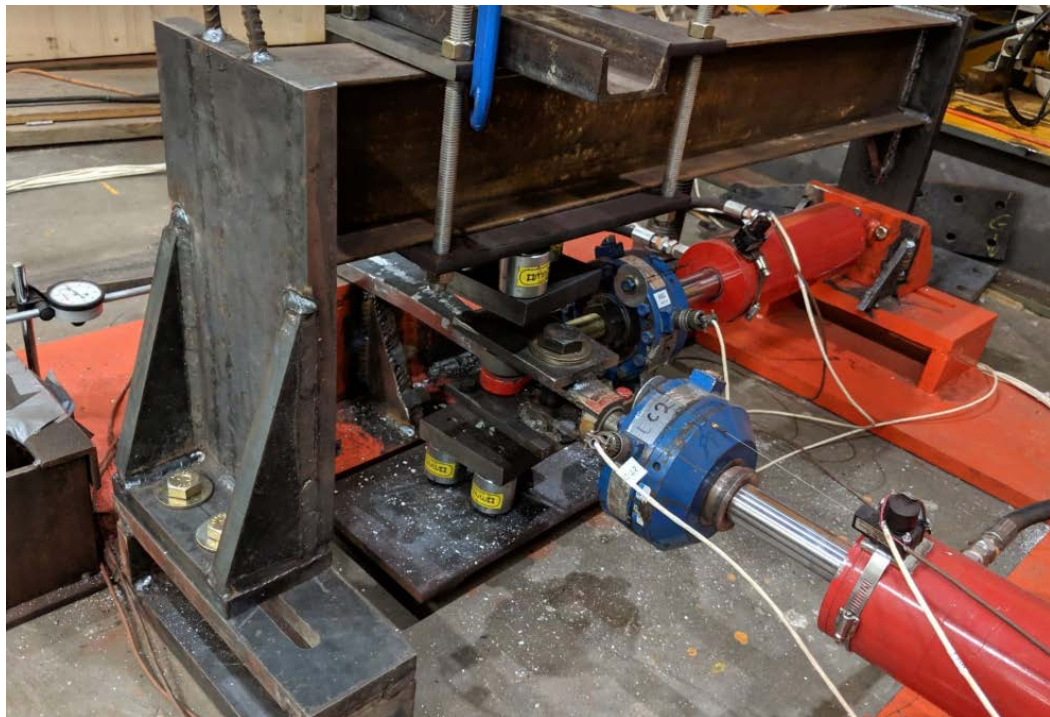


Figure 15 - Photo of Test Setup



Figure 16 - Photo of Test Setup During Testing

To replicate the in-situ boundary conditions that are expected to prevent the first global buckling mode of the flexural arms, an out-of-plane restraint system was used. The out-of-plane system comprised a stiff reaction beam and a roller assembly to permit the in-plane displacements of the actuators, while their out-of-plane displacements were restrained. The setup was inspected for damage after each test and no damage was observed at any time, except for slight ovalization of the six bolt holes on the testing platform due to local bearing stresses. Lastly, eight additional mechanical stoppers were added after the testing of S series specimens in *Phase I*, when noticeable rotations and bolt slip occurred during testing; this also prevented further ovalization of the bolt holes in the subsequent tests.

3.3 Instrumentation

Figure 14 also shows the instrumentation used throughout the test. The two actuators were connected to their own sets of LVDTs and load cells for the control system. Two additional LVDTs were attached to the roller assembly to verify the displacements of the pinhead in both in-plane directions. As can be seen in Fig. 14, six strain gauges (SG1 to SG6) were attached to the centerline of the specimen extreme fibres at each side (SG1 and SG2 at $x = 0L$; SG3 and SG4 at $x = 0.5L$; SG5 and SG6 at $x = 1.0L$) to obtain strain profile data which was used to approximate the instance of yielding. These strain gauge readings together with their respective load-displacement data were also used to help validate the finite element analysis in Chapter 4. All SG data can be found in Appendix E.

3.4 Loading Protocol – Displacement Protocol

The displacement loading protocol shown in Fig. 17 was defined based on FEMA 461 (FEMA, 2007). The target displacement was set to be 47 mm which corresponds to 3% drift of the reference wall. The displacement protocol followed FEMA 461 guidelines until the maximum stroke of the north displacement-controlled actuator (90mm) was reached. Specimens were then subjected to maximum displacement cycles until 80% strength degradation or fracture was observed.

3.5 Loading Protocol – Axial Compression Protocol

No standards or guidelines were identified in the literature for applying axial compression forces and in-plane cyclic displacements simultaneously. However, the axial demand of each flexural arm can be obtained analytically based on its hysteretic behaviour by

modeling the hysteretic performance of each specimen without axial load and finding the corresponding lateral base shear values in the same reference wall used to obtain the target displacement values. Thus, all arms without axial forces were tested first in *Phase I* and seven different flexural arm models were developed using OpenSees. These models were validated against their respective hysteretic responses in *Phase I* and accurately reflects the changes to b/t and/or L between each specimen. Afterwards, seven pushover analyses were performed up to 3% uplift to quantify the expected base shear of each wall when a different specimen model is used (Yassin, personal communication, 2018). The average base shear values were then divided by four to find the average axial compression force on each arm, under the assumption that the flexural arms were used in place of mechanical stoppers to resist sliding of the rocking wall. From the results, the expected axial compression (base shear) per arm ranged from 22 kN for the arm with the smallest force capacity, to 26 kN for the arm with the largest force capacity. Therefore, to provide an upper bound on the expected load, the axial compression force used in *Phase II* was a constant force of 30 kN, even though this load would be expected to be lower at smaller displacements.

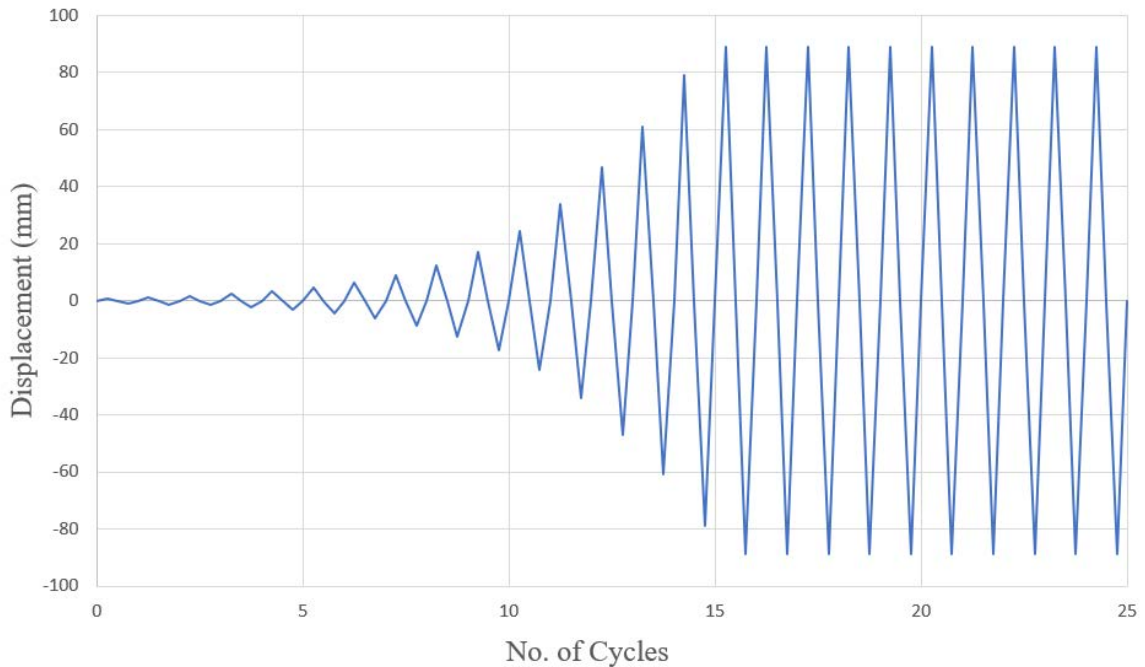


Figure 17 – Displacement Loading Protocol

3.6 Damage Sequence

In addition to the instrumentation described earlier in Section 3.3, two cameras were used to capture the failure mode and extent of damage associated with each arm. In this section, the behaviour of specimens SL-L1-6.0 and SL-L1-6.0A is described to illustrate deformation stages that were experienced during the tests. These key deformation stages are: 1) yielding, identified by the flaking of whitewash (if applicable) and/or the mounted strain gauges (i.e. SG3 and SG4 were placed at the intended location of plastic hinges from design); 2) buckling initiation, determined by visual identification; and 3) failure, defined here as 80% strength degradation or fracture. Displacements noted in the captions refer to the current displacement cycle within the loading history; for example, the notation of 5x90 mm translates to the fifth cycle at 90 mm displacement.

3.6.1 Damage Sequence in *Phase I*

Figure 18 shows the damage sequence of specimen SL-L1-6.0 from the top and side profile. This was one of the first tests conducted and whitewash was not applied to this specimen. SG3 and SG4 (Appendix E) showed that the specimen experienced more than 2000 $\mu\text{m/m}$ (the approximate yield strain based on $F_y = 400 \text{ MPa}$) at the negative 9 mm displacement cycle, indicating that yielding had occurred. The extent of yielding at the target displacement cycle of 47 mm is shown in Fig. 18c and 18d, where no buckling is visible. Signs of buckling initiation were observed at the 61 mm displacement cycle, as shown in Fig. 18f. No strength degradation was observed prior to buckling initiation of the specimens tested in *Phase I*, including specimen SL-L1-6.0 shown in Fig. 18. Furthermore, the buckling behaviour was dominated by localized buckling in the compression zone around $x = 0.5L$ leading to progressively larger out-of-plane deflections, shown in Figs. 18i, 18j, 18k, and 18l. Since buckling could not occur in tension, this deflection accumulated in the compression side only, which alternated based on the cyclic displacement protocol. For example, this caused potential decreases to out-of-plane deflections due to the tension stresses stretching out the buckled region, which results in an increase to the displacement capacity of the device. Ultimately, the specimen failed at a displacement of 5x90 mm, as shown in Figs. 18i, 18j, 18k, and 18l.

In general, most specimens tested in *Phase I* experienced yielding at approximately $x = 0.5L$, which is almost where yielding/plastic hinging was designed to occur, as shown in Fig. 19 for specimen L-L1.2-6.0 for a clearer illustration. In addition, Fig. 19 also shows that although ideal simultaneous yielding of the extreme outer fibres was not achieved with

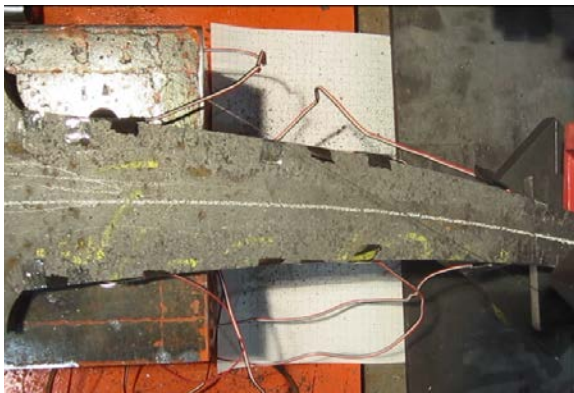
the straight outer edges, it was enough to achieve significant engagement of the whole arm at higher displacement demands.



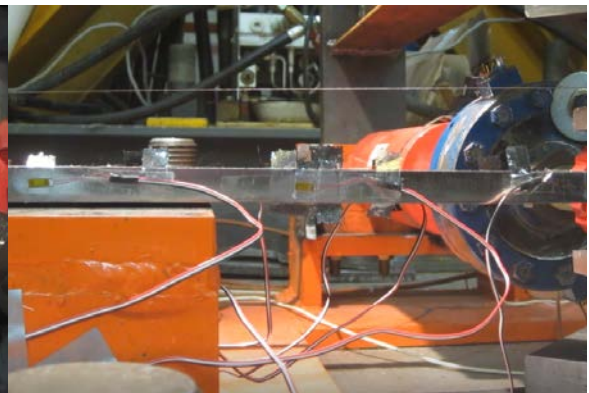
(a) Yielding – Top View (9 mm)



(b) Yielding – Side View (9 mm)



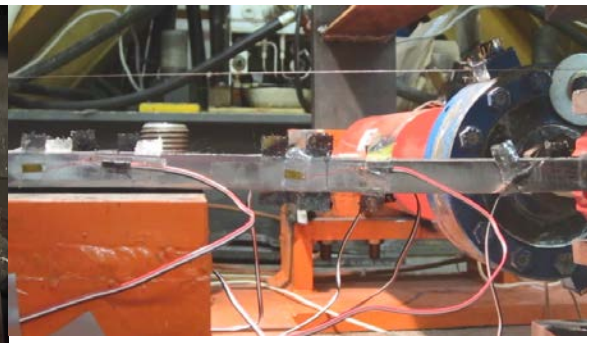
(c) Target Displacement – Top View (47 mm)



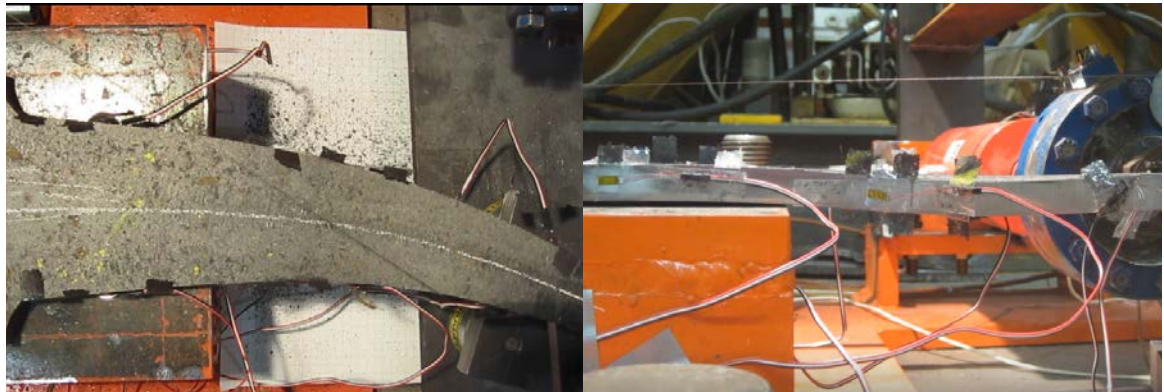
(d) Target Displacement – Side View (47 mm)



(e) Buckling Initiation – Top View (61 mm)



(f) Buckling Initiation – Side View (61 mm)



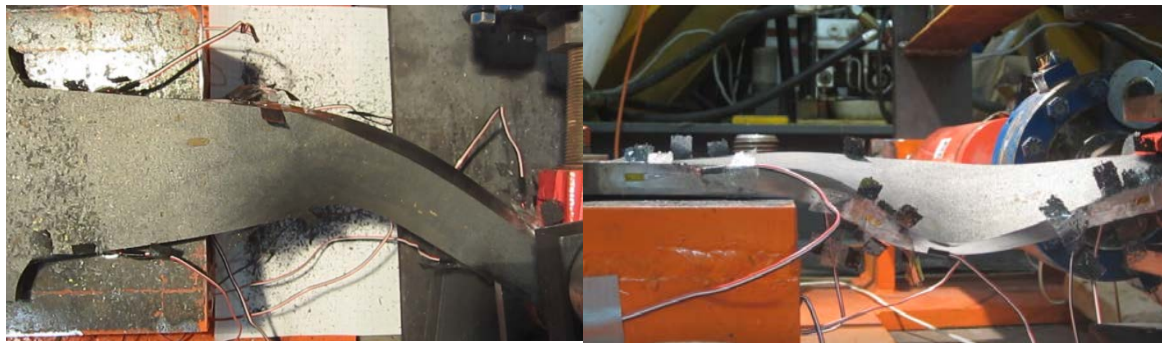
(g) Max Displacement – Top View (90 mm)

(h) Max Displacement – Side View (90 mm)



(i) Prior to Failure – Top View (4x90 mm)

(j) Prior to Failure – Side View (4x90 mm)



(k) Failure – Top View (5x90 mm)

(l) Failure – Side View (5x90 mm)

Figure 18 - Photos of specimen SL-L1-6.0

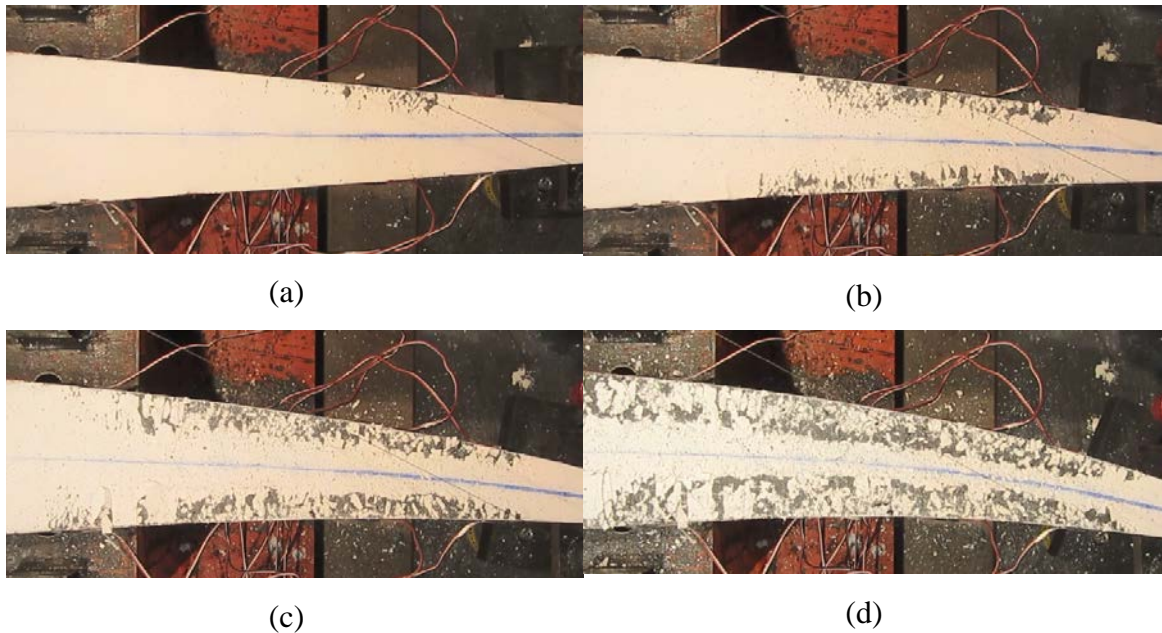
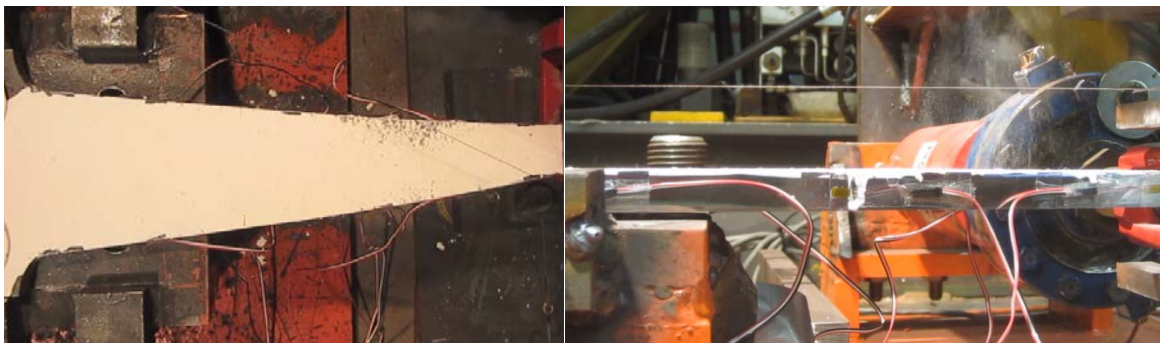


Figure 19 - Progression on Yielding on Specimen L-L1.2-6.0

3.6.2 Damage Sequence in *Phase II*

To allow for direct comparison between *Phase I* and *Phase II*, Figure 20 shows the damage sequence of specimen SL-L1-6.0A which had the same geometrical configuration of specimen SL-L1-6.0 shown earlier in Figure 18, but with the addition of axial compression. From the experimental results of both specimens, the axial compression accelerated the onset of yielding from 9 mm in specimen SL-L1-6.0 to 6 mm in specimen SL-L1-6.0A (Figs. 18a, 18b, 20a, 20b), and subsequently more yielding was observed at the target displacement cycle in *Phase II* (Figs. 18c, 18d, 20c, 20d). Similar to that in *Phase I*, the buckling behaviour in *Phase II* is assumed to begin with the localized buckling of the compression zone, around $x = 0.5L$; however, experiments showed that the actual location of yield and buckling initiation for *Phase II* specimens are closer to $x = 0.67L$, as seen in Fig. 20a and discussed more thoroughly in Appendix I. Furthermore, although the two

specimens experienced buckling initiation at the same displacement cycle (61 mm), the 30 kN of axial compression played a major role in propagating the rapid transition of buckling behaviour from initiation to failure in only one displacement cycle from 61 mm to 75 mm, as shown in Figs. 20e, 20f, 20g, 20h. In addition, as shown in Figs. 20k and 20l, specimen SL-L1-6.0A failed due to 80% strength degradation after a single displacement cycle at 90 mm while specimen SL-L1-6.0 was able to sustain five displacement cycles at 90 mm, as shown in Figs. 18k and 18l. This behaviour is also demonstrated in Fig. 21, which shows specimen S-L1-7.5A depicting the same buckling progression leading to failure as specimen SL-L1-6.0A. More specifically, the fuses in *Phase II* do not experience the same alternating displacement accumulation phenomenon caused by the buckling pattern described in *Phase I*. This failure pattern was the dominant behaviour in *Phase II*, where the axial load would increasingly govern the buckling behaviour as the out-of-plane deflections increased, where most specimen failures in *Phase I* were caused by the lateral torsional buckling of the fuses. Overall, the fuse behaviour under axial load can generally be characterized by more rapid progression through the stages of buckling initiation, strength degradation, and then failure.

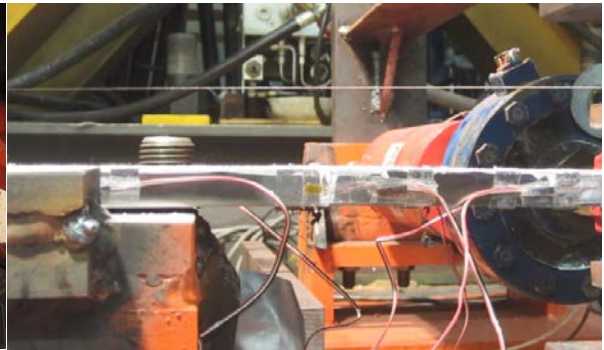


(a) Yielding – Top View (6 mm)

(b) Yielding – Side View (6 mm)



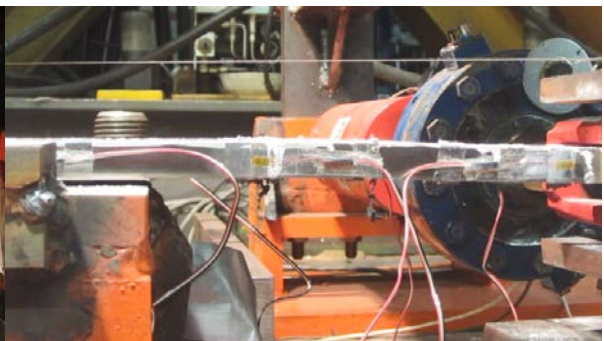
(c) Target Displacement – Top View (47 mm)



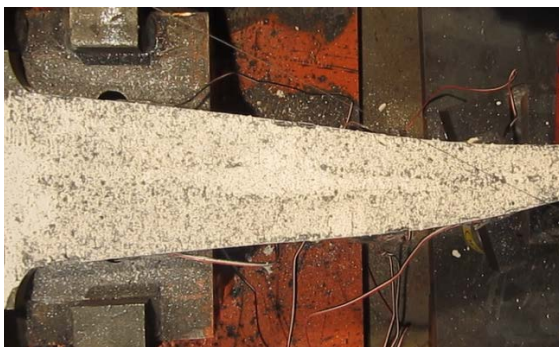
(d) Target Displacement - Side View (47 mm)



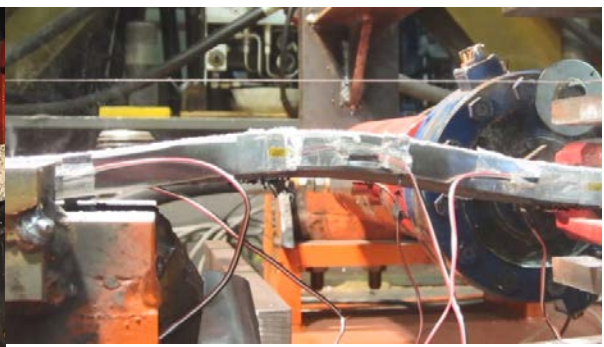
(e) Buckling Initiation – Top View (61 mm)



(f) Buckling Initiation – Side View (61 mm)



(g) Prior to Failure – Top View (75 mm)



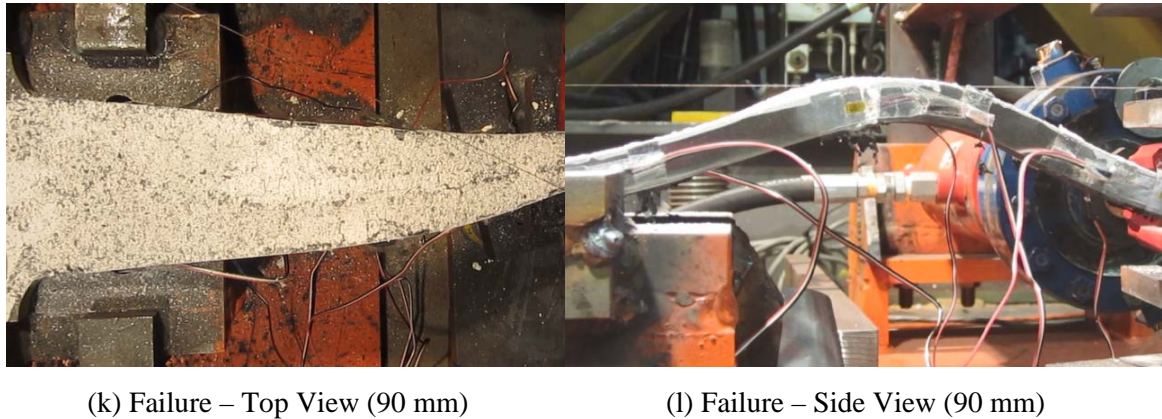
(h) Prior to Failure – Side View (75 mm)



(i) Max Displacement - Top View (90 mm)



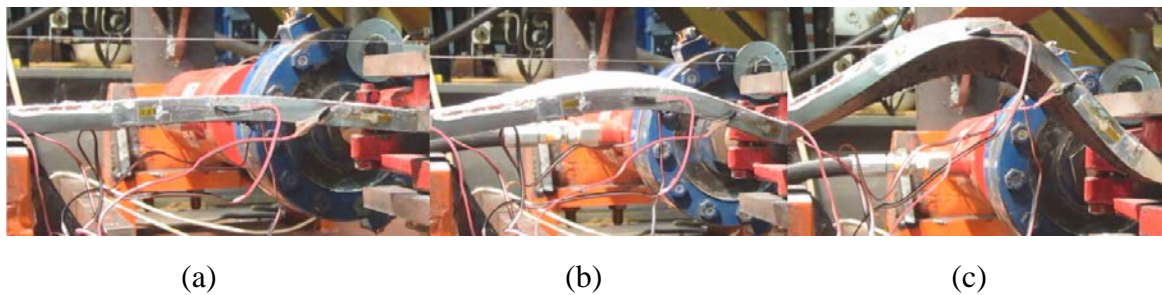
(j) Max Displacement - Side View (90 mm)



(k) Failure – Top View (90 mm)

(l) Failure – Side View (90 mm)

Figure 20 - Photos of specimen SL-L1-6.0A



(a)

(b)

(c)

Figure 21 - Test Photos of Specimen S-L1-7.5A: (a) Local Buckling (34 mm); (b) Global Buckling (47 mm); (c) Failure (47 mm)

3.6.3 Test Observations for All Specimens

The damage sequences for all other specimens can be found in Appendix D. These outline the deformation profile of each specimen at 47 mm, 90 mm, and failure, except for those that did not have a camera setup or that failed at earlier displacement cycles. Specimens S-L1-7.5 and S-L1-6.0 were two of the first conducted tests and whitewash was not applied to these specimens. The whitewash in some tests clumped while drying and caused some variations in flaking behaviour, but general yielding trends can still be observed. Most specimens in *Phase II* had a higher extent of buckling compared to those in *Phase I*, thus lower displacement ductility capacities. Most tests ended when 80% strength degradation

was reached, though three specimens (S-L1-4.3, S-L1-4.3A, S-L1-5) failed in fracture due to low cycle fatigue. Of these three, only the thickest specimens (S-L1-4.3 and S-L1-4.3A) did not experience any buckling initiation. No cracks or visible damages aside from yielding occurred in the non-fractured specimens.

3.7 Qualitative Discussion of Observations – Experimental Data

Table 2 summarizes the experimental results of the thirteen arms because specimen L-L0.8-6.0A was destroyed due to a laboratory error and no data was obtained. Experimental yield forces (Q_y) were determined by identifying the force when SG3 or SG4 first exceeded 2000 $\mu\text{m/m}$, while experimental plastic forces (Q_p) were identified as the peak value from their respective load-displacement data shown in Figs. 22 and 23. These figures represent the displacement and forces measured by the LVDT and the load cell in the north actuator, respectively. Theoretical yield and plastic forces (Q_{yt} , Q_{pt}) for specimens tested in *Phase I* and *Phase II* were predicted by using the nominal strength design equations (presented earlier in Eqs. (2), (3), (4), and (5)) and compared against the experimental result to assess for their accuracy. For *Phase II* specimens, the value of Δ_y used to calculate $Q_{yt,axial}$, $Q_{pt,axial}$ were the measured displacements for each corresponding specimen obtained from *Phase I* when SG3 or SG4 first measured 2000 $\mu\text{m/m}$. The second term in Eqs. (4) and (5) which accounts for the contribution due to axial compression forces were always less than 3.4% and 2.4% of the values of $Q_{yt,axial}$ and $Q_{pt,axial}$, respectively. Cumulative displacements at buckling initiation, onset of strength degradation, and failure, were chosen

as the engineering displacement parameters since most specimens could not be tested to their full displacement capacities due to limitations of the actuator stroke.

Table 2 - Test Matrix with Results

ID	Q _y (kN)	Q _y /Q _{yt}	Q _p (kN)	Q _p /Q _{pt}	Cumulative Disp @ Buckling Initiation (mm)	Cumulative Disp @ Str Degradation (mm)	Cumulative Disp @ Failure (mm)
S-L1-7.5	18.7	0.68	39.0	0.95	79.8	1215.4	1927.4
SL-L1-6	24.3	0.90	55.0	1.36	899.4	1927.4	2995.4
S-L1-5	28.2	0.87	68.0	1.40	2639.4	2995.4	7979.4
S-L1-4.3	33.7	0.89	78.0	1.38	FRACTURE	3351.4	6911.4
S-L1-7.5A	15.0	0.79	24.8	0.87	467.4	467.4	655.4
SL-L1-6A	23.2	0.94	45.3	1.22	655.4	1393.4	1482.4
S-L1-5A	27.2	0.90	57.9	1.28	1215.4	2639.4	2995.4
S-L1-4.3A	32.9	0.91	66.9	1.23	FRACTURE	FRACTURE	5487.4
L-L0.8-6	28.6	0.89	69.0	1.44	655.4	1571.4	2283.4
SL-L1-6	24.0	0.89	55.0	1.36	899.4	1927.4	2995.4
L-L1.2-6	19.0	0.87	43.0	1.31	1571.4	1927.4	2995.4
L-L1.4-6	17.4	0.92	35.0	1.23	1571.4	2283.4	4775.4
L-L0.8-6A	-	-	-	-	-	-	-
SL-L1-6A	23.2	0.94	45.3	1.22	655.4	1393.4	1482.4
L-L1.2-6A	20.1	0.95	37.9	1.20	1215.4	1571.4	1927.4
L-L1.4-6A	16.5	0.92	30.9	1.14	1215.4	1571.4	1571.4

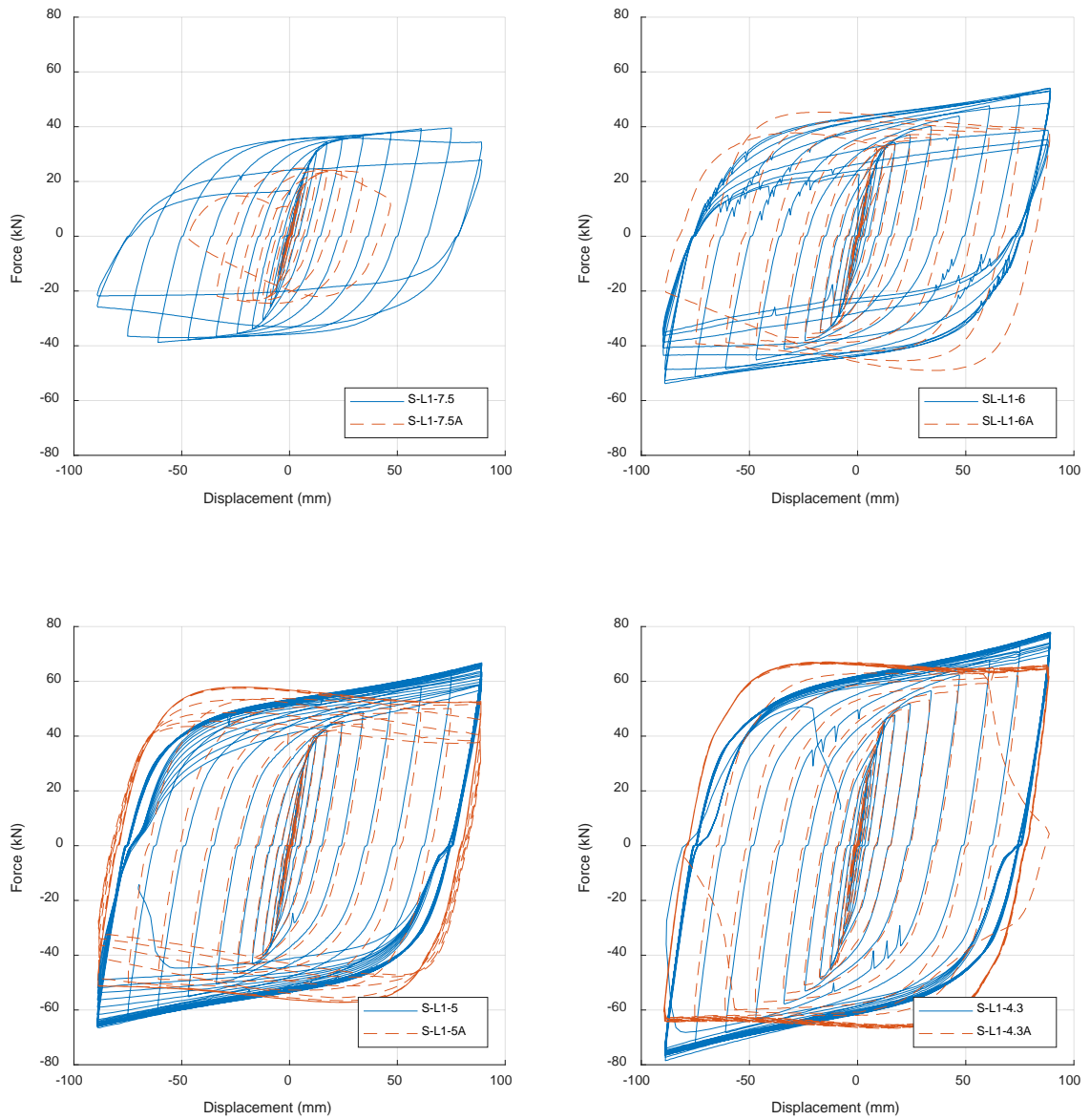


Figure 22 - Experimental Load Displacement Loops for Aspect Ratio

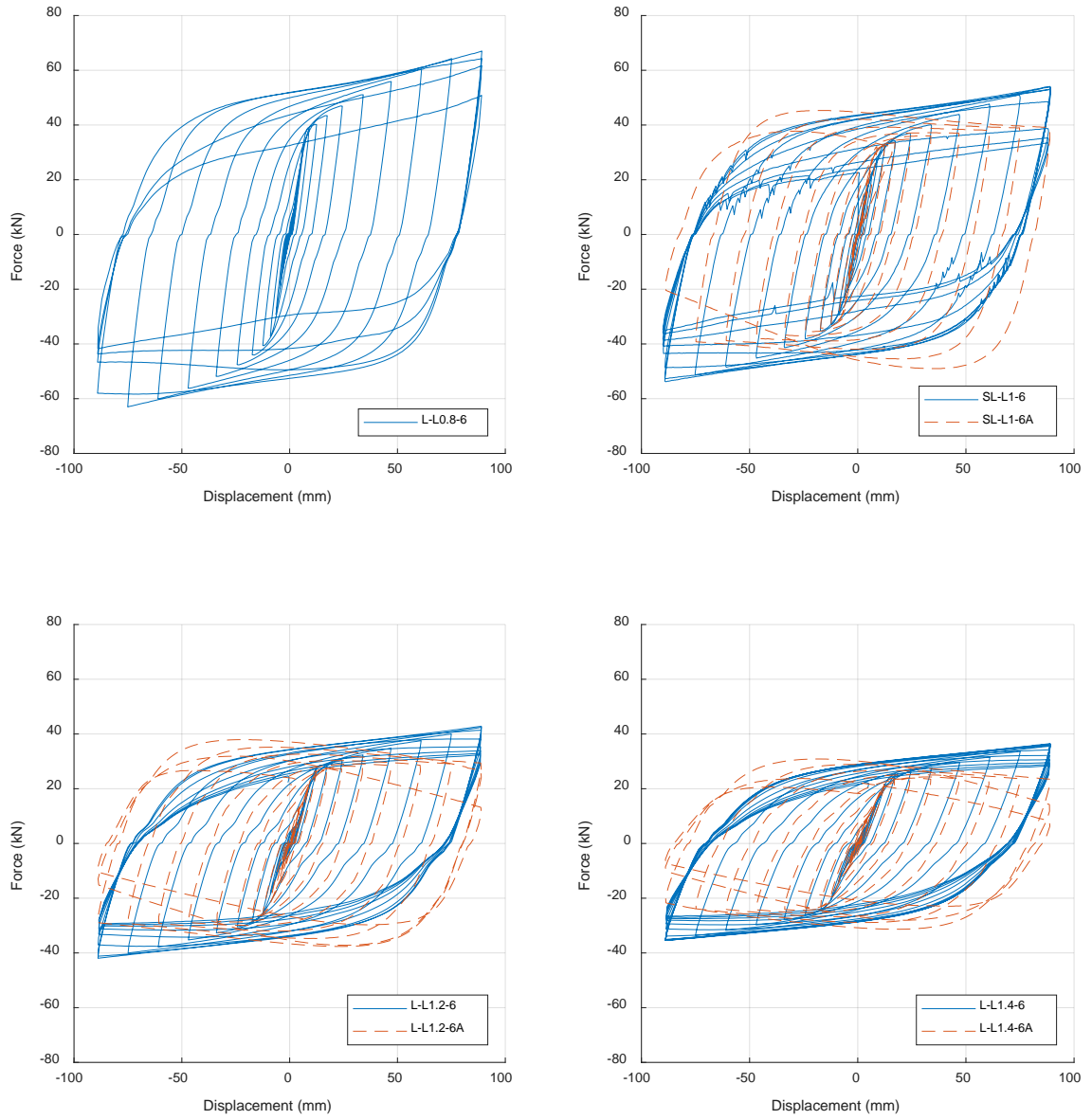


Figure 23 - Experimental Load Displacement Loops for Length

3.7.1 Qualitative Discussion of Observations – Forces in *Phase I*

Almost all specimens tested in *Phase I* performed similarly up to the maximum actuator displacement (90 mm) as discussed earlier in Section 3.6.1 and confirmed by the hysteretic responses shown in Figs. 22 and 23. More specifically, all specimens except one in *Phase I* were able to reach 90 mm displacement without signs of strength degradation and any observable strength degradation was caused by the progression of buckling in the arm, ultimately causing failure due to reaching 80% strength degradation. As can be seen in Figs. 22 and 23, all specimens tested in *Phase I* also showed positive post-yield stiffnesses and thus experienced their peak forces at peak displacements. However, because of the limits on the actuator stroke, the true peak force capacities were not reached for any specimens except for S-L1-7.5, which is demonstrated by the lack of post-peak behaviour. This suggests that higher peak forces could have been observed if these specimens were subjected to higher displacement levels.

A combination of bolt slip and progression of bearing ovalization caused noticeable rotations during testing between the bolt group of the flexural arm and the testing platform. This contributed to some jagged responses due to large bolt slips, as seen in the hysteretic response of specimen SL-L1-6.0 and S-L1-4.3 in Fig. 22. Furthermore, these could also have resulted in some loss of stiffness in the hysteretic loops, as the flexural arms were observed to be slightly rotating when the actuator transitioned from one push (or pull) displacement cycle to the opposite direction. However, the effect of this stiffness loss is hard to quantify and did not influence the observed peak force capacities because the bolts would eventually lock against the bolt holes. These issues were mitigated when eight

mechanical stoppers were welded onto the testing platform for the L series specimens tested in *Phase I* and subsequently for all specimens tested in *Phase II*, as mentioned in Section 3.2.

3.7.2 Qualitative Discussion of Observations – Forces in *Phase II*

Similar to *Phase I*, most specimens tested in *Phase II* also performed similarly to one another up to maximum actuator displacement. However, the presence of axial compression negatively influenced the peak force capacities of the specimens in *Phase II* when compared to their counterparts in *Phase I*. In addition, although specimens in *Phase II* increased the load that they carried during each cycle of increasing displacement, the peak forces of these specimens often occurred before reaching the peak displacements. Furthermore, this peak force was typically also higher than the forces measured on the *Phase I* specimens at the same displacement levels. For example, as shown in Fig. 22, the force at 90 mm displacement for specimen SL-L1-6.0 was 54 kN (plastic force, Q_p , for this specimen), while the force for specimen SL-L1-6.0A was 39 kN. On the other hand, the force at -40 mm displacement for specimen SL-L1-6.0 was 37 kN, while the force for specimen SL-L1-6.0A was 45 kN (peak force, Q_p , for this specimen). Lastly, post-peak behaviour due to ultimate shear displacement demand was rarely observed because larger displacement cycles were always accompanied by a larger peak force. For example, only specimens S-L1-7.5A and SL-L1-6.0A kept gaining strength until the last cycle at their peak displacement (47 mm and 90 mm, respectively) before exhibiting strength degradation prior to failure, while other specimens (i.e. L-L1.2-6.0A and L-L1.4-6.0A) cycled at

maximum displacement before strength degradation indicating that higher forces could be expected following larger displacements.

Therefore, Q_p values for specimens in *Phase II* were taken as the peak forces and did not occur at the maximum actuator displacement. Two potential sources contributing to this behaviour can be related to the introduction of axial forces and elastic deformations/slack in the system. First, the inclusion of axial forces contributed to the overall instability of the flexural device due to P-delta effects. Second, the applied constant axial force kept the whole system engaged throughout the whole testing procedure, thus reducing the elastic deformations and slack experienced by the flexural arm as the device cycles through the displacement protocol. This reduction of deformations would create a stiffer and more reactive test setup, resulting in higher forces at lower displacements. Aside from these behaviours, strength degradation of the *Phase II* specimens was mostly due to buckling and always occurred after buckling initiation.

3.7.3 Qualitative Discussion of Observations – Displacements in *Phase I*

Figures 22 and 23 show that there were some visible displacement tolerances in the system which corresponds to the displacements measured by the LVDT on the north actuator. This tolerance can be seen in all the hysteresis loops of the specimens tested in *Phase I*, near zero vertical force, when the whole system is temporarily disengaged in one pull/push direction as it transitions into the opposite direction. This is due to the overall construction tolerances of the test setup, separate from elastic deformations, which translated to roughly 1 mm in displacement stroke.

All specimens in *Phase I*, except specimen S-L1-7.5, reached the target design displacement of 47 mm before any signs of buckling initiation was observed. Furthermore, most specimens were able to achieve the 90 mm displacement cycle with minimal buckling, which corresponds to 5.7% of wall drift. In general, the results showed that thicker specimens were generally able to sustain more and larger displacement cycles before buckling and fracture than thinner specimens. However, one test shows that the total suppression of buckling initiation may lower cumulative displacement performance before failure. This is shown by specimen S-L1-5 versus S-L1-4.3, where the thinner specimen S-L1-5 experienced buckling and was able to sustain three more maximum displacement cycles before failure than specimen S-L1-4.3 which did not buckle and fractured earlier due to low cycle fatigue. Lastly, since post-peak behaviour was not observed due to limitations of the actuator stroke, almost all specimens are expected to be able to sustain larger displacements than those shown here.

3.7.4 Qualitative Discussion of Observations – Displacements in *Phase II*

In *Phase II*, it was observed that all specimens except one (S-L1-7.5A) reached the target design displacement of 47 mm without buckling initiation. In addition, the majority of specimens sustained the first 90 mm cycle of maximum actuator displacement with minimal to no buckling. However, all measured cumulative displacement parameters in *Phase II* were lower than those in *Phase I*, indicating that axial forces had a negative influence on the device performance as expected. Finally, due to the presence of axial loads, the visible displacement tolerances in the system are less pronounced in *Phase II* compared to those in *Phase I*, as described in Section 3.7.3.

3.8 Quantitative Discussion of Test Results – Forces and Displacements

3.8.1 Quantitative Discussion of Test Results - Forces in *Phase I*

Table 2 shows that the predicted yield forces, using the design Eq. (2), are within +8% to +13% of the experimental value, except for specimen S-L1-7.5 which may be affected by material properties due to the lack of a visible yielding plateau, as shown in Appendix A. This would have affected its experimental yield stress, skewing the value used in the design equations, thus contributing to inaccuracies. Other potential sources of error may include variations from the interpretation of stress-strain data, cyclic versus uniaxial loading effects, and approximating the location of yielding. For example, SG3 and SG4 may not have been placed at the true location of yielding initiation, as discussed earlier in Section 3.6.1.

Conversely, except specimen S-L1-7.5, the experimental plastic/peak forces were higher than their predicted counterparts, with minimum and maximum deviations of -23% and -44%, respectively. As mentioned earlier, peak plastic forces were not reached for most specimens in *Phase I*, due to the limitations of maximum actuator stroke, which suggests that even higher forces should be expected at larger displacement levels. Ma et al. (2010) also reported that for butterfly fuses, the experimental peak forces were approximately 2 to 2.3 times the predicted theoretical values, which could be consistent with the findings of the current study if the current specimens had not been limited by actuator stroke. Based on these observed differences and the limited database of tested devices, the theoretical design equations for plastic (peak) forces need to be further investigated to prevent the risk of violating capacity design philosophies.

3.8.2 Quantitative Discussion of Test Results – Forces in *Phase II*

The predicted yield values using Eq. (4) for specimens tested in *Phase II* were within +5% to +10% of the experimental findings, while the predicted peak values using Eq. (5) were within -14% to -28% of the experimental findings. Both these ranges do not include specimen S-L1-7.5A, which buckled unexpectedly, and no yielding plateau was observed for specimen S-L1-7.5A which may have also decreased the overall accuracy of the design equations. Other sources of inaccuracies are expected to be the same as discussed in Section 3.8.1. The summary of predicted values using the design equations can be found in Table 2, while Table 3 summarizes the performance of the measured engineering force parameters in *Phase II*, as a percentage of *Phase I* values, both normalized by their respective yield stresses shown in Table 1. For example, for specimen SL-L1-6.0A, $N_{Qy,axial} =$

$$Q_{y,axial}/390 \text{ MPa} \quad \text{and} \quad N_{Qy,non-axial} = Q_{y,non-axial}/400 \text{ MPa} \quad , \quad \text{therefore}$$

$$N_{Qy,axial}/N_{Qy,non-axial} = 98\%.$$

3.8.3 Quantitative Discussion of Test Results – Displacements in *Phase I*

The displacement performance of each specimen at failure, visible strength degradation, and buckling initiation are summarized in Table 2. The specimens in *Phase I* generally experienced higher delays between each displacement stage when compared to *Phase II*, in addition to experiencing each stage at a further cumulative displacement level.

3.8.4 Quantitative Discussion of Test Results – Displacements in *Phase II*

As presented in Table 3, the axial forces in *Phase II* had a greater influence on the displacement capacities than the force capacities. More specifically, specimens in the S

series of *Phase II* had (relative to *Phase I*) 46% to 73% of cumulative displacement before buckling initiation, 38% to 88% of cumulative displacement before strength degradation, and 34% to 79% of cumulative displacement before failure. Additionally, specimens in the L series of *Phase II* had (relative to *Phase I*) 73% to 77% of cumulative displacement before buckling initiation, 69% to 82% of cumulative displacement before strength degradation, and 33% to 64% of cumulative displacement before failure.

Table 3 - Comparison of Engineering Parameters in Phase II, Expressed in Percentages of Phase I Performance

ID	Cumulative Disp @ Buckling Initiation	Cumulative Disp @ Str Degradation	Cumulative Disp @ Failure	Q _y	Q _p	Cumulative Energy Dissipated
S-L1-7.5A	-	38%	34%	107%	85%	20%
SL-L1-6A	73%	72%	49%	98%	84%	40%
S-L1-5A	46%	88%	38%	98%	87%	52%
S-L1-4.3A	-	-	79%	98%	86%	94%
L-L0.8-6A	-	-	-	-	-	-
SL-L1-6A	73%	72%	49%	99%	84%	40%
L-L1.2-6A	77%	82%	64%	105%	88%	58%
L-L1.4-6A	77%	69%	33%	95%	88%	38%

3.9 Discussion of Test Results - Design Parameters

3.9.1 Effect of L

Since no full design guidelines for the displacement capacity of flexural arms were found before this study, the preliminary design of the current device started with the assumption that arms with a ratio $b/t = 6$ should not experience buckling initiation before 14% shear deformation (Δ/L) (Ma et al., 2010). This assumption together with other design considerations mentioned in Section 2.5 were subsequently used to obtain the control arm length of $L_{ref} = 315$ mm. The results shown in Table 4 demonstrate this assumption was conservative in predicting the displacement before buckling initiation for flexural devices with an aspect ratio of 6. More specifically, for the L series flexural arms tested in *Phase I*

($b/t = 6$) with yielding length from $L = 0.8L_{ref}$ to $1.4L_{ref}$, the arms buckled after 18% to 24% shear deformation which is somewhat larger than what was reported from previous experiments.

In *Phase II*, the displacement capacity before buckling initiation for flexural arms under axial loads with $b/t = 6$ and varying L ranged from 15% to 20% shear deformation. Each specimen of the L series in *Phase II* suffered a decrease in shear deformation capacity before buckling initiation by -3.4%, -4.0%, and -4.5% for specimens L-L1.4-6.0A, L-L1.2-6.0A, and SL-L1-6.0A, respectively. Although specimen L-L0.8-6.0A broke during testing, the general trend of the L series specimens tested in *Phase II* suggests that a decrease of 4% in the displacement performance before buckling initiation can be expected, which results in a prediction of 14% shear deformation or less before buckling initiation. Therefore, the expected displacement performance before buckling initiation for flexural arms with $b/t = 6$ and different lengths under 30 MPa of axial compression stress (at the location of intended yielding/buckling $x = 0.5L$, as discussed previously in Section 3.1) ranges from 14% to 20% shear deformation.

Additionally, the design equations (Eqs. (2) and (4)) for *Phase I* and *Phase II* were quite accurate in predicting the yield force of flexural arms with $b/t = 6$ and different lengths for both without and with axial loads, ranging from +8% to +13% and +5% to +8%, respectively. Furthermore, a positive correlation can be seen between L and the accuracy of Eqs. (3) and (5) for estimating the peak strength where the measured peak strength reduces from 144% of theoretical for L-L0.8-6.0 to 123% for L-L1.4-6.0 in *Phase I*, and 122% of theoretical for SL-L1-6.0A to 114% for L-L1.4-6.0A in *Phase II*.

Table 4 - Summary of Performances for all Specimens

		ID	Actuator Displacement @ Buckling Initiation (mm)	Shear Deformation @ Buckling Initiation (%)	Difference in Shear Deformation in Phase II	Qy/Qyt	Qp/Qpt	Axial Stress @ $x = 0.5L$ (MPa)	
Length	No Axial (Phase 1)	L-L0.8-6.0	47	18%	-	0.89	1.44	-	
		SL-L1-6.0	61	19%	-	0.89	1.36	-	
		L-L1.2-6.0	90	24%	-	0.87	1.31	-	
		L-L1.4-6.0	90	20%	-	0.92	1.23	-	
Axial (Phase 2)		L-L0.8-6.0A	-	-	-	-	-	30	
		SL-L1-6.0A	47	15%	-4.5%	0.94	1.22	30	
		L-L1.2-6.0A	75	20%	-4.0%	0.95	1.20	30	
		L-L1.4-6.0A	75	17%	-3.4%	0.92	1.14	30	
Aspect Ratio	No Axial (Phase 1)	S-L1-7.5	9	3%	-	0.68	0.95	-	
		SL-L1-6.0	61	19%	-	0.90	1.36	-	
		S-L1-5.0	90 +	> 28%	-	0.87	1.40	-	
		S-L1-4.3	90 +	> 28%	-	0.89	1.38	-	
	Axial (Phase 2)		S-L1-7.5A	24	8%	+5%	0.79	0.87	37
			SL-L1-6.0A	47	15%	-4.5%	0.94	1.22	30
			S-L1-5.0A	75	24%	-4% or more	0.90	1.28	25
			S-L1-4.3A	90 +	> 28%	-	0.91	1.23	21

3.9.2 Effect of b/t

Although decreasing the aspect ratios b/t of flexural arms (by keeping b constant and increasing t) significantly delayed the initiation of buckling, clear relationships between the displacement performances in *Phase I* could not be easily established since two out of the four arms did not experience buckling initiation at maximum actuator displacement. Therefore, Table 4 shows that buckling was initiated in specimens S-L1-5.0 and S-L1-4.3 at > 28% shear deformation, since the two specimens were able to sustain three and sixteen cycles at 90 mm displacement without any signs of buckling initiation.

Similarly, Table 4 shows that the displacement performance before buckling initiation of S series specimens in *Phase II* were also negatively influenced by about -4% shear deformation under 30 MPa to 25 MPa of axial stress, although exact trends could not be established. This is due to a couple of factors. First, the displacement performance before buckling initiation of S-L1-7.5A increased with axial loading, which acts counter

intuitively to the theoretical understanding that an increase of axial compression will contribute to reaching critical buckling stress faster, simply by increasing the compression stresses in the compression flange. Secondly, direct comparisons in the performance of S-L1-5A and S-L1-4.3A to their *Phase I* counterparts can not be made since their displacement performances before buckling initiation were not established. Nevertheless, a decrease to b/t (by keeping b constant and increasing t) still proved to be very effective at delaying buckling initiation until higher shear deformation cycles.

In general, the theoretical equations for yield and plastic strength were both quite accurate for the S series flexural arms with varying b/t , except for specimens S-L1-7.5 and S-L1-7.5A. Firstly, Eqs. (2) and (3) were able to predict the experimental yield and peak strength in *Phase I* by within +10% to +13% and within -36% to -40%, respectively. Second, Eqs. (4) and (5) were able to predict the experimental yield and peak strength in *Phase II* by within +6% to +10% and -22% to -28%, respectively. Furthermore, the predicted yield strength equations in both phases were also more accurate than the predicted peak strength equations. The low variance of the prediction values of all yield and peak strengths regarding varying b/t suggests that the equations may be precise, but inaccurate.

Lastly, the change in axial stress levels did not have a high influence on the strength performance of flexural arms. This is possibly due to the low axial stresses (21 MPa to 37 MPa) used in the current study, where a higher axial stress may cause a more noticeable effect. Furthermore, as discussed previously, the true peak strengths were not established for many specimens in *Phase I* or *Phase II*, which may result in higher and more varying values indicating different relationships all together. Thus, it would be ideal to conduct

more tests with and without axial loads so that the accuracy of the prediction equations can be improved. However, at current axial demand levels, these flexural arms all performed well beyond target displacement levels and the current theoretical equations are sufficient in estimating the overall strength performance of these devices.

3.10 Quantitative Discussion of Test Results – Energy Dissipation Capacities

Figure 24 shows the relationship between the cumulative energy dissipated per volume of yielding steel to b/t and L , with and without axial forces, while Fig. 25 plots the relationship between cumulative displacement to b/t and L , with and without axial forces. The values for cumulative energy dissipated were normalized by the total volume of the yielding steel for each specimen to obtain the effective energy dissipation performance per unit volume to allow for a better comparison between specimens with different geometric properties. The ratios between specimens tested in *Phase II* and their counterparts in *Phase I*, regarding cumulative energy dissipated and cumulative displacement before failure were summarized previously in Table 3.

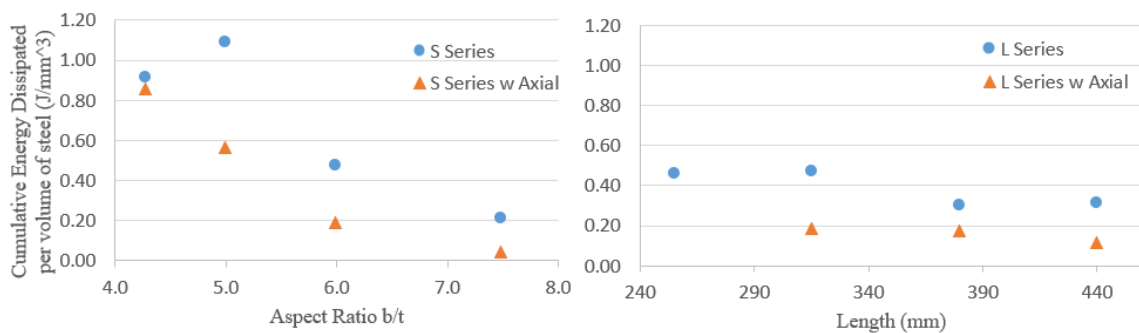


Figure 24 - Cumulative Energy Dissipated per Volume of Yielding Steel to Aspect Ratio and L

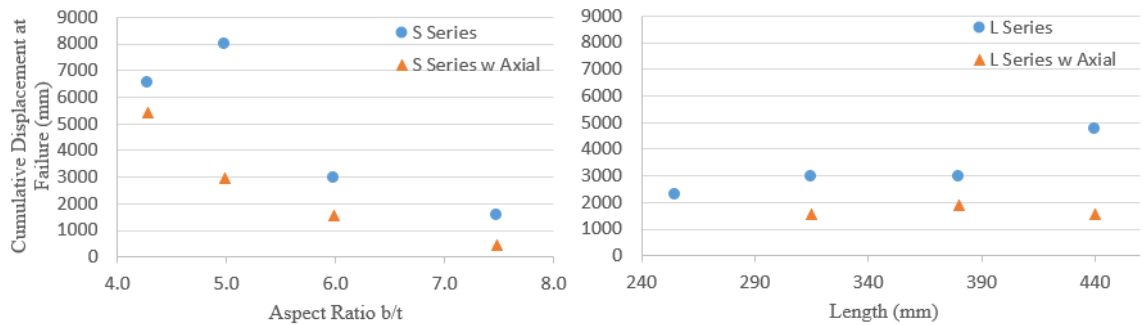


Figure 25 - Cumulative Displacement at Failure to Aspect Ratio and L

As seen in Figs. 24 and 25, the axial compression forces negatively influenced the performance of flexural arms in both the normalized cumulative energy dissipation and cumulative displacement capacity before failure; however, in both *Phase I* and *Phase II*, specimens with lower aspect ratios (b/t) have higher cumulative energy dissipation capacities than those with higher aspect ratios. For example, specimen S-L1-4.3 ($b/t = 4.3$) had 0.92 J/mm^3 normalized energy dissipation capacity where specimen S-L1-7.5 ($b/t = 7.5$) had 0.21 J/mm^3 ; comparatively, specimen S-L1-4.3A ($b/t = 4.3$) had 0.86 J/mm^3 and specimen S-L1-7.5A ($b/t = 7.5$) had 0.04 J/mm^3 . The high energy dissipation capacities of these specimens with lower aspect ratios is primarily due to the delayed onset of buckling initiation and subsequently failure, which allowed for more stable hysteretic behaviour at larger and additional displacement cycles. However, specimen S-L1-5 ($b/t = 5$) performed better than the thicker specimen S-L1-4.3 ($b/t = 4.3$), which may be because it was able to buckle during the tests and thus delay the fracture of the fuse caused by low cycle fatigue, but further testing would be required to verify this. Furthermore, thicker specimens with lower aspect ratios were more resistant to the negative influences of axial compression on

the normalized cumulative energy dissipation capacity, ranging from 94% of the *Phase I* performance in specimen S-L1-4.3A to 20% in specimen S-L1-7.5A.

On the other hand, although *Phase I* specimens with higher L values were able to sustain higher cumulative displacements (Fig. 25) than other *Phase I* specimens with lower L values as discussed earlier, these specimens with higher L values also showed lower normalized energy dissipation capacities (Fig. 24). For example, as can be seen in Fig. 24 and 25 for *Phase I*, the specimen with $L = 440$ mm had the highest cumulative displacement before failure in the L series arms at 4750 mm, but also had almost the lowest normalized energy dissipation capacity at 0.3 J/mm^3 ; where a specimen with $L = 315$ mm had 3000 mm of cumulative displacement before failure but 0.5 J/mm^3 of normalized energy dissipation capacity. This is because specimens with higher L values have more steel volume but also have lower stiffness and peak strength capacities compared to specimens with lower L values.

Conversely, specimens with different L values in *Phase II* showed similar performances in both cumulative displacement before failure and normalized cumulative energy dissipation capacity. For example, all tested specimens of the L series in *Phase II* had a normalized cumulative energy dissipation capacity between 0.12 J/mm^3 to 0.19 J/mm^3 , and a cumulative displacement before failure between 1544 mm to 1900 mm. This is likely caused by the failure pattern discussed in Section 3.6.2, since the failure mode for the specimens tested in *Phase II* are governed by axial compression forces, and any form of buckling will quickly lead to the failure of the specimen. For example, at a given shear deformation, the specimens with longer lengths are more susceptible to lateral torsional

buckling due to having a longer unbraced length, causing these arms to buckle earlier; whereas the specimens with shorter lengths do not suffer from having longer unbraced lengths but will experience a higher relative shear deformation demand comparatively, which causes a quicker development of higher compression stresses and reaching the critical buckling stress. Since both factors contribute to the onset of buckling initiation, therefore it is understandable that neither an increase or decrease in L will contribute to a noticeable increase in the performance of energy dissipation or displacement.

Based on the experimental results shown above, changes to aspect ratio b/t (by keeping b constant and increasing t) have proven to be more effective in delaying buckling than any changes in L . This delay of buckling initiation also resulted in observable increases to the performance of these flexural arms in both cumulative energy dissipation and displacement before failure. In *Phase II* with axial compression loads, the previously discussed behaviour in *Phase I* of a thinner specimen (S-L1-5) outperforming a thicker specimen (S-L1-4.3) can not be observed, since specimen S-L1-5A failed due to buckling and S-L1-4.3A did not buckle but instead failed due to fracture. Therefore, it can be expected that fuses with lower aspect ratios should have better performance in general.

3.11 New Proposed Design Equations for Strength

To check the accuracy of the proposed design equations, the following changes are proposed based on the experimental observations. First, the yield stress for specimen S-L1-7.5 is proposed to be changed from 508 MPa to 400 MPa like the rest of the S series specimens tested in *Phase I*, which is closer to the theoretical material properties associated with the yield strength of 50W steel. Second, L as presented in Eqs. (2), (3), (4), and (5) is

proposed to be changed to the parameter h , as shown in Fig. 12. This change is based on the mechanical derivations which ultimately associates the yield/plastic moment as the yield/plastic force, applied at the pin head of the flexural arm, multiplied by the moment arm which is captured more accurately by the parameter h than L in Fig. 12. Third, σ_y as presented in Eqs. (3) and (5) is proposed to be changed to the ultimate stress σ_u , as the preliminary derivations of the Eqs. (3) and (5) assumes the plastic moment condition that $M_y = \left(\frac{bh^2}{6}\right) \sigma_y$ and $M_p = 1.5 M_y = \left(\frac{bh^2}{4}\right) \sigma_y$. Since Q_p has been changed from the plastic strength to the peak strength, it seems more suitable to be using the ultimate strength of the material rather than the yield strength.

Table 5 - Summary of Proposed Changes to Force Design Equations

ID	Q_y/Q_{yt} (old)	Q_y/Q_{yt} (new)	Q_p/Q_{pt} (old)	Q_p/Q_{pt} (new)
S-L1-7.5	0.68	0.95	0.95	0.97
SL-L1-6	0.90	0.99	1.36	1.07
S-L1-5	0.87	0.95	1.40	1.09
S-L1-4.3	0.89	0.98	1.38	1.07
S-L1-7.5A	0.79	0.87	0.87	0.75
SL-L1-6A	0.94	1.03	1.22	0.95
S-L1-5A	0.90	0.99	1.28	0.98
S-L1-4.3A	0.91	0.99	1.23	0.94
L-L0.8-6	0.89	1.00	1.44	1.14
SL-L1-6	0.89	0.98	1.36	1.07
L-L1.2-6	0.87	0.94	1.31	1.00
L-L1.4-6	0.92	0.98	1.23	0.95
L-L0.8-6A	-	-	-	-
SL-L1-6A	0.94	1.03	1.22	0.95
L-L1.2-6A	0.95	1.03	1.20	0.91
L-L1.4-6A	0.92	0.98	1.14	0.86

Therefore, Table 5 summarizes the comparison between the new strength prediction values obtained after the proposed changes and the previous iteration of design equations. As seen, the proposed changes were able to more accurately predict both yield and peak

strengths for both *Phase I* and *Phase II* specimens. Previously, the old yield strength equations obtained an error within +13% for all specimens except S-L1-7.5 and S-L1-7.5A. Now, the new yield strength equations obtained an error within $\pm 6\%$ and includes specimen S-L1-7.5. More importantly, the new peak strength equations obtained an error range of +5% to -14% and includes S-L1-7.5, which is better than the old error range of -14% to -44% and does not include S-L1-7.5 or S-L1-7.5A. Lastly, none of the design equations were able to accurately estimate the strength capacity for S-L1-7.5A which was the only specimen that could not sustain the maximum displacement capacity. Therefore, to fully characterize the strength behaviour of flexural arms, further experimental and/or analytical investigations are still needed to establish more confidence in the proposed design equations.

4 Numerical Modeling

4.1 Description of the Model

Numerical models were developed using ABAQUS and validated against the experimental results of the flexural arms tested in the current study (ABAQUS, 2018). To simplify computational requirements associated with the developed model, only the flexural arm(s) out of the whole experimental set up were modeled using three dimensional (3D) planar shell elements. The nominal Young's Modulus, $E = 200 \text{ kN/mm}^2$, and plastic stress-strain relationships obtained from corresponding coupon test data were used to define the material properties for each model (Appendix B). The boundary conditions of the flexural arm were modeled as fixed at the bolt holes, with the out-of-plane movements restrained at the pin hole in the flexural arm. A rigid pin was also modeled to represent the loading pin used in the experimental assembly. The cyclic displacement protocol used in the experimental program was applied through this pin and imposed onto the flexural arm, while the axial compression forces of *Phase II* were applied onto the pin hole of the flexural arm. Fine meshing sizes were required near the pin hole for the convergence of the analytical model, as shown in Fig. 26.

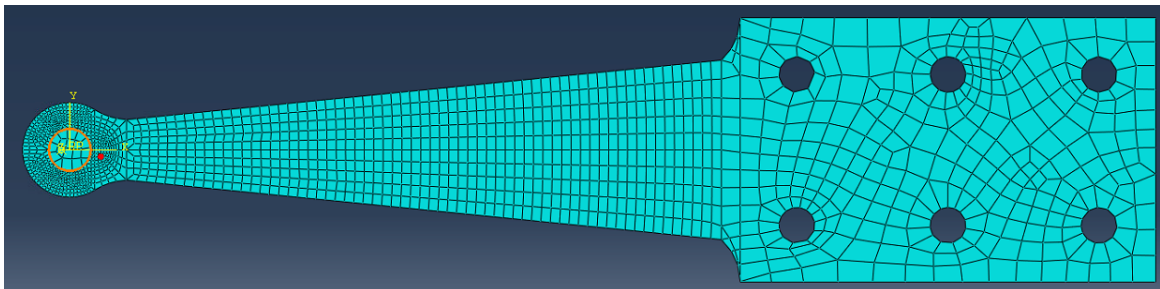


Figure 26 - Meshing Details for the Flexural Device in ABAQUS

To perform nonlinear buckling analysis in ABAQUS, an initial geometric imperfection was assigned to each flexural arm to initiate buckling (ABAQUS, 2018). This geometric imperfection was defined as the linear buckling modes of each arm in *Phase I* in the direction of shear deformation demand. This modeling technique was able to accurately capture both the buckling shape and behaviour of the specimens in both *Phase I* and *Phase II*, as seen in Figs. 27 and 28, for specimens SL-L1-6.0A and L-L0.8-6.0, respectively. More specifically, both the global and local buckling behaviours were accurately captured at the corresponding displacement levels in the analytical model.

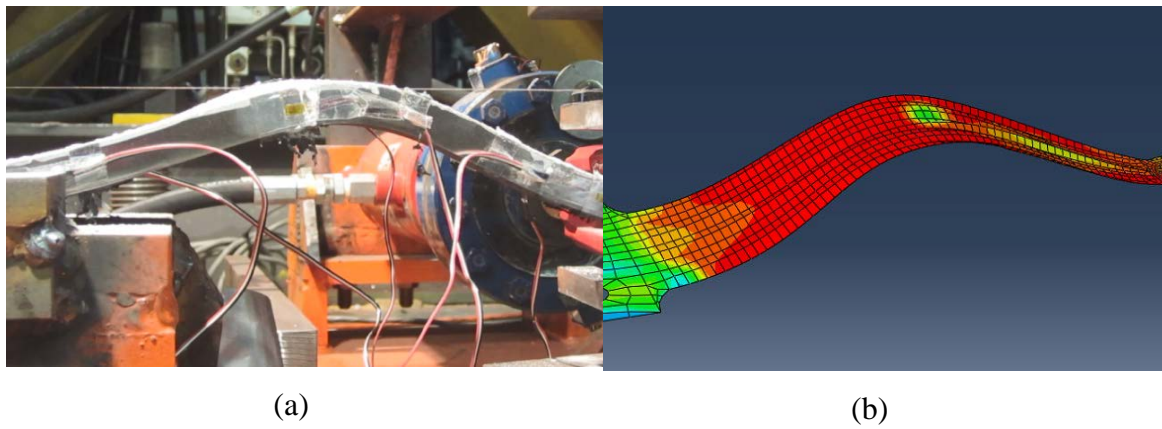


Figure 27 - Buckling Shape of SL-L1-6.0A; (a) Experimental (90 mm); (b) ABAQUS Result (90 mm)

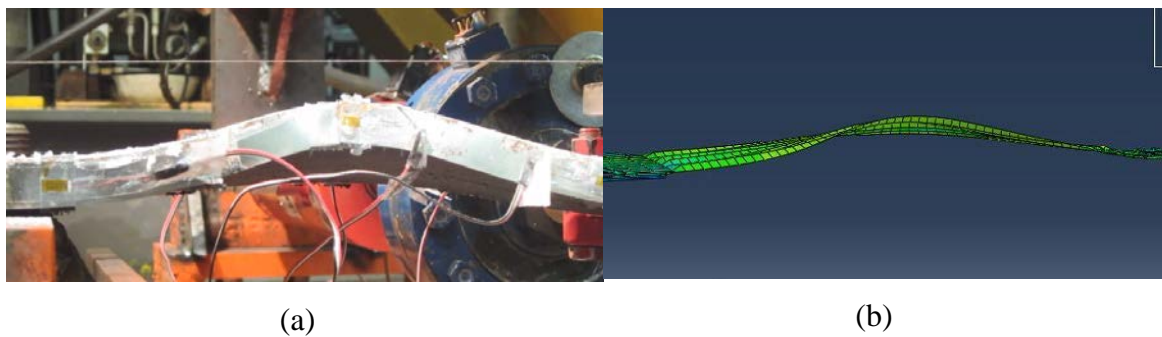


Figure 28 - Buckling Shape of L-L0.8-6.0; (a) Experimental (90 mm); (b) ABAQUS Result (90 mm)

4.2 Discussion of Analytical Results

The model load-displacement responses at the maximum displacement cycle for all fourteen arms are plotted against the experimental results in Figs. 29 to 35. Note that although no experimental data was captured for specimen L-L0.8-6.0A, the obtained analytical response is expected to be a good representation of its actual performance. Overall, the experimental hysteretic behaviours of each specimen were similar to that of the developed model. In particular, the monotonic loading curve of each specimen is represented well, with a maximum error of 10% when comparing the strength of each specimen at different displacement levels for all specimens except S-L1-7.5A. However, several differences can be seen when the model cyclic loops are compared to the experimental counterparts. First, both the loading and unloading stiffnesses of the analysis results are higher compared to the test results and the hysteresis loops are fuller in the analysis. These differences are understandable considering that the ABAQUS model does not account for the slack and the elastic deformations in the overall test setup. In addition, the bolt holes of the flexural arms were modeled as fixed in the analysis, which results in a more rigid and responsive assembly compared to the experimental test setup. Finally, the corners of the model hysteresis loops are not as rounded compared to the experimental results, this is because the material properties modeled in ABAQUS used an isotropic hardening model and does not consider the Bauschinger effect.

Overall, this model is good at capturing the buckling behaviour and estimating the monotonic loading curve of the flexural arms, but improvements can be expected if the whole test setup along with a more sophisticated material model is adapted; however,

computation time should be considered since each current analysis at the maximum displacement cycle takes about 5 hours to complete, even with the current simplified model. Furthermore, although the current model can perform cyclic analysis, the completion time required is about 3 days per specimen which is acceptable for design checks on future specimens but quickly becomes unfeasible for any large parametric or sensitivity analyses. Results of the cyclic analysis can be found in Appendix H.

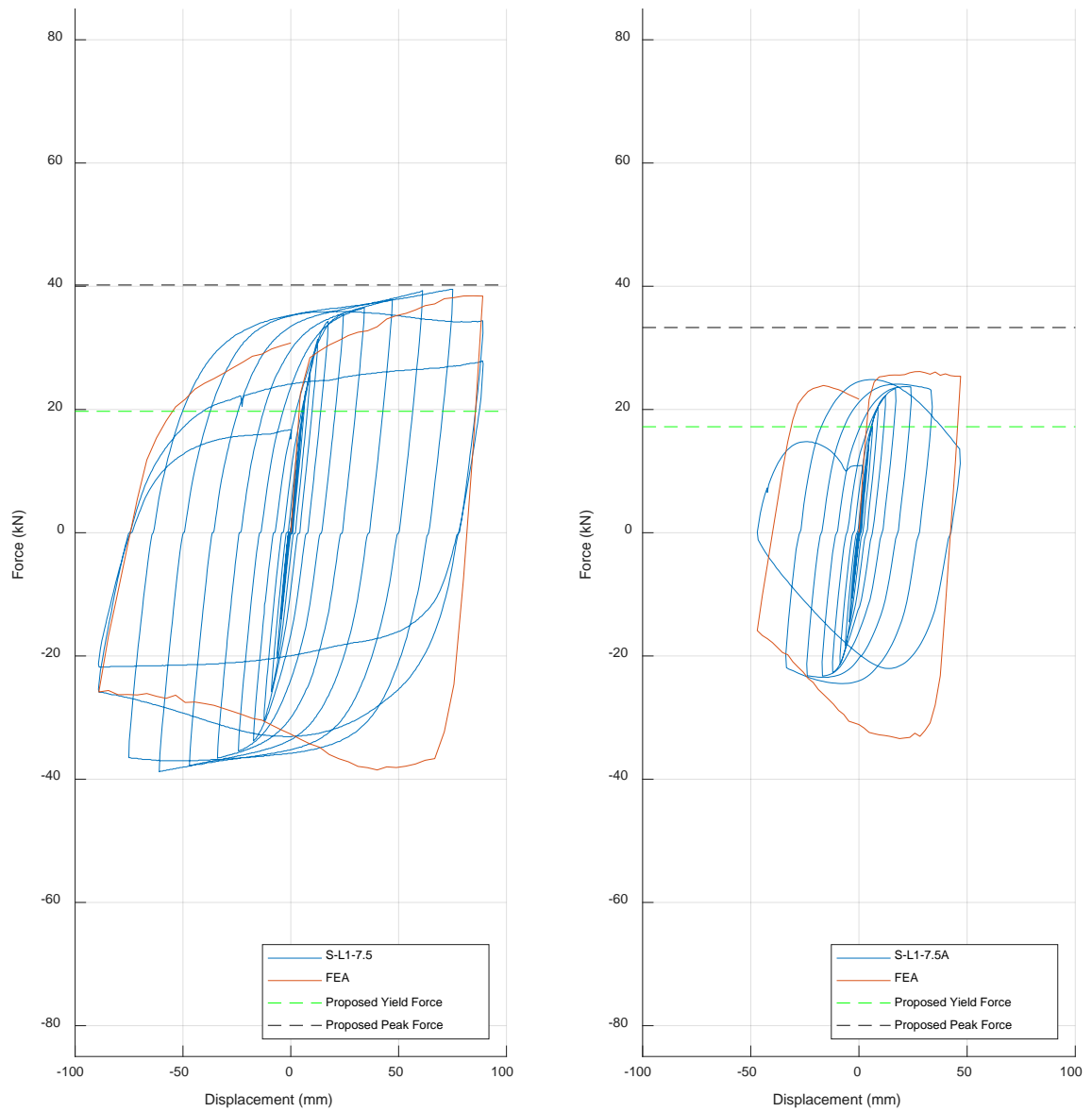


Figure 29 - Hysteresis Plots for S-L1-7.5 and S-L1-7.5A

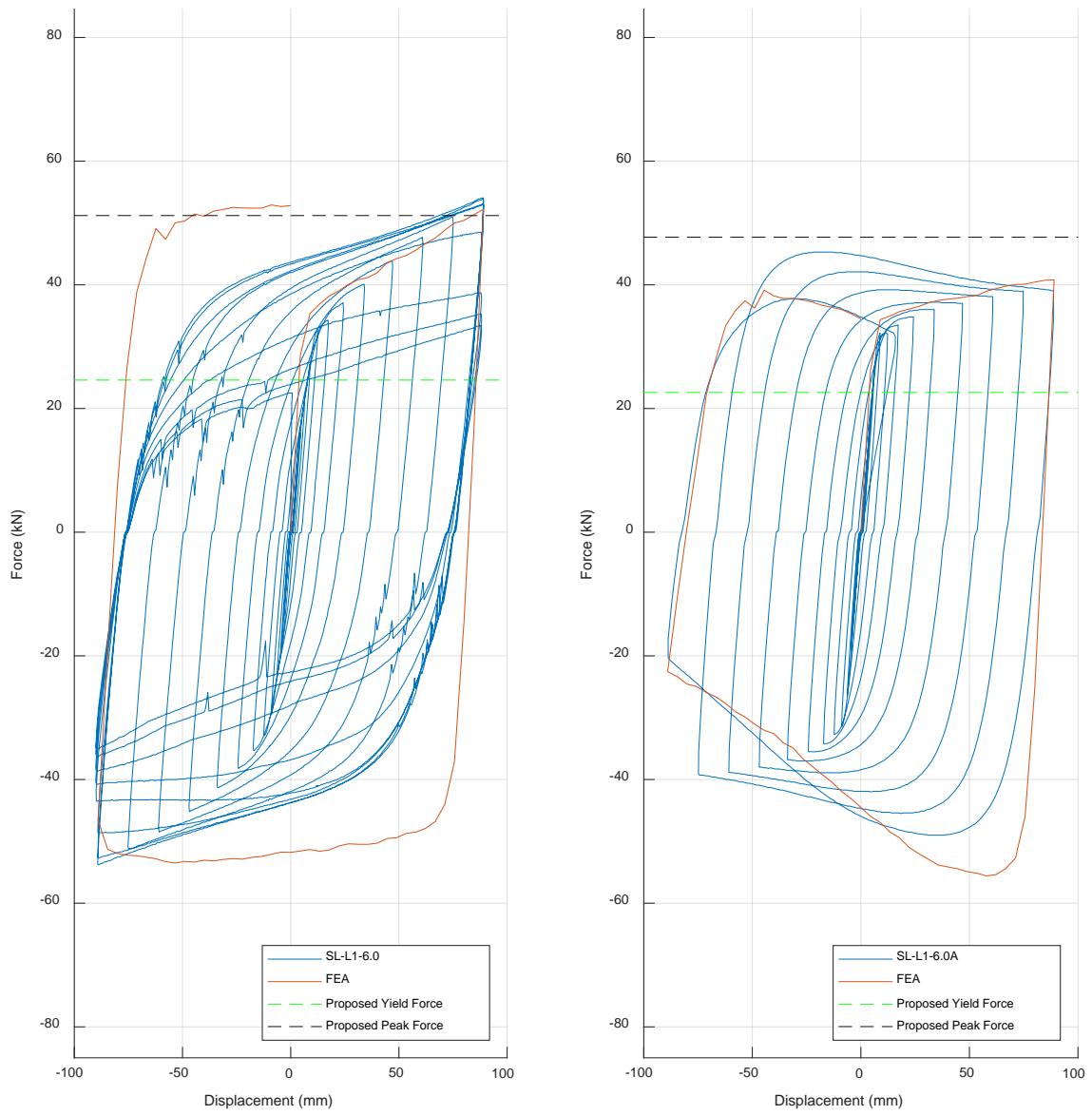


Figure 30 - Hysteresis Plots for SL-L1-6.0 and SL-L1-6.0A

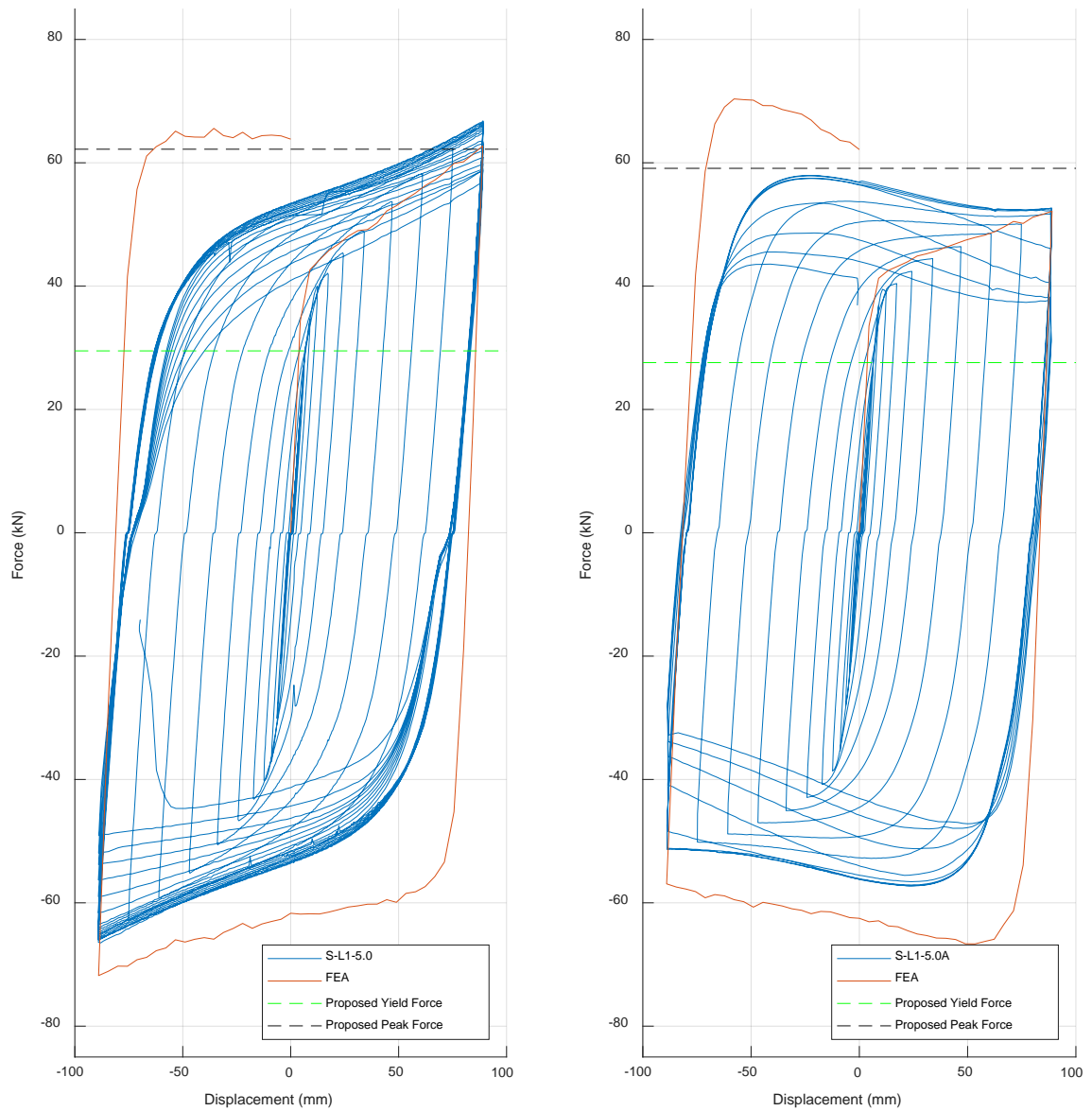


Figure 31 - Hysteresis Plots for S-L1-5 and S-L1-5A

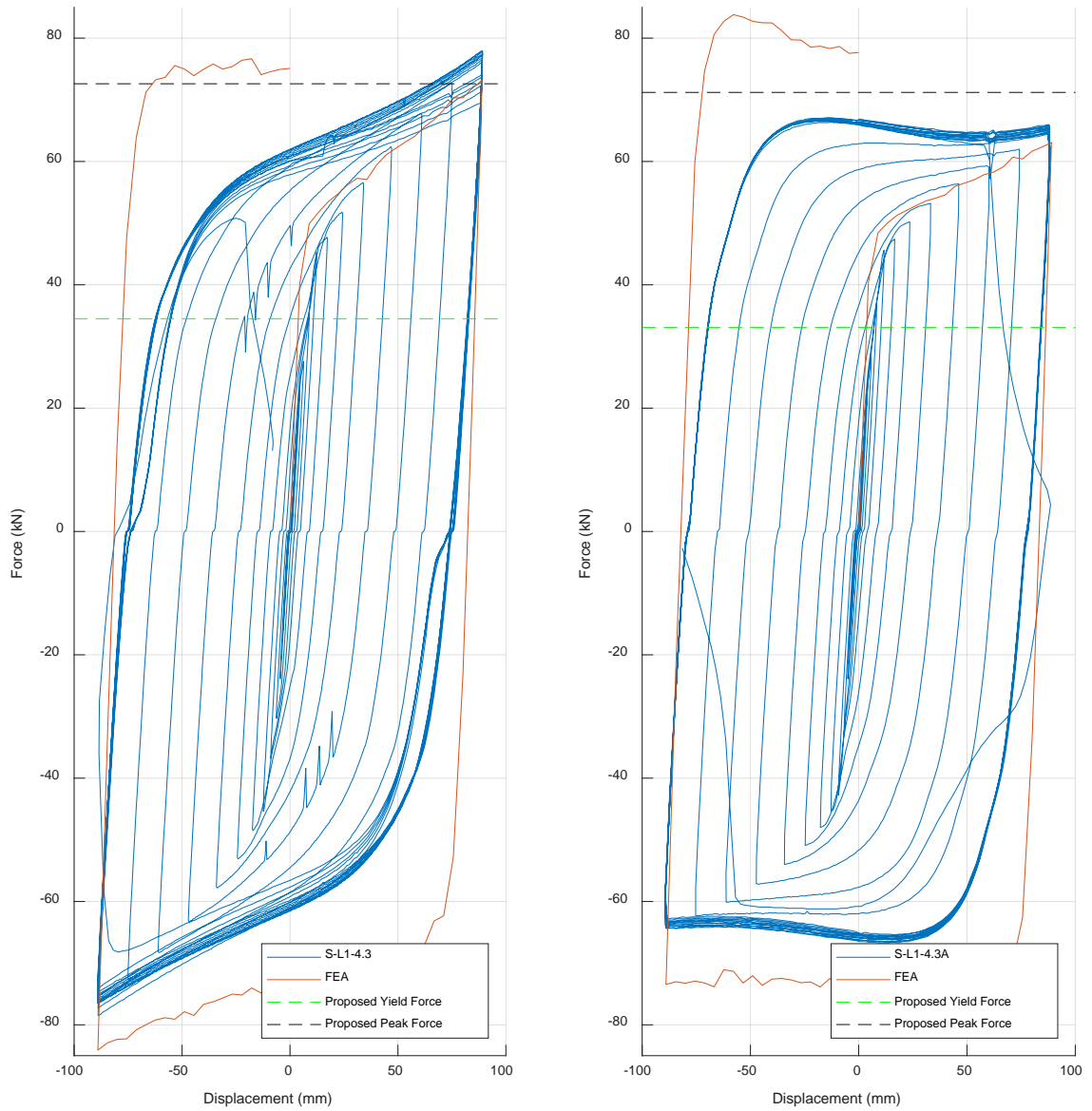


Figure 32 - Hysteresis Plots for S-L1-4.3 and S-L1-4.3A

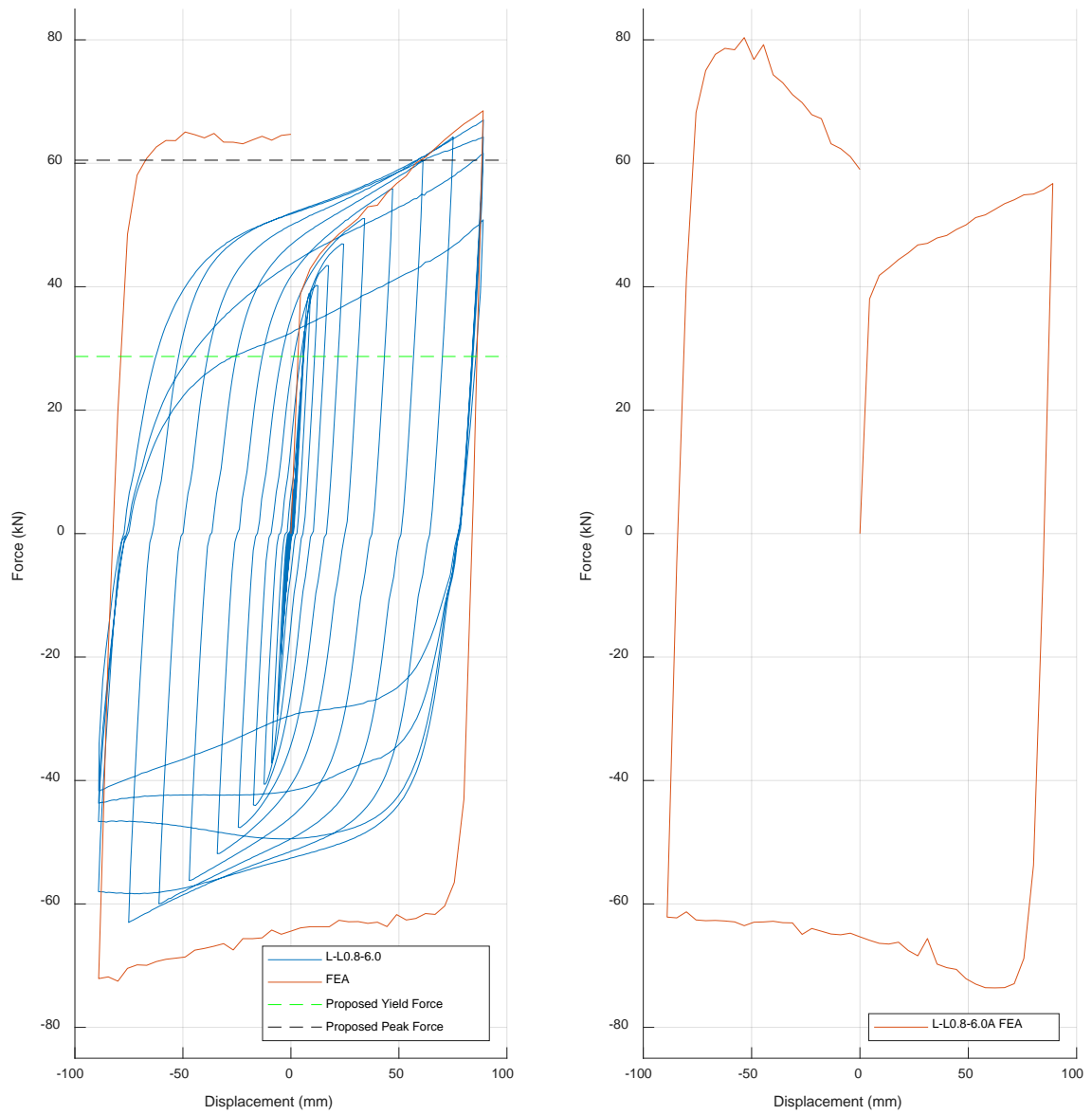


Figure 33 - Hysteresis Plots for L-L0.8-6.0 and L-L0.8-6.0A

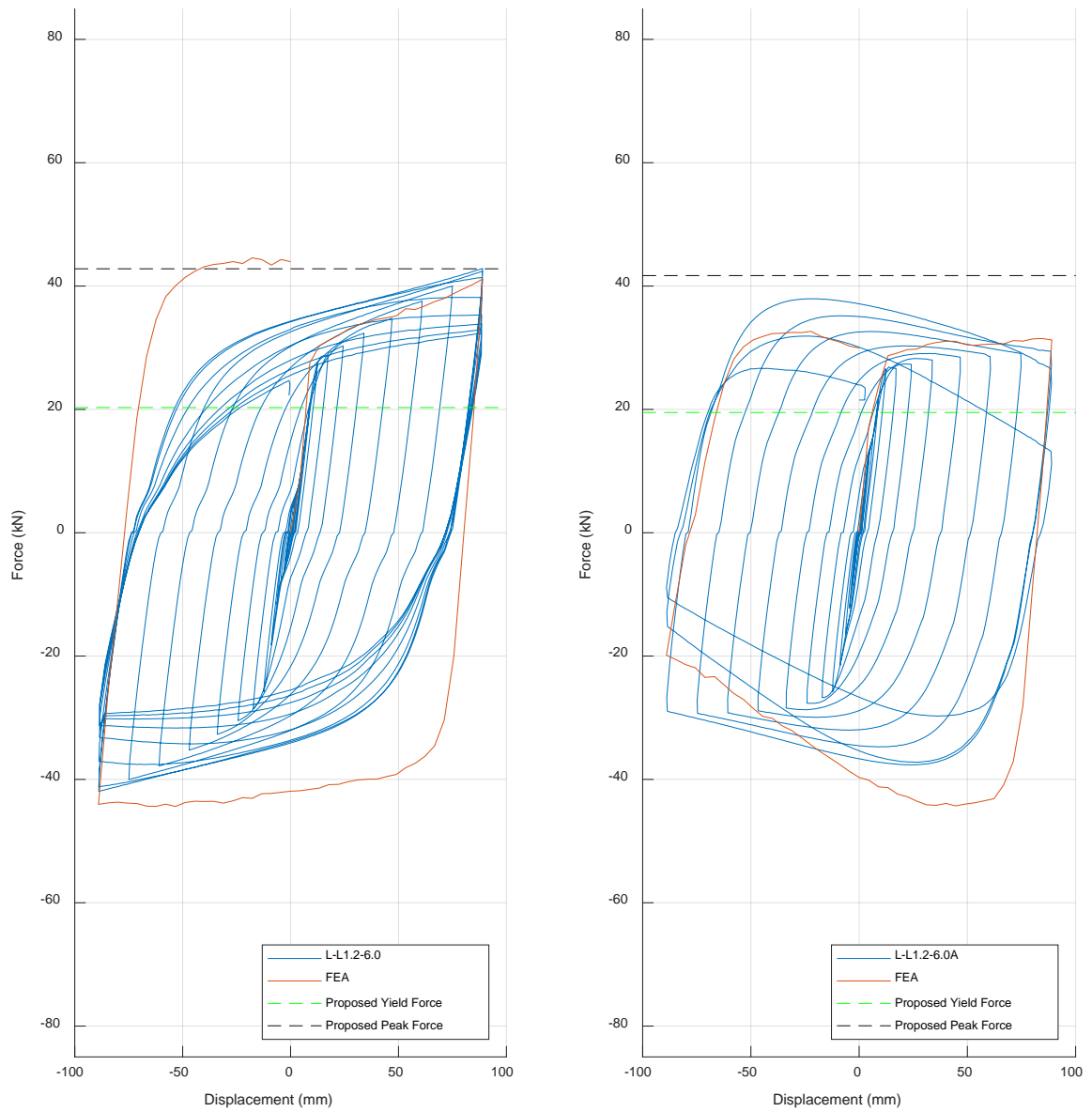


Figure 34 - Hysteresis Plots for L-L1.2-6.0 and L-L1.2-6.0A

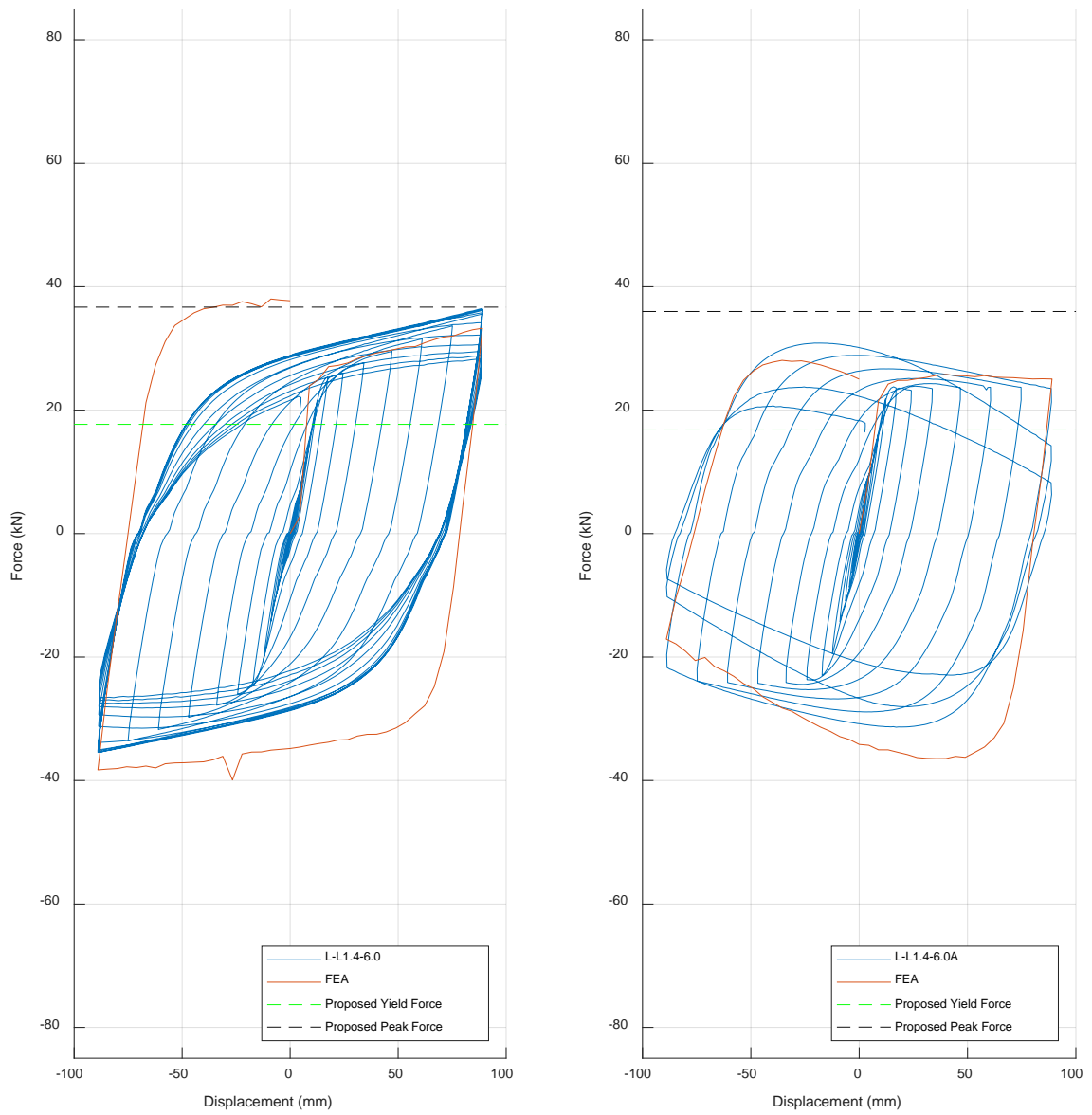


Figure 35 - Hysteresis Plots for L-L1.4-6.0 and L-L1.4-6.0A

5 Conclusions

A total of fourteen flexural arms were designed and thirteen were tested to investigate their behaviour as energy dissipation devices for CRMWs. Similar to previous strong-axis flexural yielding hysteretic dampers, the energy dissipation mechanism of flexural arms is based on the strong-axis bending of the steel tapered cantilever arm. However, unlike previous studies, the performance of these flexural arms was investigated under both cyclic displacement and axial compression forces simultaneously. Specifically, new design equations for yield and plastic strength that accounts for axial compression forces were proposed and validated against the experimental results. These flexural arms can be fabricated from any grade of steel plate using the proposed design equations, with no special fabrication techniques involved. The development of an easily manufactured and replaceable EDD with the ability to also resist sliding demands is expected to enhance the overall performance of CRMWs. Major findings and recommendations are presented as follows:

5.1 Performance of Flexural Arms without Axial Loads

Seven flexural arms were tested in *Phase I* which were split into the S series and the L series. The S series had a constant $L = 1.0L_{ref}$ but varied b/t from 4.3 to 7.5 (varied t while keeping $b = 95$ mm) to investigate the effects of b/t . Meanwhile the L series had a constant $b/t = 6$ but varied L from $0.8L_{ref}$ to $1.4L_{ref}$ to investigate the effects of L . The flexural arms sustained full hysteretic behavior without buckling initiation up to at least 18% shear deformation (Δ/L), except for specimen S-L1-7.5. Furthermore, all specimens sustained

two or more cycles at maximum actuator displacement (90 mm, which corresponds to 5.7% reference wall drift) before ultimately failing to strength degradation or fracture.

5.2 Performance of Flexural Arms with Axial Loads

Seven flexural arms were proposed in *Phase II* with identical geometrical configurations as *Phase I*, but with the addition of 30 kN of axial compression. Only six arms were tested due to a laboratory error. This axial compression was converted to varying values of axial stress for each specimen based on the location of intended yielding at $x = 0.5L$ (Table 4). The addition of axial stresses decreased the displacement capacity of the flexural arms before buckling initiation by about 4% shear deformation, except S-L1-7.5A, which results in at least 14% shear deformation before buckling for flexural arms under 21 MPa to 37 MPa of axial stress. Moreover, these axial stresses can reduce the energy dissipation capacities by up to 80% of their original value in *Phase I* (Table 3 and 4), while also reducing the cumulative displacement before strength degradation and failure, by up to 62% and 67% of their original value, respectively. Finally, the majority of specimens (4 out of 6) sustained the first 90 mm cycle of maximum actuator displacement with minimal to no buckling, which may be attributed to the buckling resistance of thicker specimens (S-L1-4.3A and S-L1-5.0A) or the higher relative shear deformation capacities of longer specimens (L-L1.4-6.0A and L-L1.2-6.0A).

5.3 Force Capacity of Flexural Arms

The initial design equations to determine the nominal strengths of the flexural arms are proposed in Eqs. (2) and (3) for arms without axial forces, and subsequently Eqs. (4) and

(5) for with axial forces. Comparison with test results shows that these equations generally predicted the yield strengths with an error less than +13% for all specimens, except for specimens S-L1-7.5 and S-L1-7.5A. As discussed previously, the true peak strengths for these flexural arms were not reached for most of the specimens due to limitation in the maximum actuator stroke; however, comparison using the current observed peak strengths and Eqs. (3) and (5) shows an error range of -14% to -44% for all specimens, except for specimens S-L1-7.5 and S-L1-7.5A. These two specimens were generally excluded from any comparison for the following reasons, additional to general sources of error discussed previously. First, both specimens S-L1-7.5 and S-L1-7.5A was found to have no yielding plateau and thus affected its experimental yield stress values used by the Eqs. (2), (3), (4) and (5) (see Appendix A). Second, specimen S-L1-7.5A buckled unexpectedly and its behavior was seemingly dominated by the axial compression force, as depicted in Fig. 68 (Appendix D) and categorized by the rapid transition between the stages of buckling initiation and failure.

Based on the experimental observations, three changes were proposed and thus new design equations were established. These changes accounted for the lack of a yielding plateau observed in specimen S-L1-7.5 and adjusted the length variable L , as presented in Eqs. (2), (3), (4), and (5) to be changed to the parameter h . Furthermore, σ_y was changed to the ultimate stress σ_u , for specimens in *Phase II*. These changes were able to increase the accuracy of the initial design equations and were discussed in Section 3.11. Overall, the new equations obtained an error within $\pm 6\%$ and -5% to +14% for yield and peak strengths, respectively. Comparatively, the error ranges of the initial design equations were within

+13% and -14% to -44% for yield and peak strengths, respectively. These proposed changes were also able to capture the behaviour of specimen S-L1-7.5, but more studies are still needed to fully understand the strength capacity of flexural arms.

5.4 Displacement Capacity of Flexural Arms

As previously discussed, the true peak shear deformation capacities before buckling initiation, strength deterioration, and failure, were not obtained for most specimens due to the limitations of maximum actuator displacement (90 mm). Specimens that experienced any of these three key performance stages after multiple cycles at maximum actuator displacement did not demonstrate their true peak shear deformation capacity due to maximum displacement demand. Furthermore, no design specifications were found for the flexural arm and its displacement capacities on any of the three key stages. This makes the current error (or lack of) in true displacement performance hard to quantify.

Therefore, the design of the current flexural arm started with the estimated performance before buckling based on previous studies on similar strong-axis flexural devices with an aspect ratio $b/t = 6$, and the current targeted demands for displacement and force. Geometry limits, due to space constraints, can often dictate the initial design parameters as well. The shear deformation capacity of the flexural arms before buckling initiation is the focus in the current discussion, as it is often accompanied by both strength degradation and/or failure, particularly in specimens with axial compression forces. All performance values for shear deformation before buckling were summarized previously in Table 4.

The current experimental results show that the performance for flexural arms with $b/t = 6$ and varying L supports the preliminary displacement prediction. Therefore, for flexural arms with $b/t = 6$ and varying L , the displacement capacity before buckling initiation can be expected to be at least 18% shear deformation without axial stresses or at least 15% shear deformation with 30 MPa of axial stresses (at the location of intended yielding, $x = 0.5L$). Moreover, changes to b/t (by increasing t and keeping b constant) were observed to have the biggest influence in delaying the onset of buckling of flexural arms, but no clear quantitative relationships could be defined due to the limitations of maximum actuator stroke. However, future designers can follow the current design recommendations and reference the new experimental performance values for flexural arms with $b/t = 7.5, 6.0, 5.0,$ and 4.3 shown in Table 4. In general, thicker specimens (with $b/t = 5.0$ and 4.3) should be expected to have a displacement capacity before buckling initiation of at least 28% shear deformation without axial stresses and at least 24% shear deformation with 25 MPa of axial stress. All recommendations are based on the observations made about the current specimens, and further experimental and/or analytical investigations are still required to establish more in-depth guidelines on the displacement capacity of flexural arms.

5.5 Future Research Recommendations

Based on the observations and suggestions made previously, further investigations of the following topics are recommended in order to establish better guidelines and enhance the accuracy of the estimates for strength and displacement capacities.

5.5.1 Maximum Actuator Displacement

The limitation of maximum actuator displacement has been discussed multiple times and should be avoided in future studies to evaluate the true peak strength and displacement capacities of the flexural devices. More tests should be conducted with no limitations in shear deformation demand, especially considering the flexural devices with lower b/t ratios so that the effect of these parameters can be fully quantified.

5.5.2 Empirical Estimates of Displacement Capacity

The current set of fourteen arms were not sufficient to fully establish a confident range of displacement capacities for all of the parametric combinations in this study. Only the displacement performance of flexural device, with constant aspect ratio of $b/t = 6$ and varying L , were supported by multiple data points (4 data points in *Phase I* and 3 in *Phase II*). More tests should be conducted with the current parametric combinations, as well as additional combinations, to empirically establish the displacement capacities of the flexural device.

5.5.3 Theoretical Estimates of Displacement Capacity

The displacement capacity of the flexural device before buckling initiation can be theoretically established, if desired. This can be performed by calculating the compression stresses of the whole flexural at every displacement level and comparing it to the critical buckling stress, which can also be found. This can then be validated through the experimental program and reduce the need to empirically established the displacement capacity before buckling initiation. Though, finding the ultimate displacement capacities

might still be easier through experimentation. Furthermore, this method can also obtain a more accurate location for buckling initiation.

5.5.4 Axial Compression Force

More tests should also be performed with greater variances in axial compression forces to fully quantify the effect of axial stress levels on the performances of flexural arms, particularly on the influences towards displacement performances. In addition, the further investigation of axial stresses may result in the introduction of a new variable to the design equations. This will ideally capture the behaviour of all flexural arms under any axial stress, specifically the thinner specimens which are the most susceptible to buckling failure.

5.5.5 Design Equations

More experimental data points will help to validate and/or improve the accuracy of the design equations for strength. In addition, further efforts should be made to improve the approximate derivation procedures used in *Phase II*. Although the theoretical estimates obtained through the new proposed design equations were promising (Table 5), many aspects were assumed and simplified overall. Additional thoughts and considerations to the derivation procedure, along with more experimental data, will increase the accuracy of the design equations.

5.5.6 Numerical Modeling

The current numerical model was able to capture the buckling behaviour and deformation with good accuracy. Further improvements can be expected if the model included the test setup, along with a more sophisticated material model and a smaller time step. More

specifically, smaller time steps will help smooth out the jagged response of the analysis results and more sophisticated material models will better capture the rounded corners of the experimental hysteretic loops.

6 References

Abaqus (2018). *Abaqus analysis user's manual*, version 6.14.

Aiken, I., Nims, D., Whittaker, A., and Kelly, J. (1993). “Testing of passive energy dissipation systems.” *Earthquake Spectra*, Vol. 9, No. 3, Earthquake Engineering Research Institute, California.

ASTM Standard E8. (2003). “Standard test methods for tension testing of metallic materials.” *American Society for Testing and Materials*, pp. 62-79.

Bergman, D. M. and Goel, S. C. (1987). “Evaluation of cyclic testing of steel plate devices for added damping and stiffness.” *Report No. UMCE87-10, the University of Michigan*.

Chan, R. W. K. and Albermani, F. (2008). “Experimental study of steel slit damper for passive energy dissipation.” *Engineering Structures*, 30 (2008), pp. 1058-1066.

Chancellor, N., Eatherton, M., Roke, D., and Akbas, T. (2014). “Self-centering seismic lateral force resisting systems: High performance structures for the city of tomorrow.” *Buildings*, Vol. 4, No. 3, pp. 520-548.

EERI (2005). *World housing project*; Retrieved from <http://www.world-housing.net/>

Ezzeldin, M., El-Dakhkhni, W., and Wiebe, L. (2017). “Experimental assessment of the system-level seismic performance of an asymmetrical reinforced concrete block-wall building with boundary elements.” *Journal of Structural Engineering*, 143(8), 04017063

- FEMA 461. (2007). “Interim testing protocols for determining the seismic performance characteristics of structural and non-structural components.” *Federal Emergency Management Agency*.
- Garivani, S., Aghakouchak, A. A., and Shahbeyk, S. (2016). “Numerical and experimental study of comb-teeth metallic yielding dampers.” *International Journal of Steel Structures*, 16 (2016), pp. 177-196.
- Holden, T., Restrepo, J. I., and Mander, J. B. (2002). “Seismic performance of precast reinforced and prestressed concrete walls.” *Journal of Structural Engineering, ASCE*, Vol. 129, No.3, pp. 286-296.
- Kaminosono, T., Teshigowara, M., Hiraishi, H., Fujisawa, M., and Nakaoka, A. (1988). “Experimental study on seismic performance of reinforced masonry walls.” *Proc., 9th World Conf. on Earthquake Engineering*, Japan Association for Earthquake Disaster Prevention, Japan, pp. 109–114.
- Kobori, T., Miura, Y., Fukusawa, E., Yamada, T., Arita, T., and Takenake, Y. (1992). “Development and application of hysteresis steel dampers.” *Proc. 11th World Conference on Earthquake Engineering*, pp. 2341-2346.
- Kobori T. (2017). *Honeycomb Damper*; Retrieved from <http://www.kobori-takken.co.jp/English/randd/ctrl41.html>.

- Laursen, P. T. and Ingham, J. M. (2004). “Structural Testing of Enhanced Post-Tensioned Concrete Masonry Walls.” *Journal of Structural Engineering, ASCE*, Vol. 130, No.10, pp. 1497-1505.
- Ma, X., Borchers, E., Pena, A., Krawinkler, H., Billington, S., and Deierlein, G. G. (2010). “Design and behaviour of steel shear plates with openings as energy-dissipating fuses.” *The John A. Blume Earthquake Engineering Center* (2010), Report No.173.
- Makris, N. and Roussos, Y. (1998). “Rocking response and overturning of equipment under horizontal-type pulses.” *Report No PEER-98/05*, University of California, Berkeley.
- Matsumura, A. (1986). “Shear strength of reinforced hollow unit masonry walls.” *2nd Meeting of the U.S.-Japan Joint Technical Coordinating Committee on Masonry Research, U.S. Japan Cooperative Research Program, CO*.
- Priestley, M. J. N., Sritharan, S., Conley, J. R., and Pampanin, S. (1999). “Preliminary results and conclusions from the PRESSS five-story precast concrete test building.” *PCI Journal*, Vol. 44, No.6, pp. 42-67.
- Restrepo, J. I. and Rahman, A. (2007). “Seismic performance of self-centering structural walls incorporating energy dissipators.” *Journal of Structural Engineering, ASCE*, Vol. 133, No.11, pp. 1560-1570.

- Saeedi, F., Shabakhty, N., and Mousavi, S. (2016). “Seismic assessment of steel frames with triangular-plate added damping and stiffness devices.” *Journal of Constructional Steel Research*, Vol. 125, pp. 15-25.
- Seif Eldin, H. M. and Galal, K. (2017). “In-plane seismic performance of fully routed reinforced masonry shear walls.” *Journal of Structural Engineering, ASCE*, Vol. 143, No.7, 04017054.
- Shing, P., Schuller, M., and Hoskere, V. (1990). “In-plane resistance of reinforced masonry shear walls.” *Journal of Structural Engineering, ASCE*, Vol. 116, No.3, pp. 619–640.
- Sveinsson, B. I., Sucuoglu, H., and McNiven, H. D. (1985). “Cyclic loading tests of masonry single piers - Volume 4: Additional tests with height to width ratio of 1.” *Report No. UCB/EERC-85/15*, Earthquake Engineering Research Centre, University of California, Berkeley, CA.
- Toranzo, L. A. (2002). “The use of rocking walls in confined masonry structures: a performance-based approach.” *Ph.D. Dissertation*, Department of Civil Engineering, University of Canterbury, New Zealand.
- Toranzo, L. A., Restrepo, J. I., Carr, A. J., and Mander, J. B. (2004). “Rocking confined masonry walls with hysteretic energy dissipators and shake-table validation.” *Proc. 13th World Conference on Earthquake Engineering*, Paper No.248.

- Toranzo, L. A., Restrepo, J. I., Mander, J. B., and Carr, A. J. (2009). “Shake-table tests of confined-masonry rocking walls with supplementary hysteretic damping.” *Journal of Earthquake Engineering*, Vol. 13, No.6, pp. 882-898.
- Tsai, K. C., Chen, H. W., Hong, C. P., and Su, Y. F. (1993). “Design of steel triangular plate energy absorbers for seismic-resistance construction.” *Earthquake Spectra*, Vol. 9, pp. 505-528.
- Vargas, R. E. and Bruneau, M. (2006). “Seismic response and design of buildings with metallic structural fuses.” *Proceedings of the Fifth International Conference on Behaviour of Steel Structures in Seismic Areas (STESSA), August 14-17, Yokohama, Japan*, pp. 99–103.
- Voon, K., and Ingham, J. (2006). “Experimental in-plane shear strength investigation of reinforced concrete masonry walls.” *Journal of Structural Engineering, ASCE*, Vol. 132, No.3, pp. 400–408.
- Xia, C. and Hanson, R. (1992). “Influence of ADAS element parameters on building seismic response.” *Journal of Structural Engineering, ASCE*, Vol. 118, pp. 1903-1918.

Appendix A – Coupon Test Data

- A summary of the in-depth numerical values for yield and ultimate stress can be found in the table below, along with the elongation percentage at fracture
- The title of each graph is a reference to the corresponding specimens, two tests were done for each specimen.

Table 6 - Material Test Data

	b/t	L	Yield Stress, F _y (MPa)			Ultimate Stress, F _u (MPa)			Elongation at fracture (%)		
			Test 1	Test 2	Mean	Test 1	Test 2	Mean	Test 1	Test 2	Mean
Non Axial	7.5	L1	515	500	508	550	540	545	19%	19%	19%
	6	L1	400	400	400	555	555	555	23%	23%	23%
	5	L1	400	400	400	560	563	562	23%	23%	23%
	4.3	L1	400	400	400	564	562	563	22%	20%	21%
	6	L0.8	385	385	385	544	540	542	23%	23%	23%
	6	L1.2	394	390	392	552	550	551	23%	23%	23%
	6	L1.4	393	390	392	543	540	542	23%	23%	23%
Axial	7.5	L1	380	380	380	480	480	480	20%	20%	20%
	6	L1	390	390	390	537	540	539	24%	24%	24%
	5	L1	391	393	392	548	555	552	23%	23%	23%
	4.3	L1	400	397	399	569	563	566	23%	23%	23%
	6	L0.8	392	397	395	547	551	549	23%	23%	23%
	6	L1.2	395	396	396	554	555	555	24%	24%	24%
	6	L1.4	394	390	392	550	547	549	24%	24%	24%

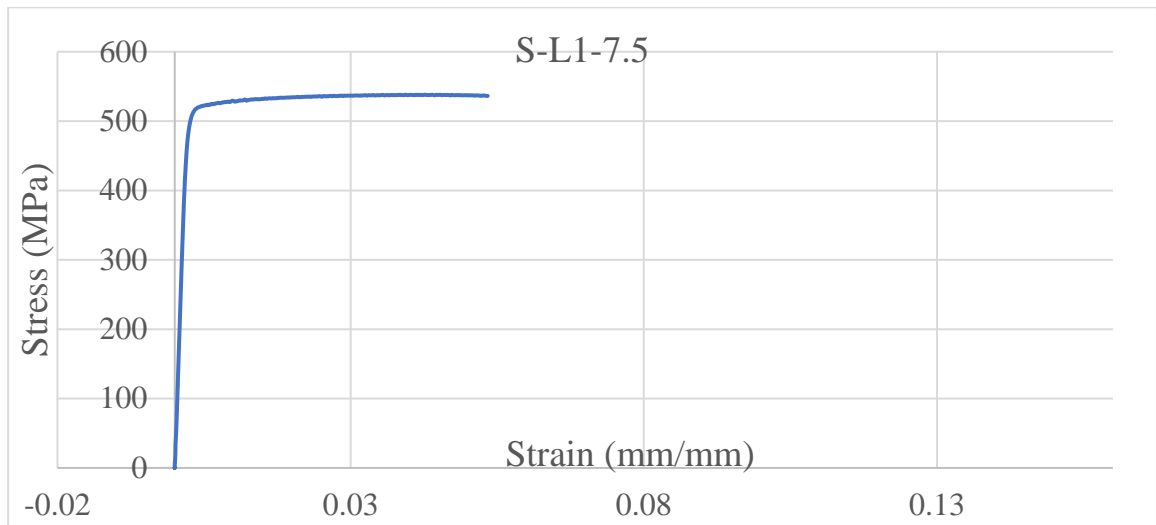


Figure 36 - Stress-Strain Curve for S-L1-7.5

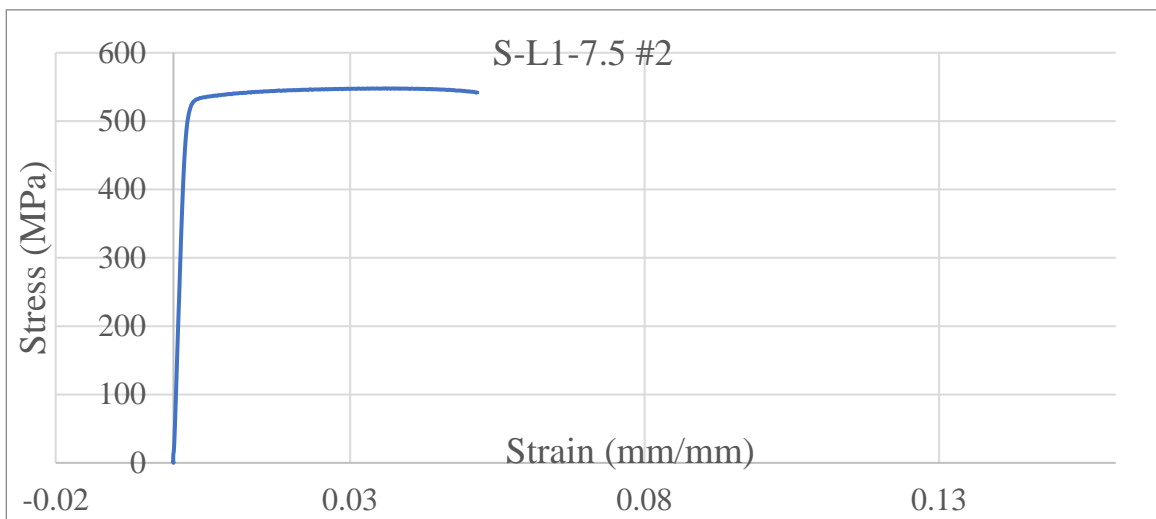


Figure 37 - Stress-Strain Curve for S-L1-7.5

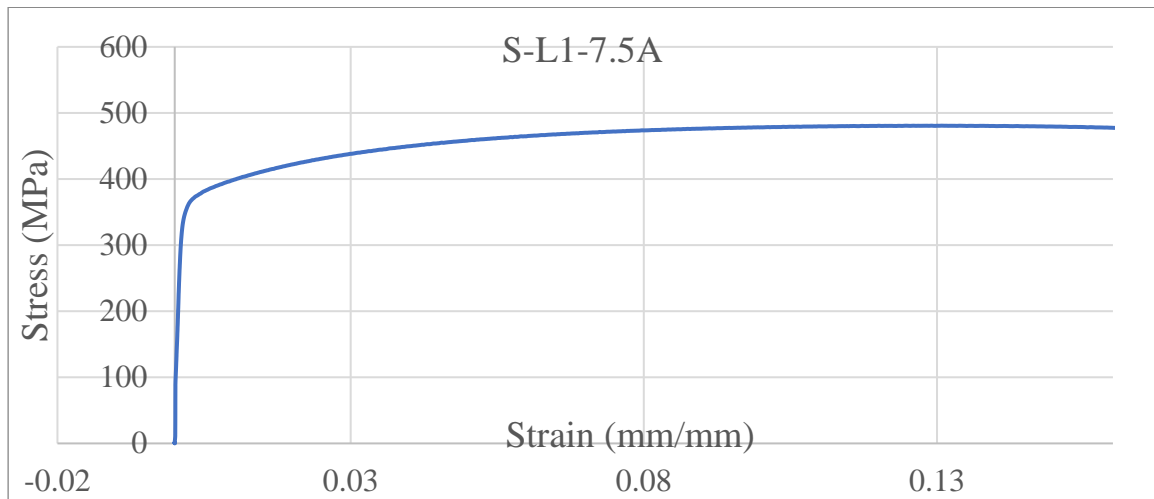


Figure 38 - Stress-Strain Curve for S-L1-7.5A

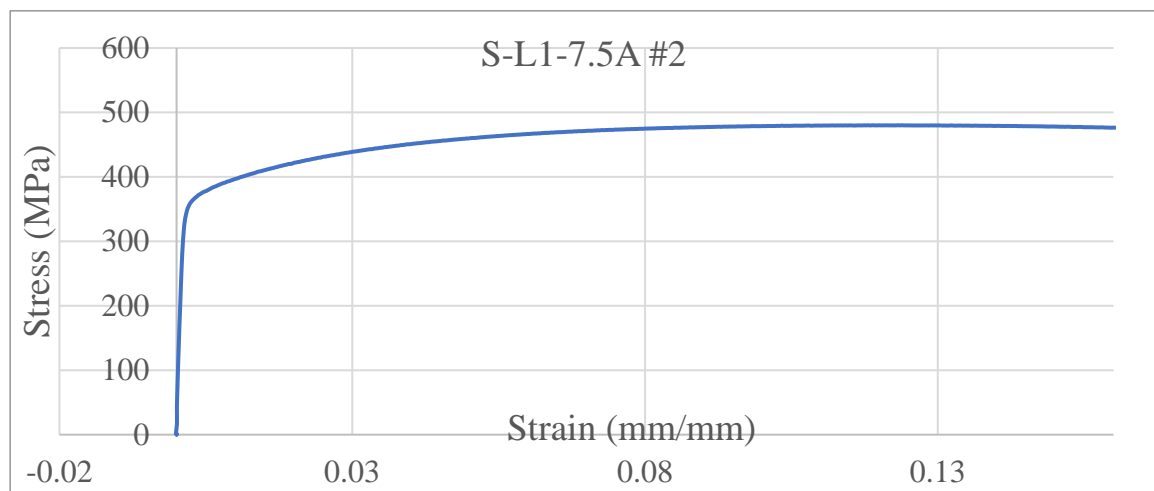


Figure 39 - Stress-Strain Curve for S-L1-7.5A

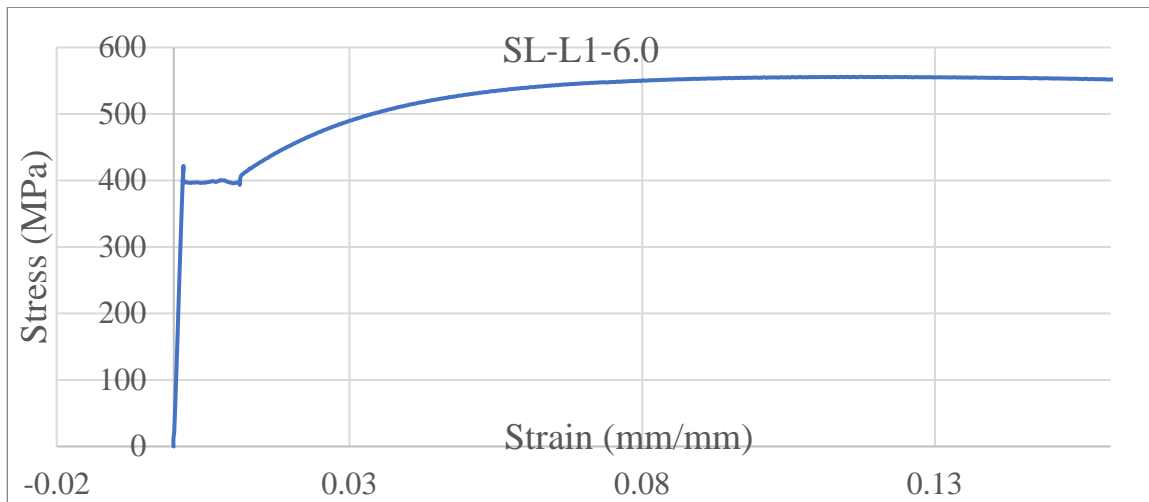


Figure 40 - Stress-Strain Curve for SL-L1-6.0

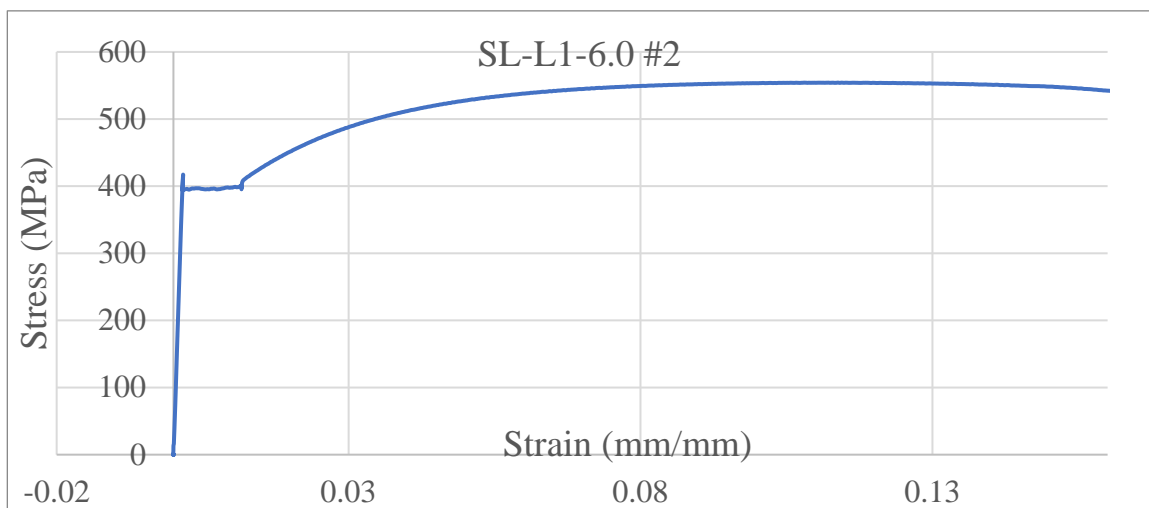


Figure 41 - Stress-Strain Curve for SL-L1-6.0

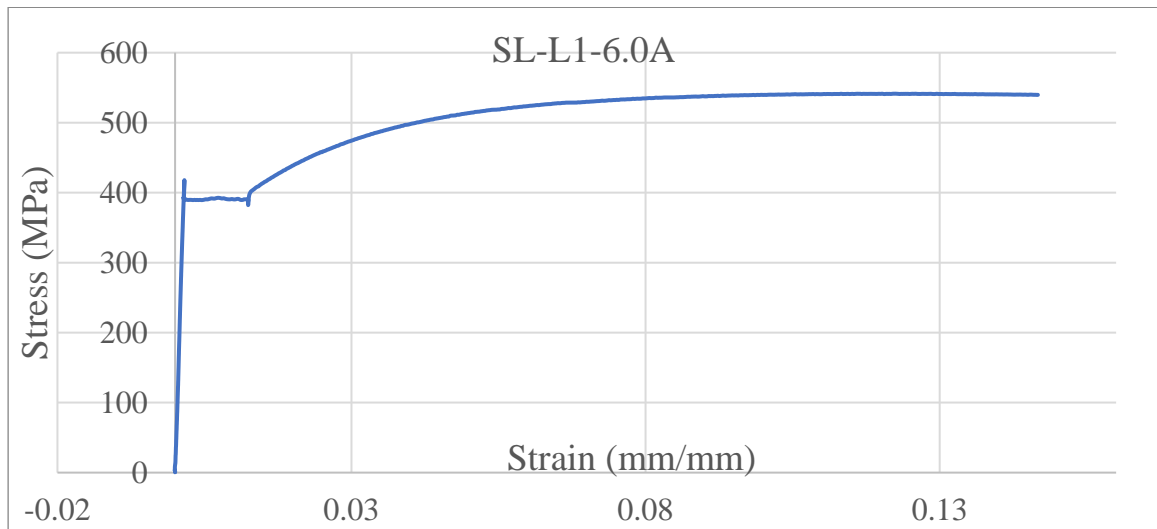


Figure 42 - Stress-Strain Curve for SL-L1-6.0A

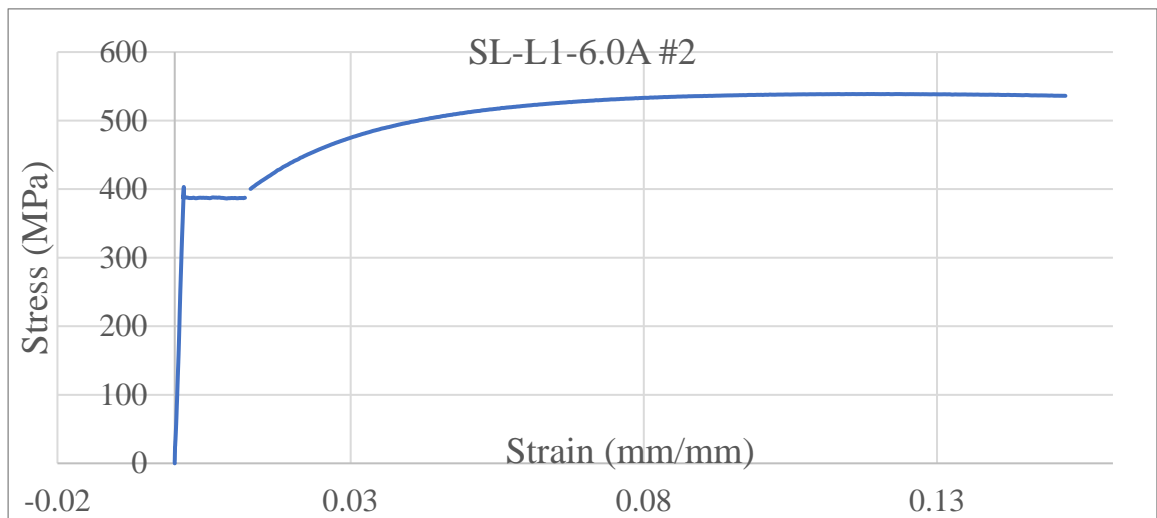


Figure 43 - Stress-Strain Curve for SL-L1-6.0A

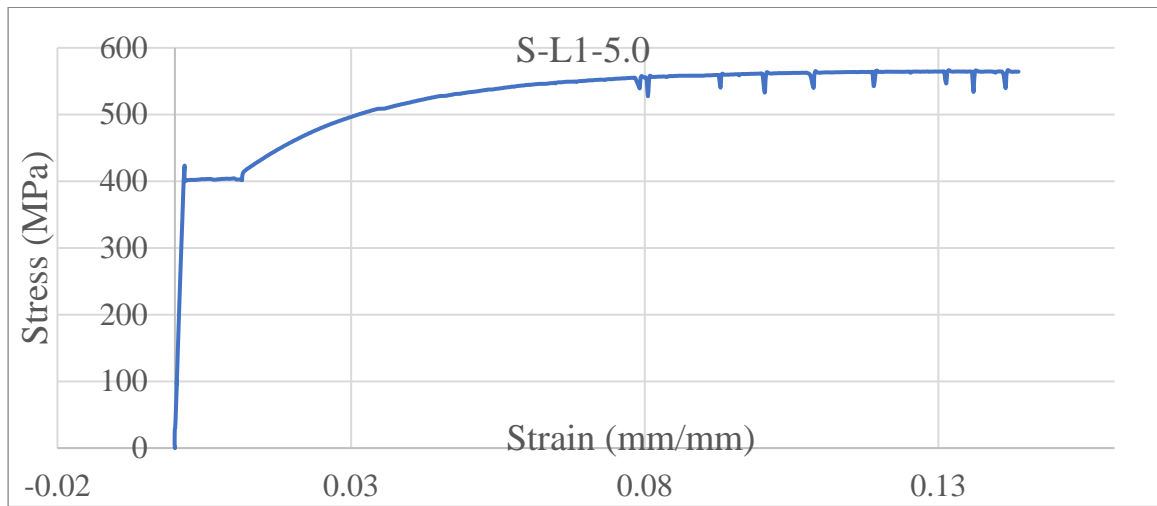


Figure 44 - Stress-Strain Curve for S-L1-5.0

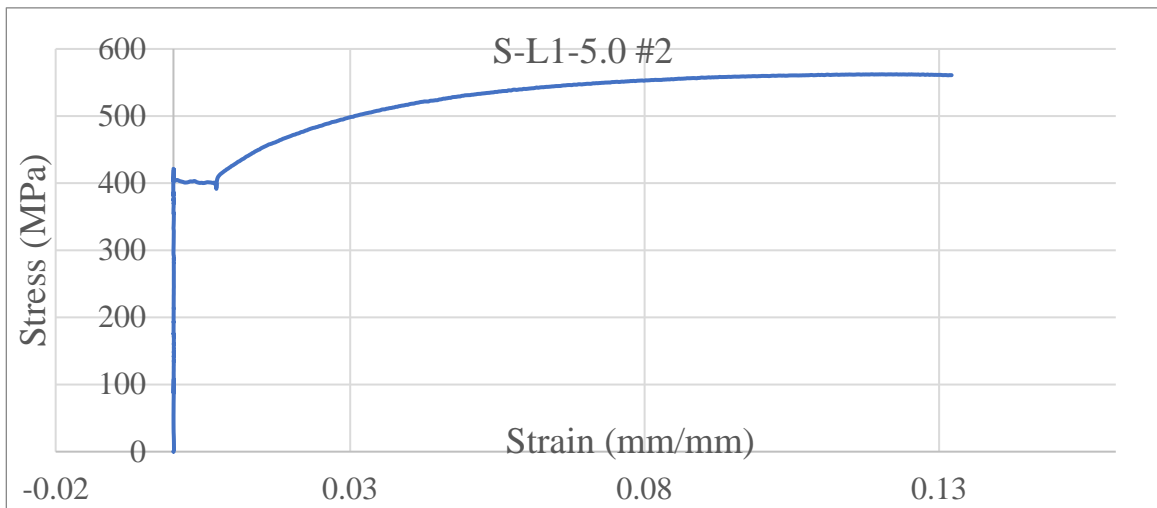


Figure 45 - Stress-Strain Curve for S-L1-5.0

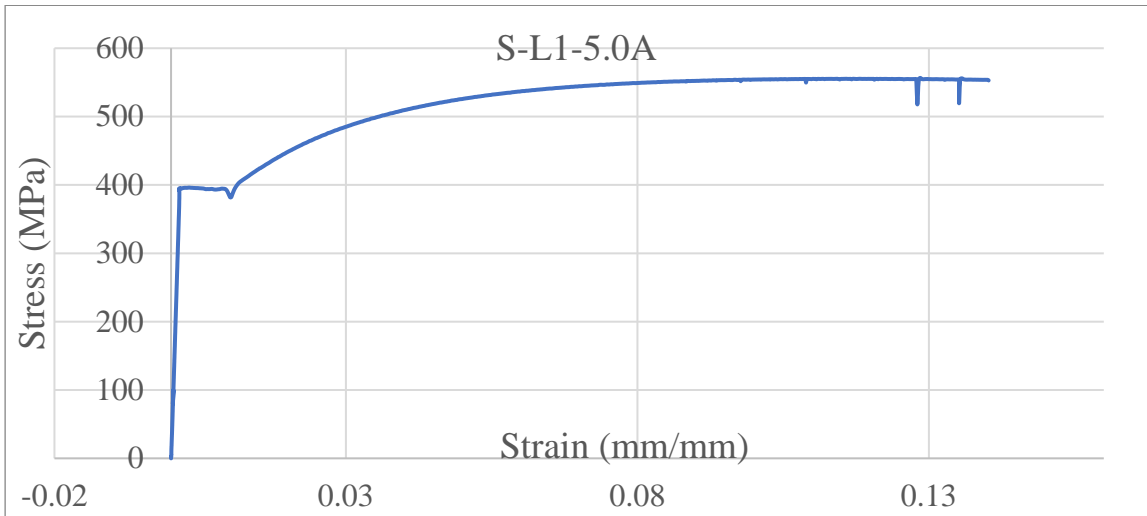


Figure 46 - Stress-Strain Curve for S-L1-5.0A

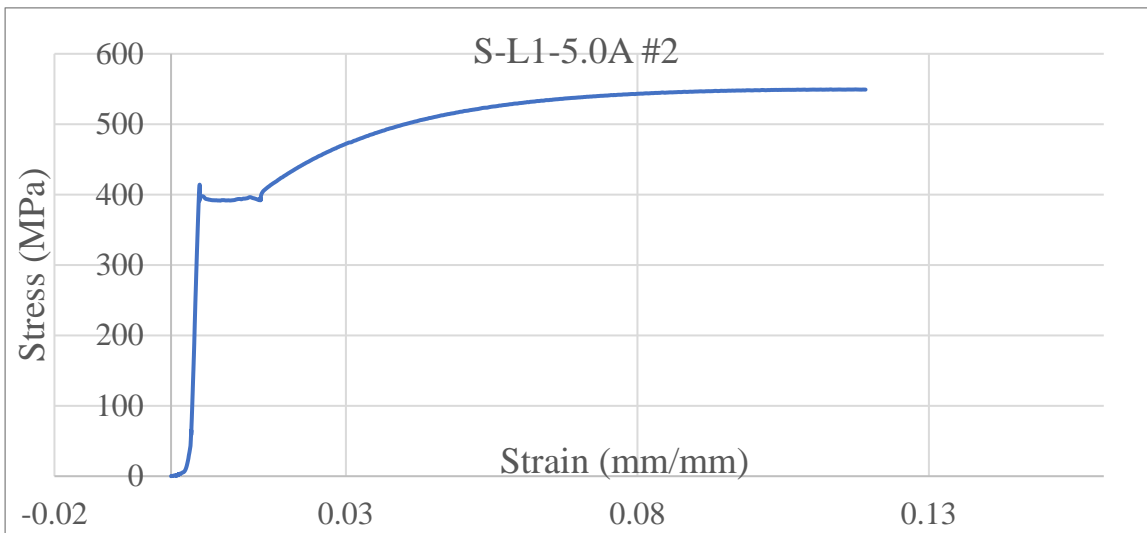


Figure 47 - Stress-Strain Curve for S-L1-5.0A

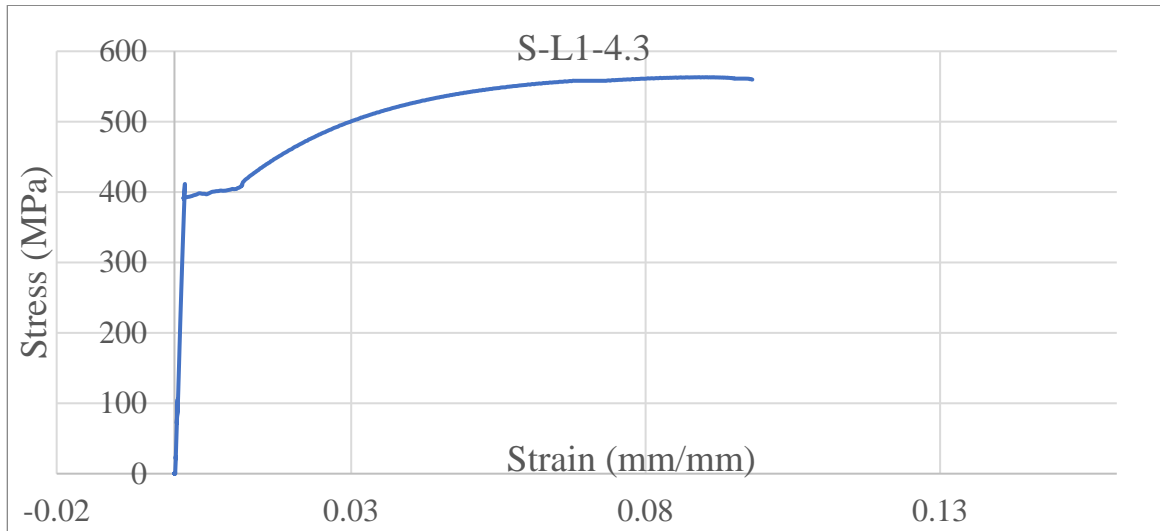


Figure 48 - Stress-Strain Curve for S-L1-4.3

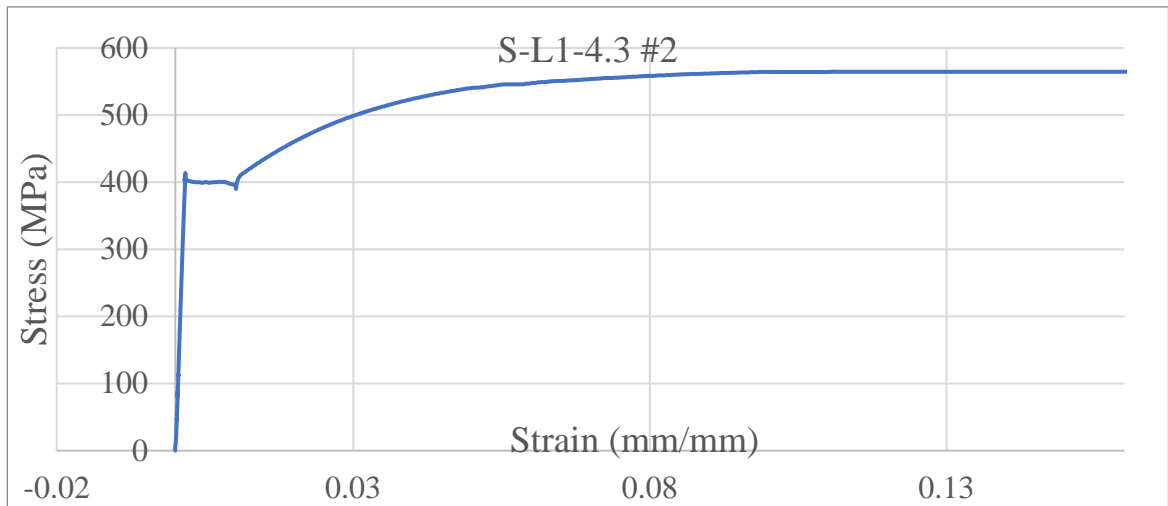


Figure 49 - Stress-Strain Curve for S-L1-4.3

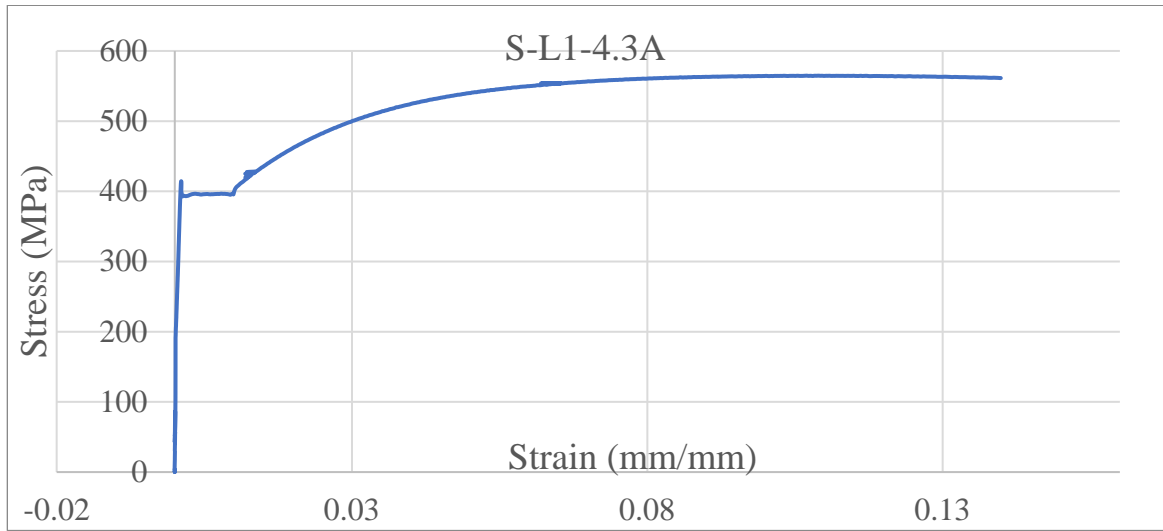


Figure 50 - Stress-Strain Curve for S-L1-4.3A

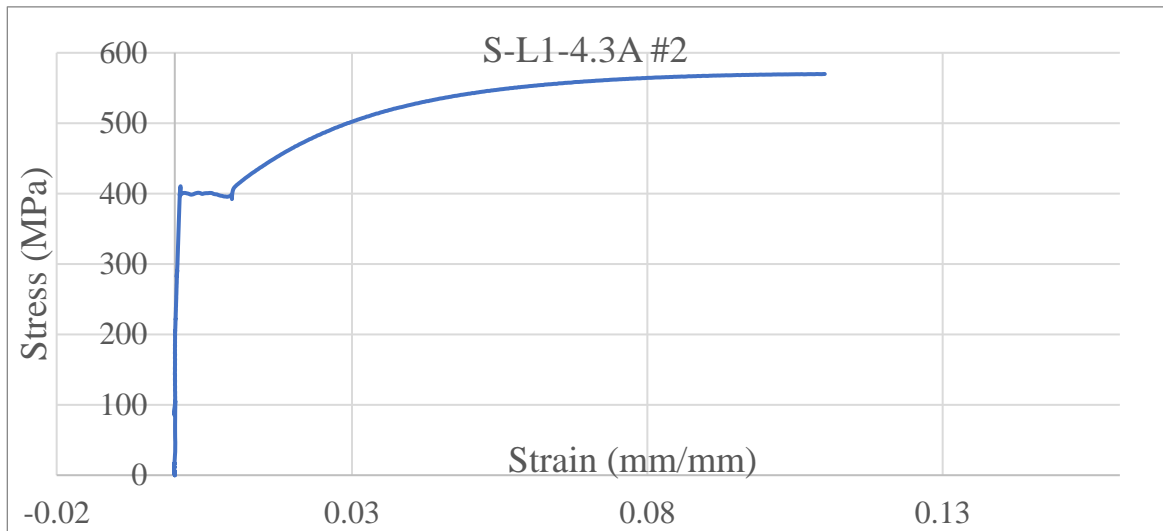


Figure 51 - Stress-Strain Curve for S-L1-4.3A

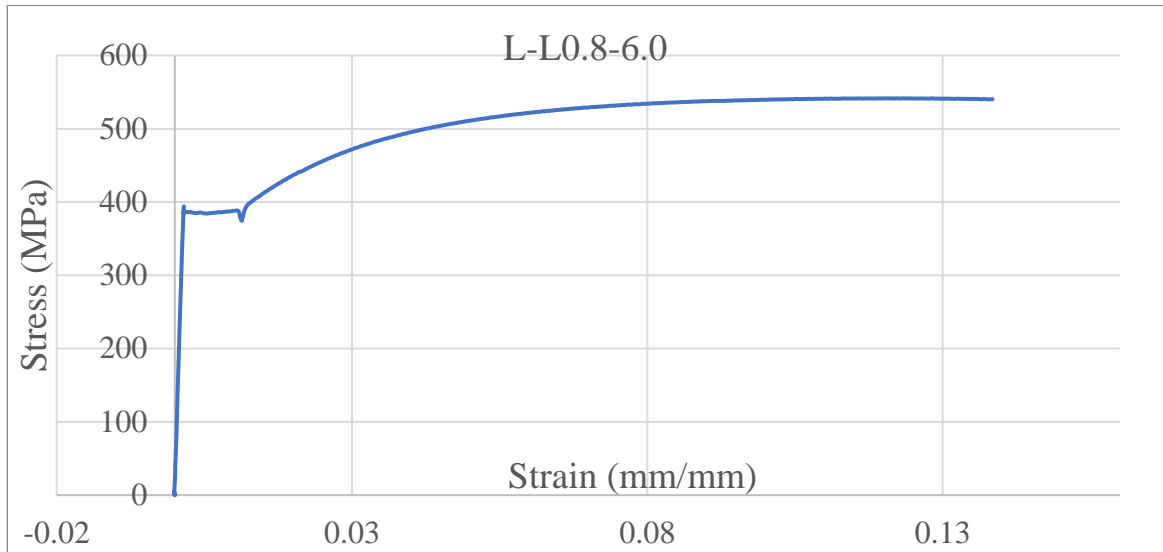


Figure 52 - Stress-Strain Curve for L-L0.8-6.0

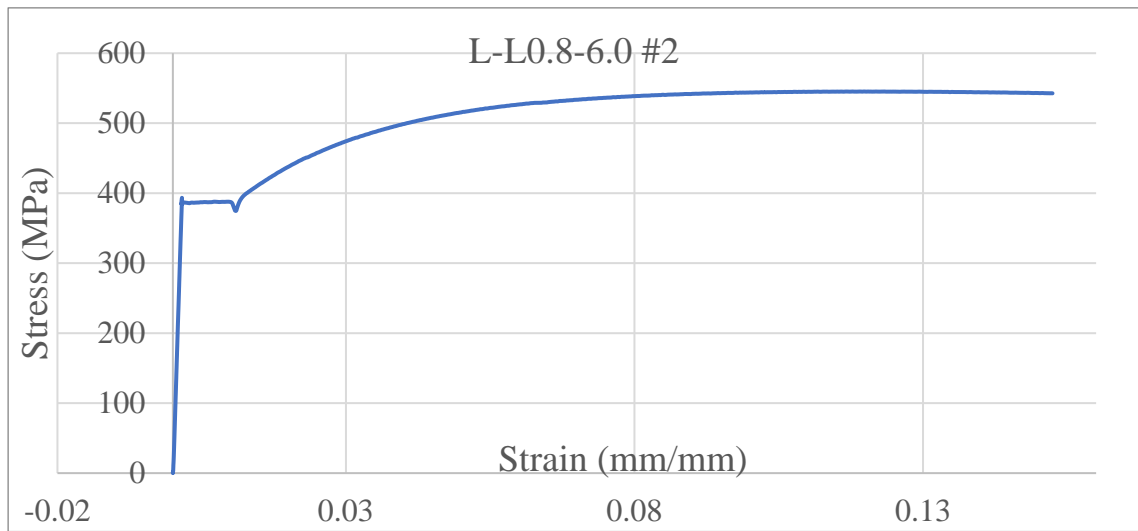


Figure 53 - Stress-Strain Curve for L-L0.8-6.0

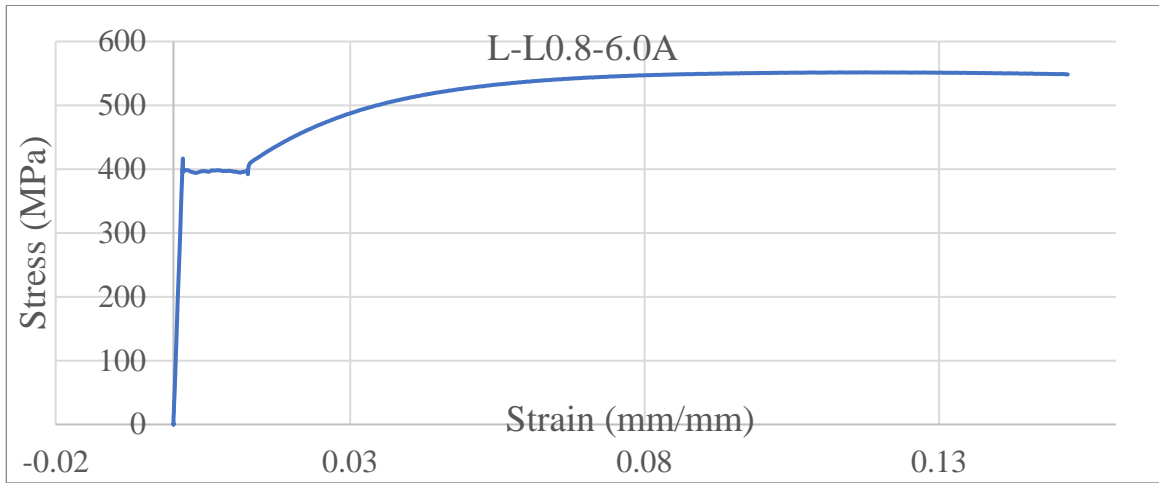


Figure 54 - Stress-Strain Curve for L-L0.8-6.0A

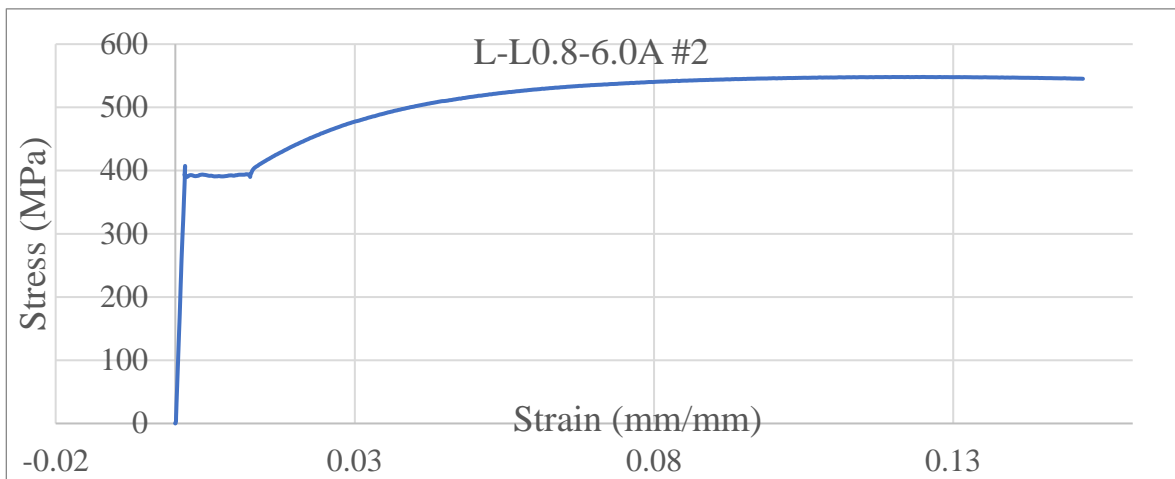


Figure 55 - Stress-Strain Curve for L-L0.8-6.0A

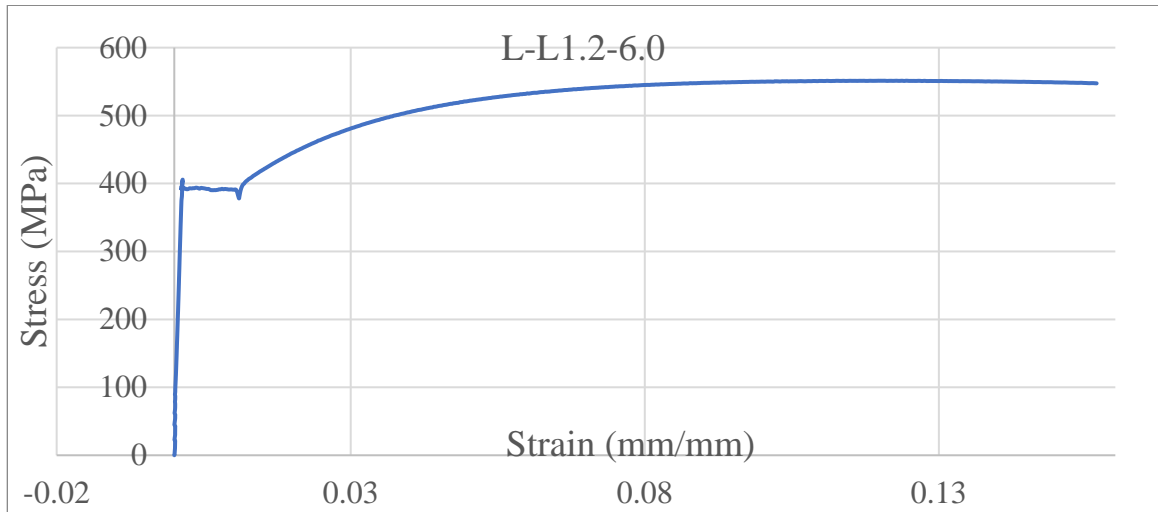


Figure 56 - Stress-Strain Curve for L-L1.2-6.0

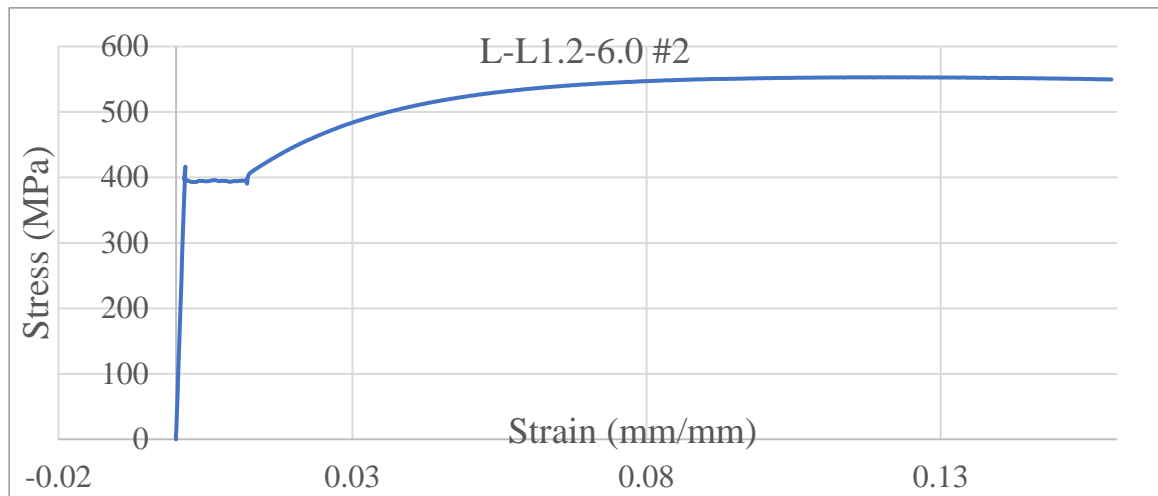


Figure 57 - Stress-Strain Curve for L-L1.2-6.0

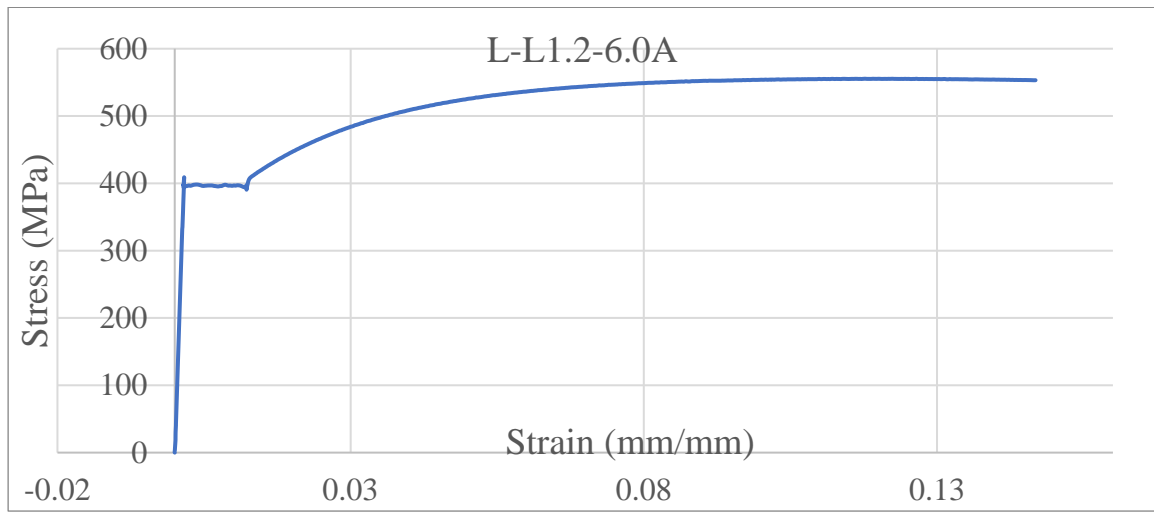


Figure 58 - Stress-Strain Curve for L-L1.2-6.0A

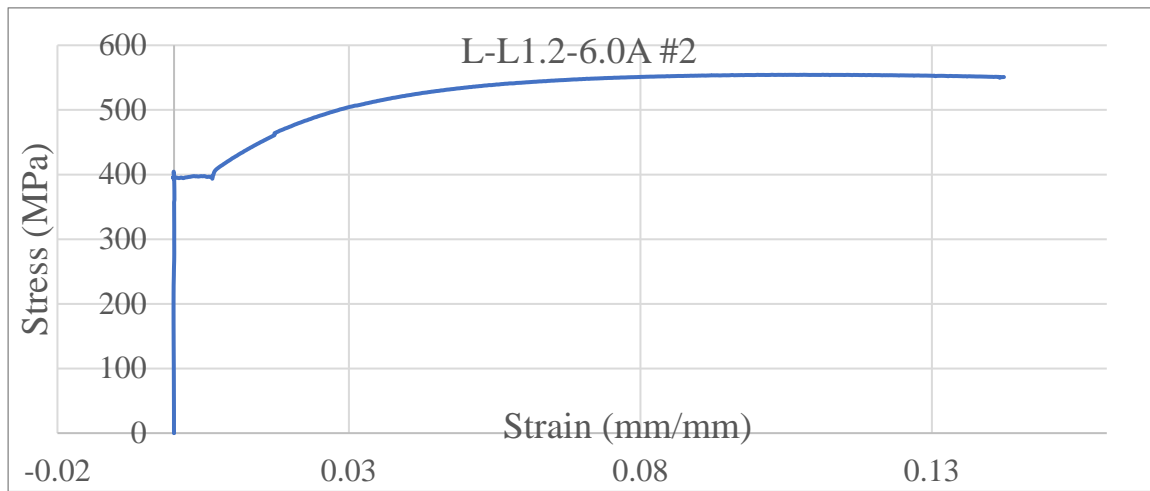


Figure 59 - Stress-Strain Curve for L-L1.2-6.0A

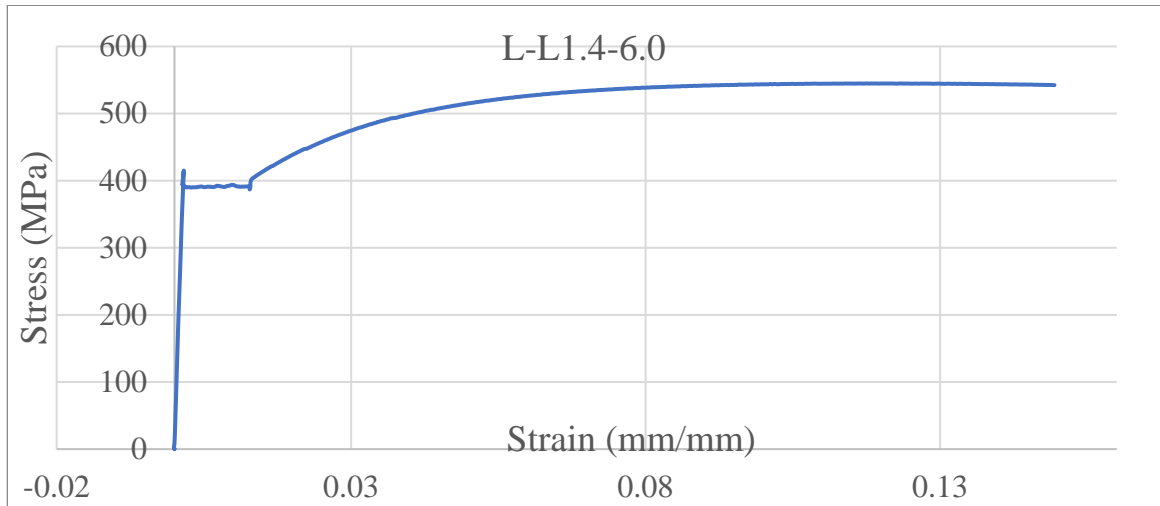


Figure 60 - Stress-Strain Curve for L-L1.4-6.0

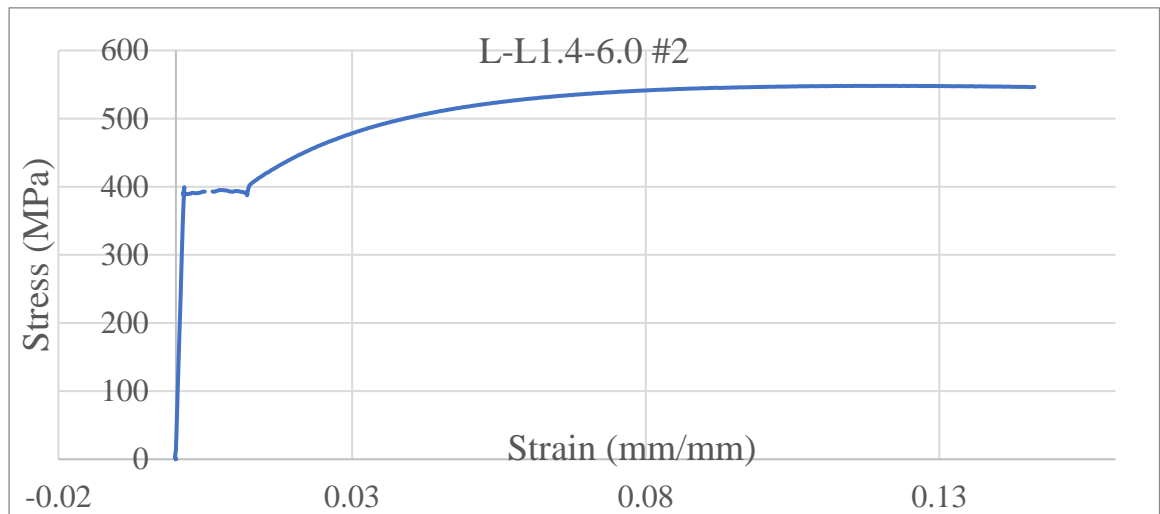


Figure 61 - Stress-Strain Curve for L-L1.4-6.0

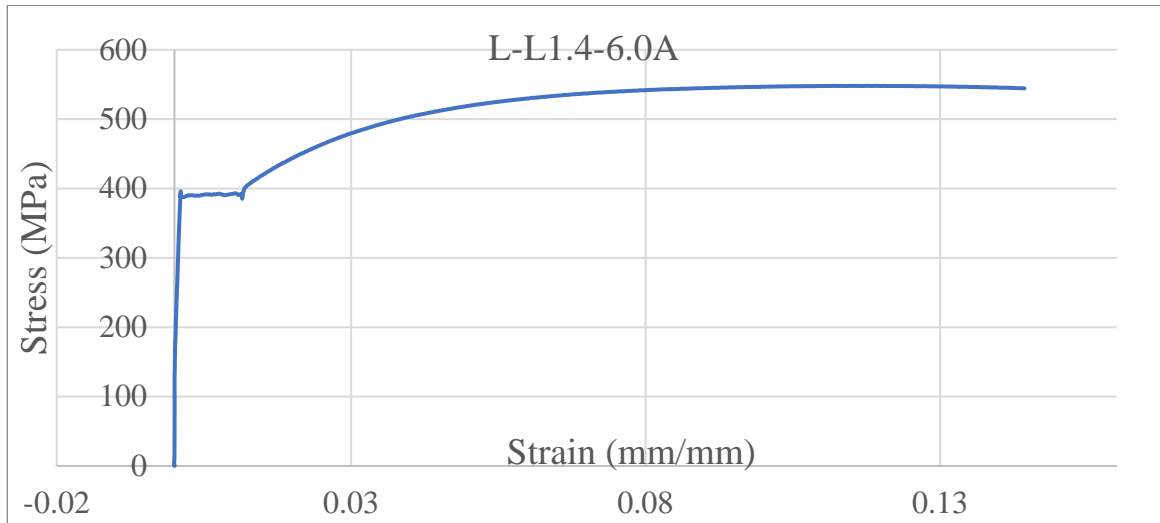


Figure 62 - Stress-Strain Curve for L-L1.4-6.0A

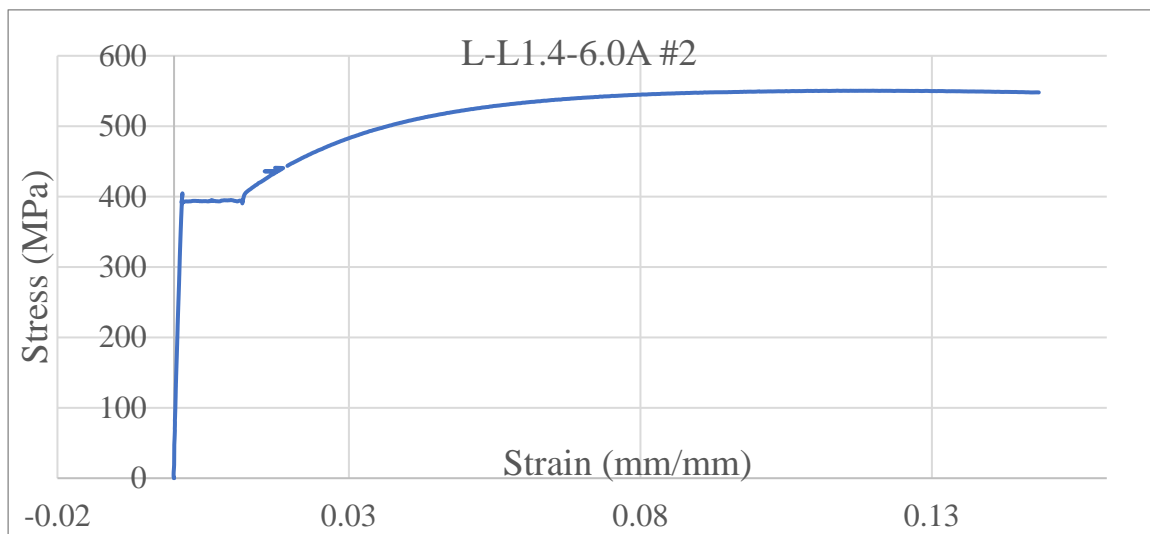


Figure 63 - Stress-Strain Curve for L-L1.4-6.0A

Appendix B – Material Model in ABAQUS

- An example of the steel coupon calibration is shown here

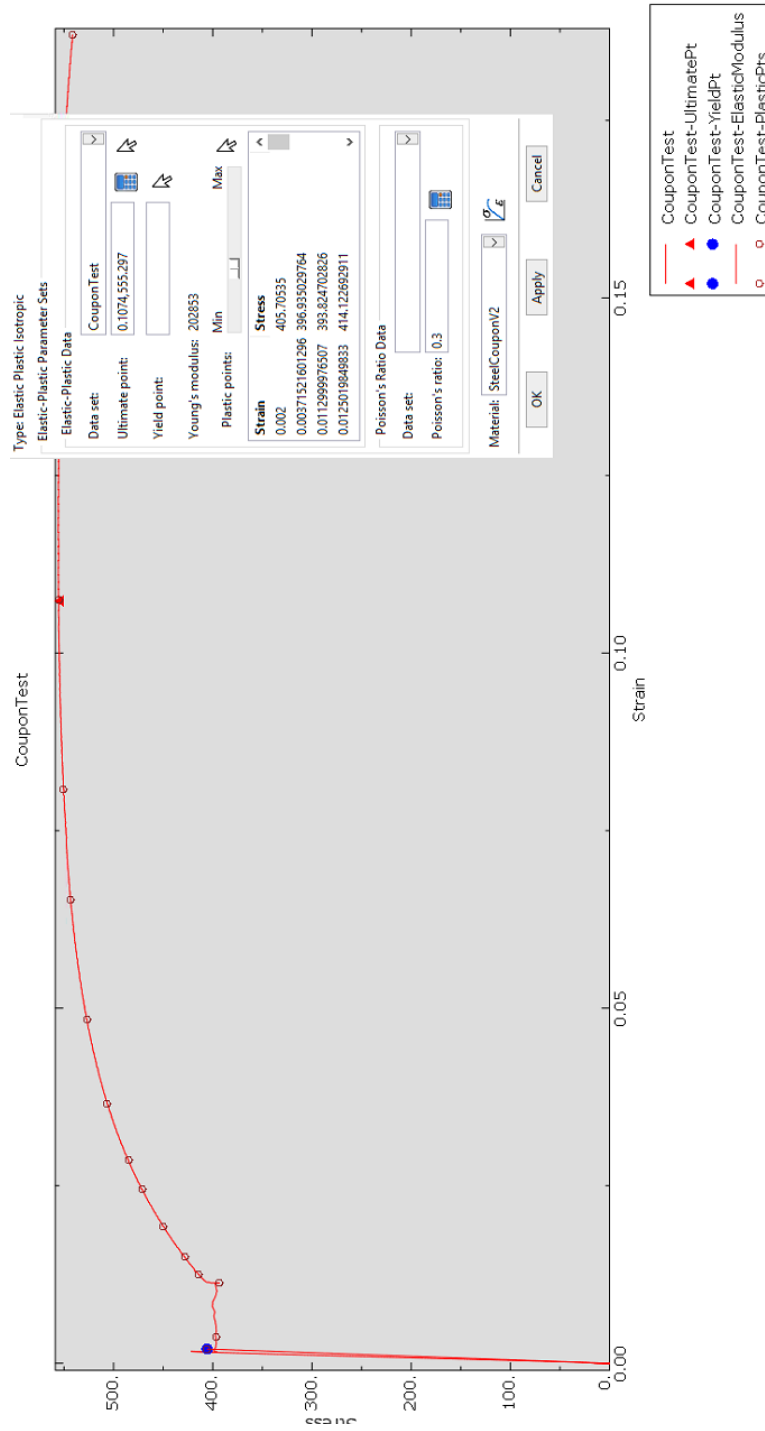


Figure 64 - ABAQUS Material Properties Curve Fitting using Coupon Test Data

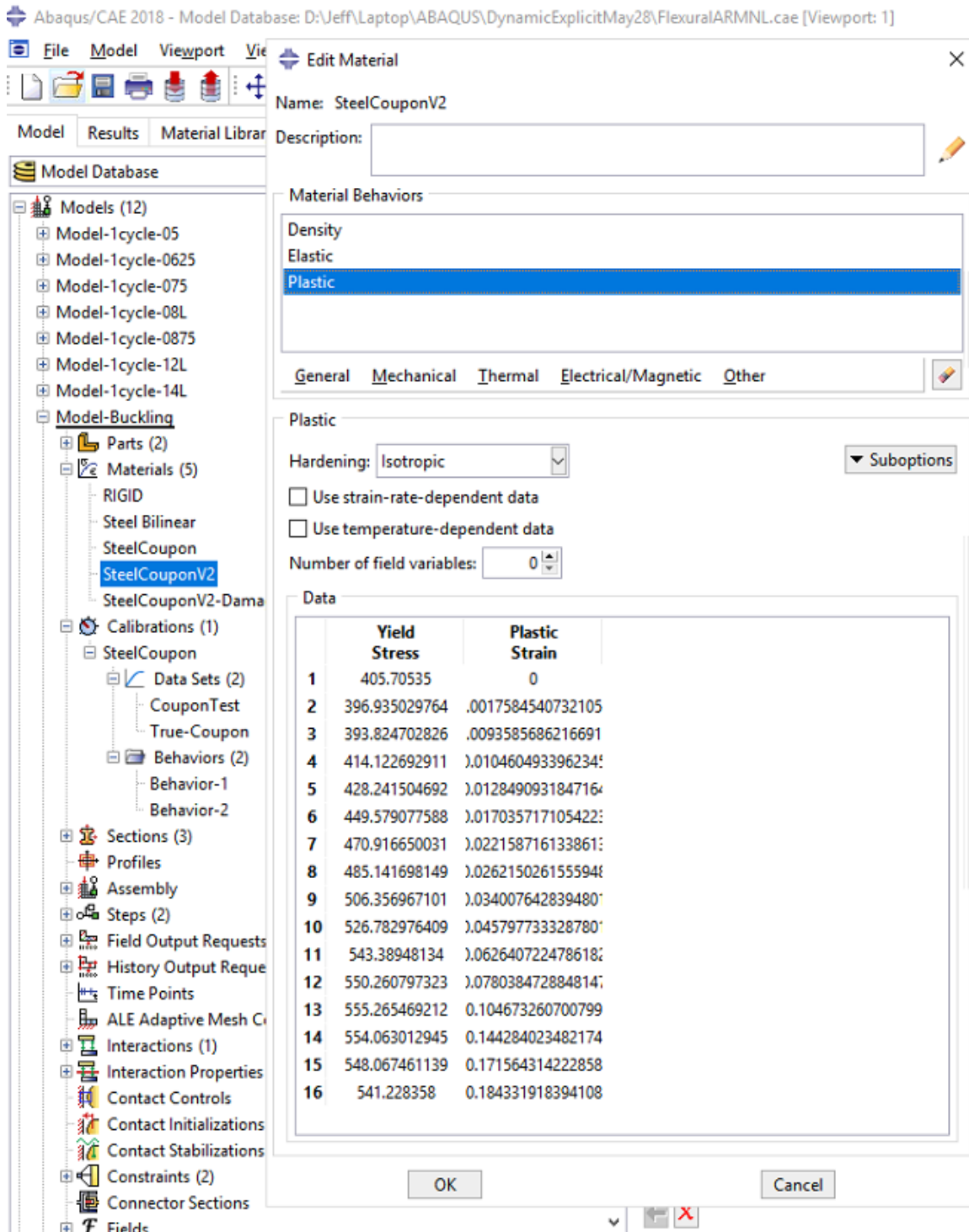


Figure 65- ABAQUS Material Properties Curve Fitting using Coupon Test Data

Appendix C – Reference Wall from Yassin

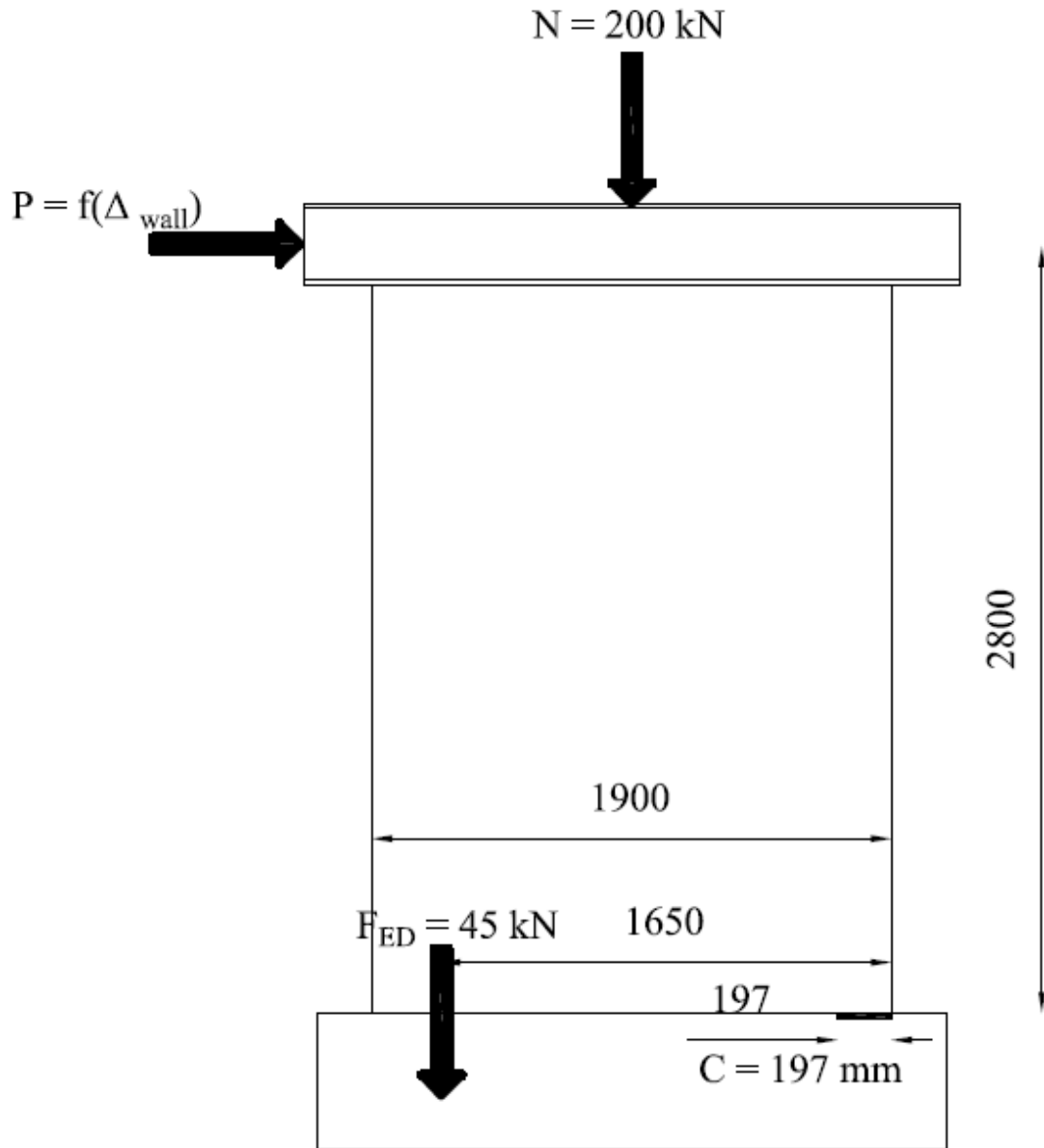
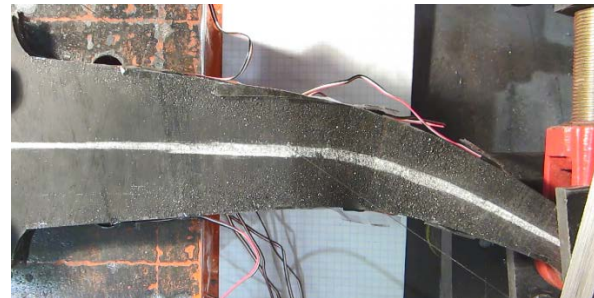


Figure 66 - Sample Calculations for Reference Wall

Appendix D – Damage Sequence of All Specimens



(a) Target Displacement – Top View (47 mm)

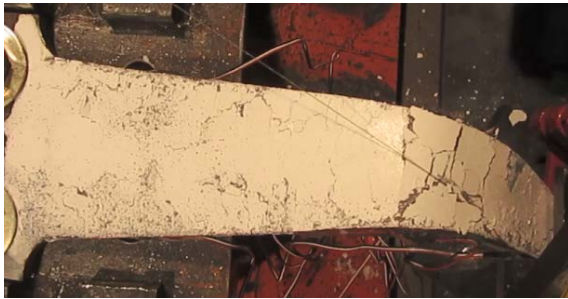


(b) Maximum Displacement - Top View (90 mm)

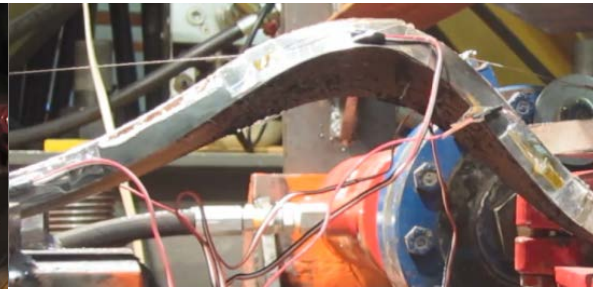


(c) Failure – Top View (2x90 mm)

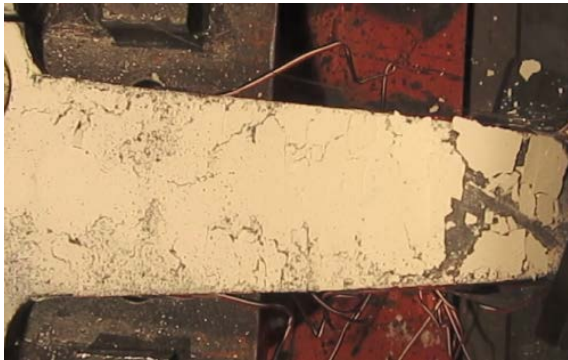
Figure 67 - Test Photos of S-L1-7.5



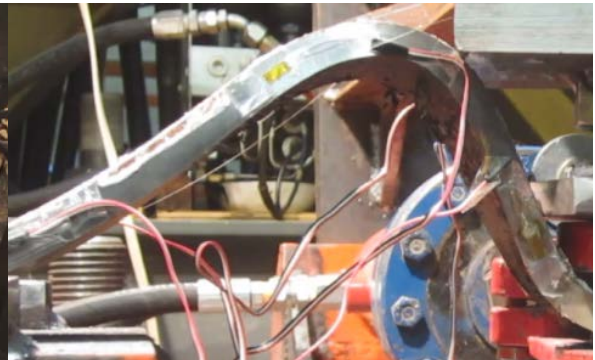
(a) Target Displacement – Top View (47 mm)



(b) Target Displacement - Side View (47 mm)

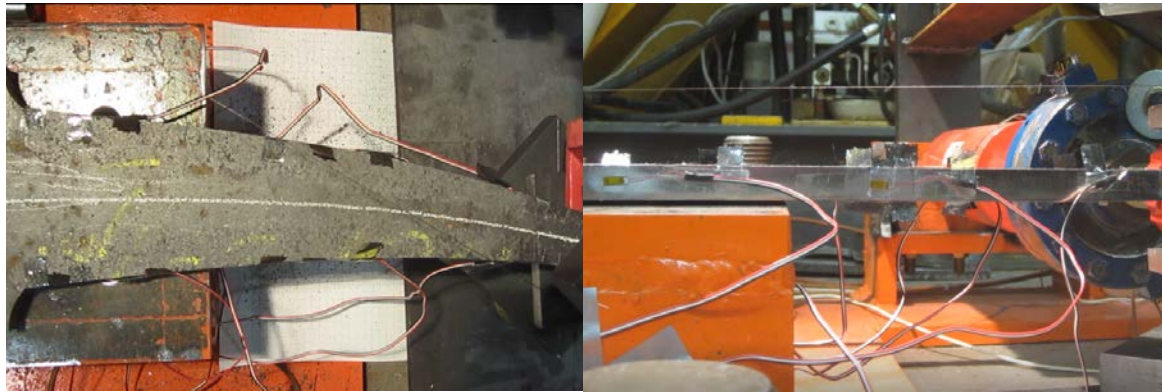


(c) Failure – Top View (47 mm)



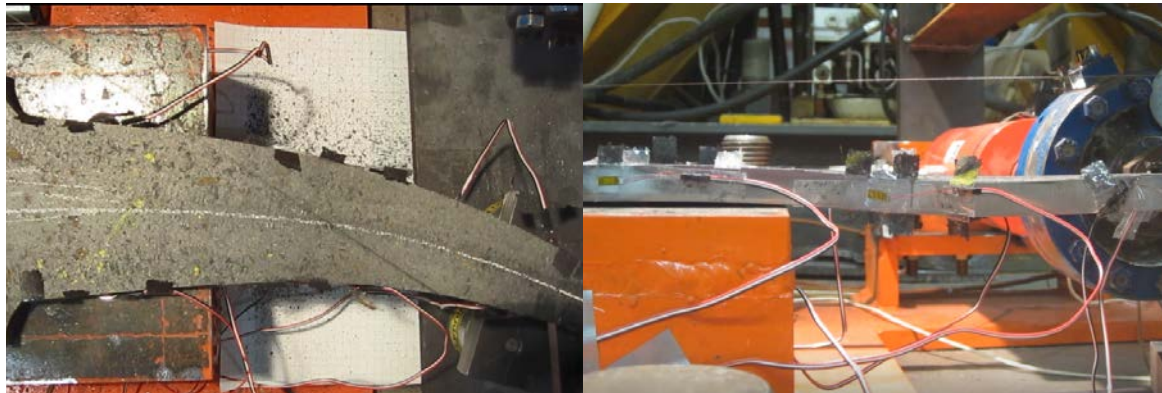
(d) Failure – Side View (47 mm)

Figure 68 - Test Photos of S-L1-7.5A



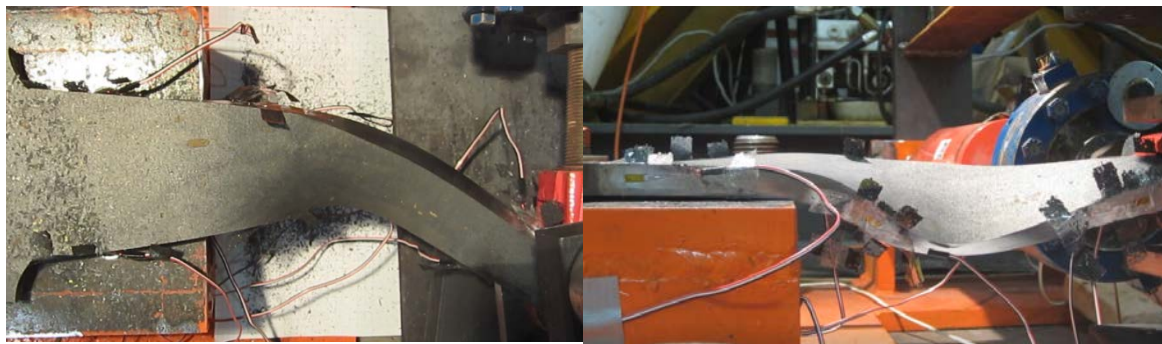
(a) Target Displacement – Top View (47 mm)

(b) Target Displacement – Side View (47 mm)



(c) Max Displacement – Top View (90 mm)

(d) Max Displacement – Side View (90 mm)



(e) Failure – Top View (5x90 mm)

(f) Failure – Side View (5x90 mm)

Figure 69 - Test Photos of S-L1-6.0

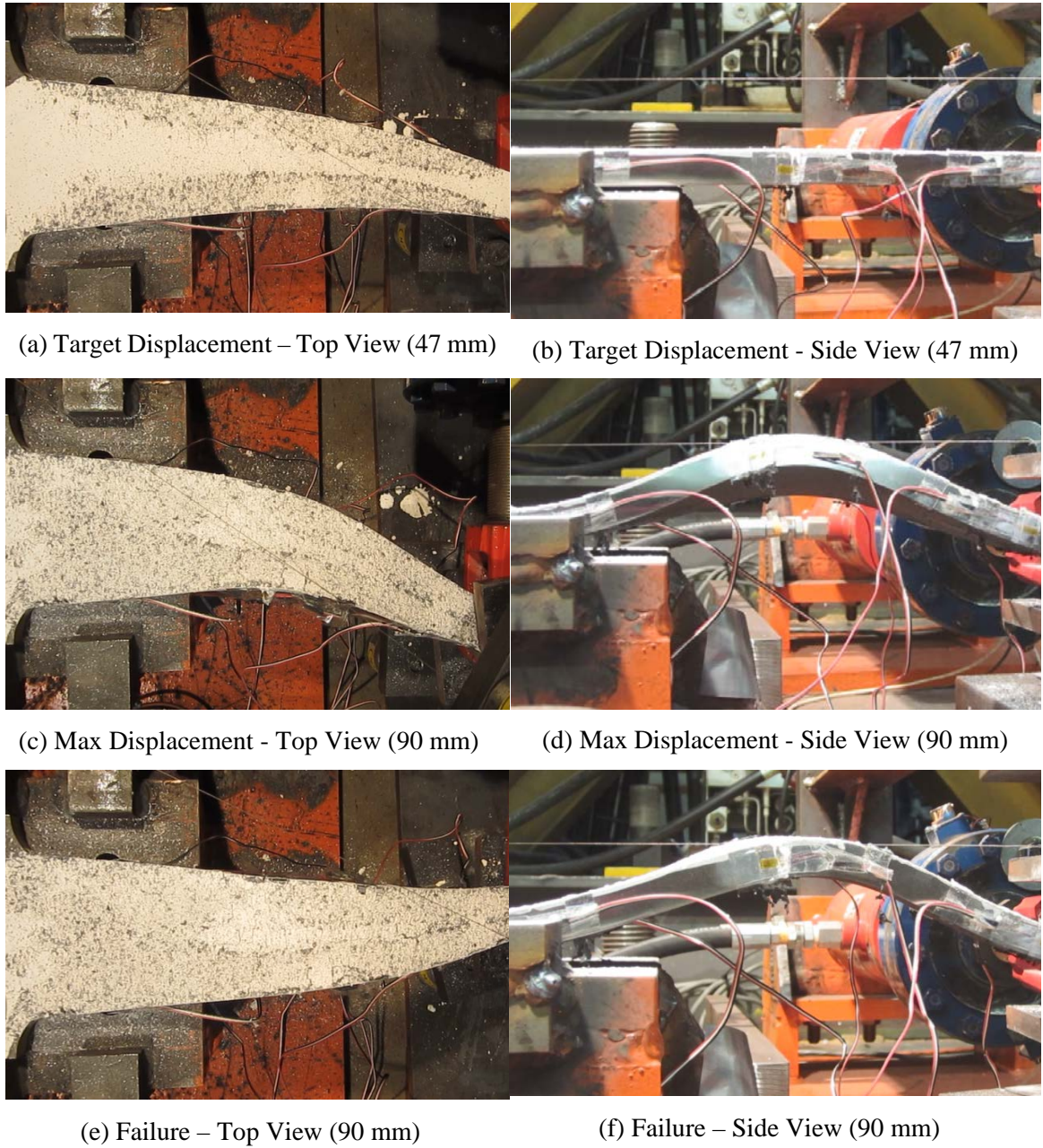


Figure 70 - Test Photos of S-L1-6.0A

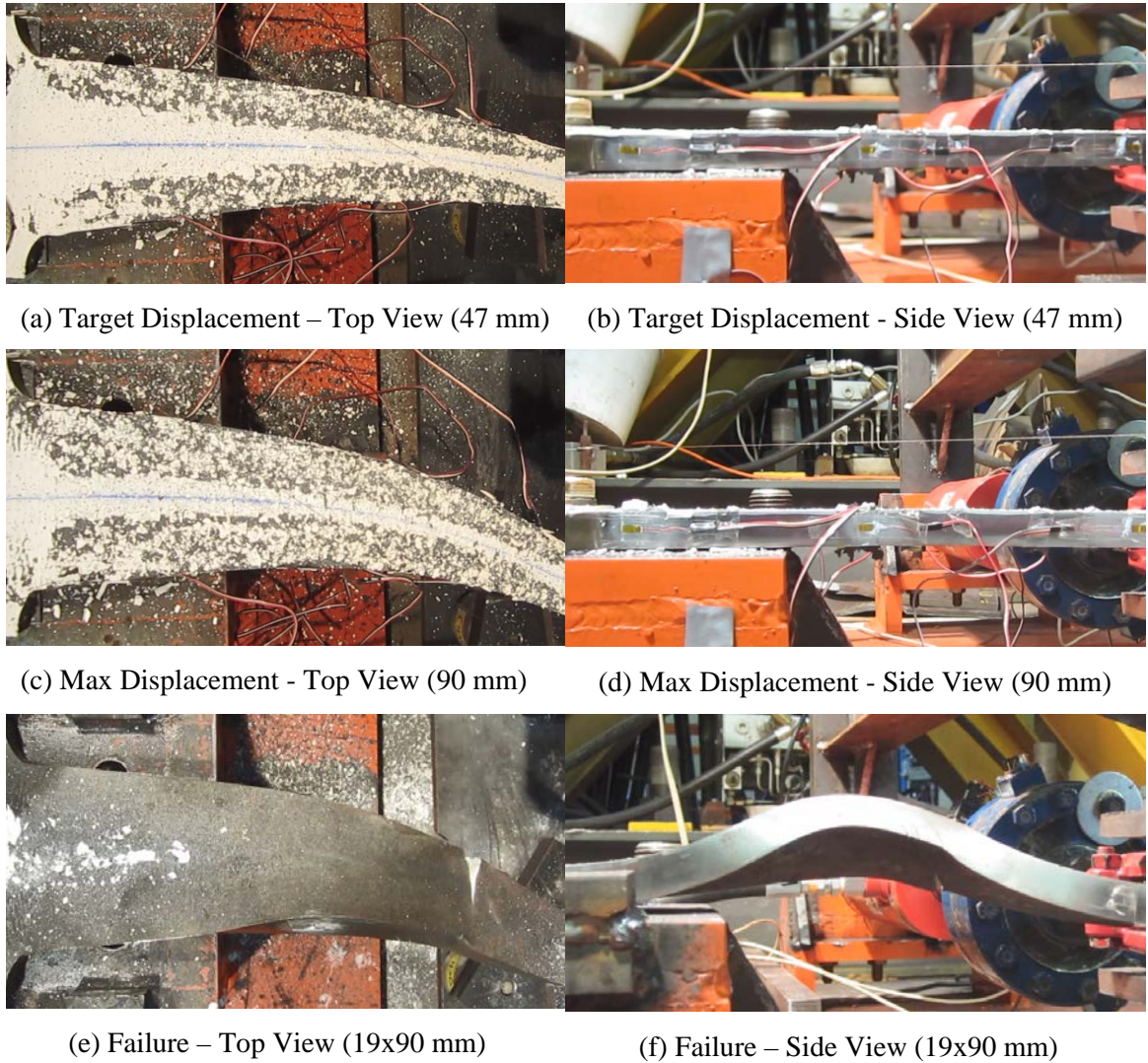
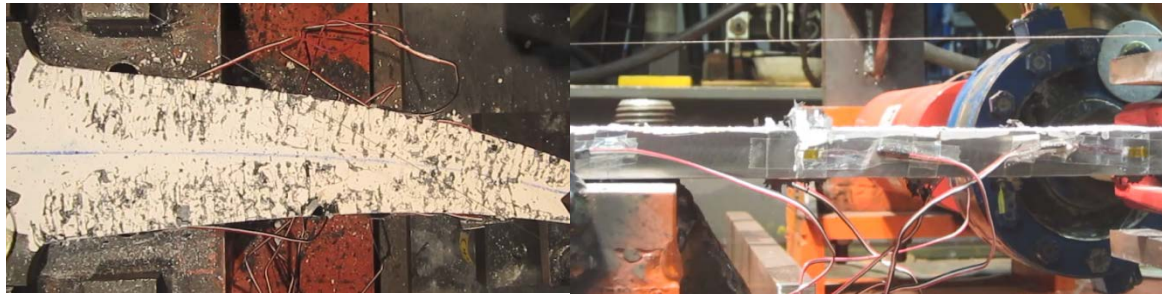
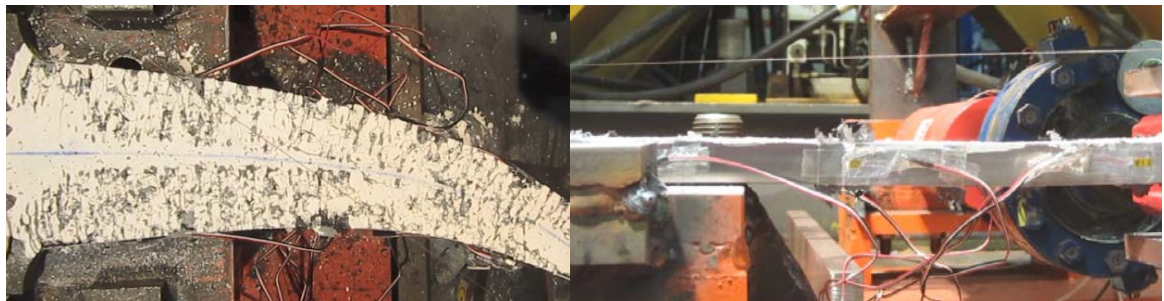


Figure 71 - Test Photos of S-L1-5



(a) Target Displacement – Top View (47 mm)

(b) Target Displacement - Side View (47 mm)



(c) Max Displacement - Top View (90 mm)

(d) Max Displacement - Side View (90 mm)



(e) Failure – Top View (5x90 mm)

(f) Failure – Side View (5x90 mm)

Figure 72 - Test Photos of S-L1-5A

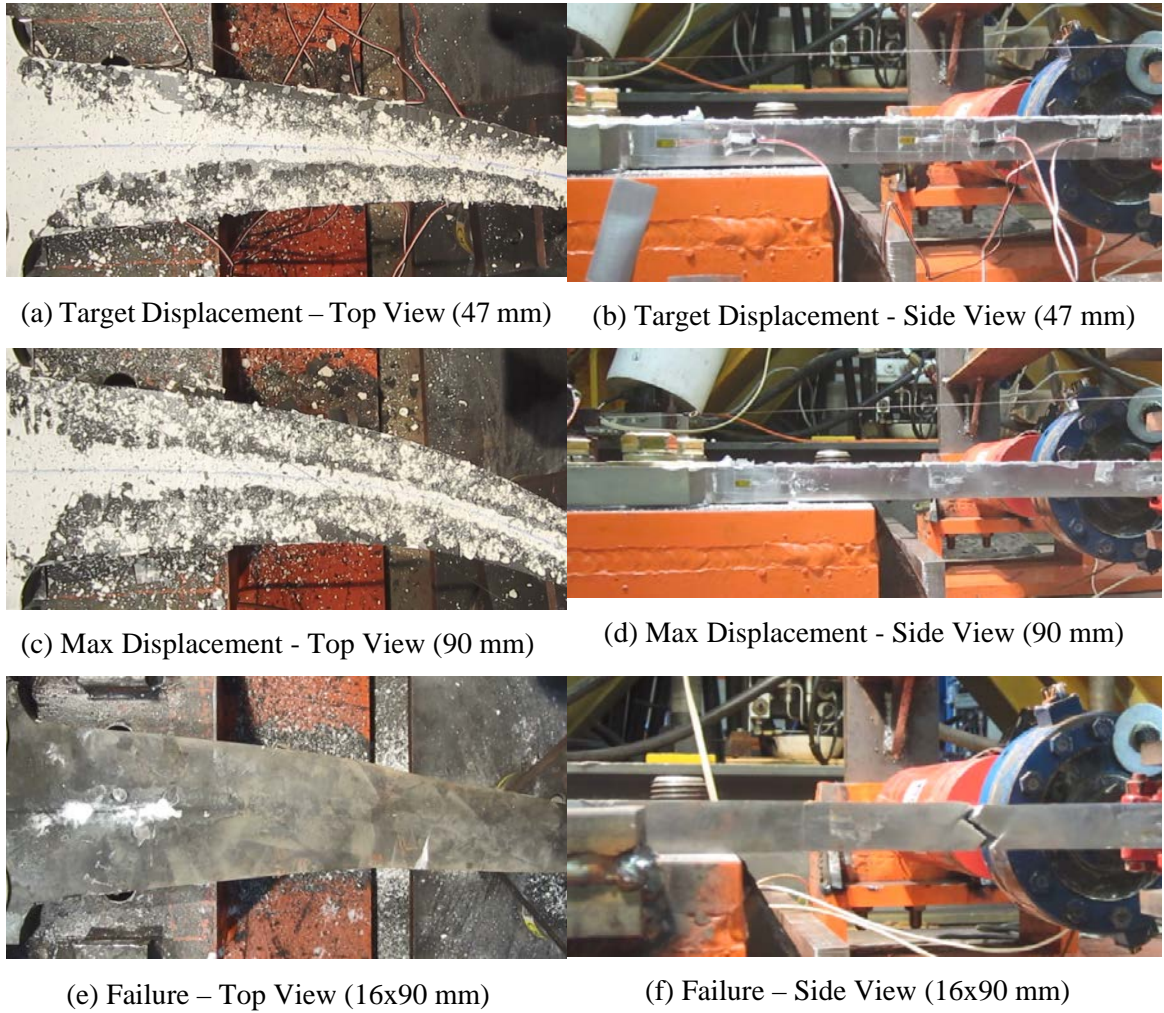


Figure 73 - Test Photos of S-L1-4.3

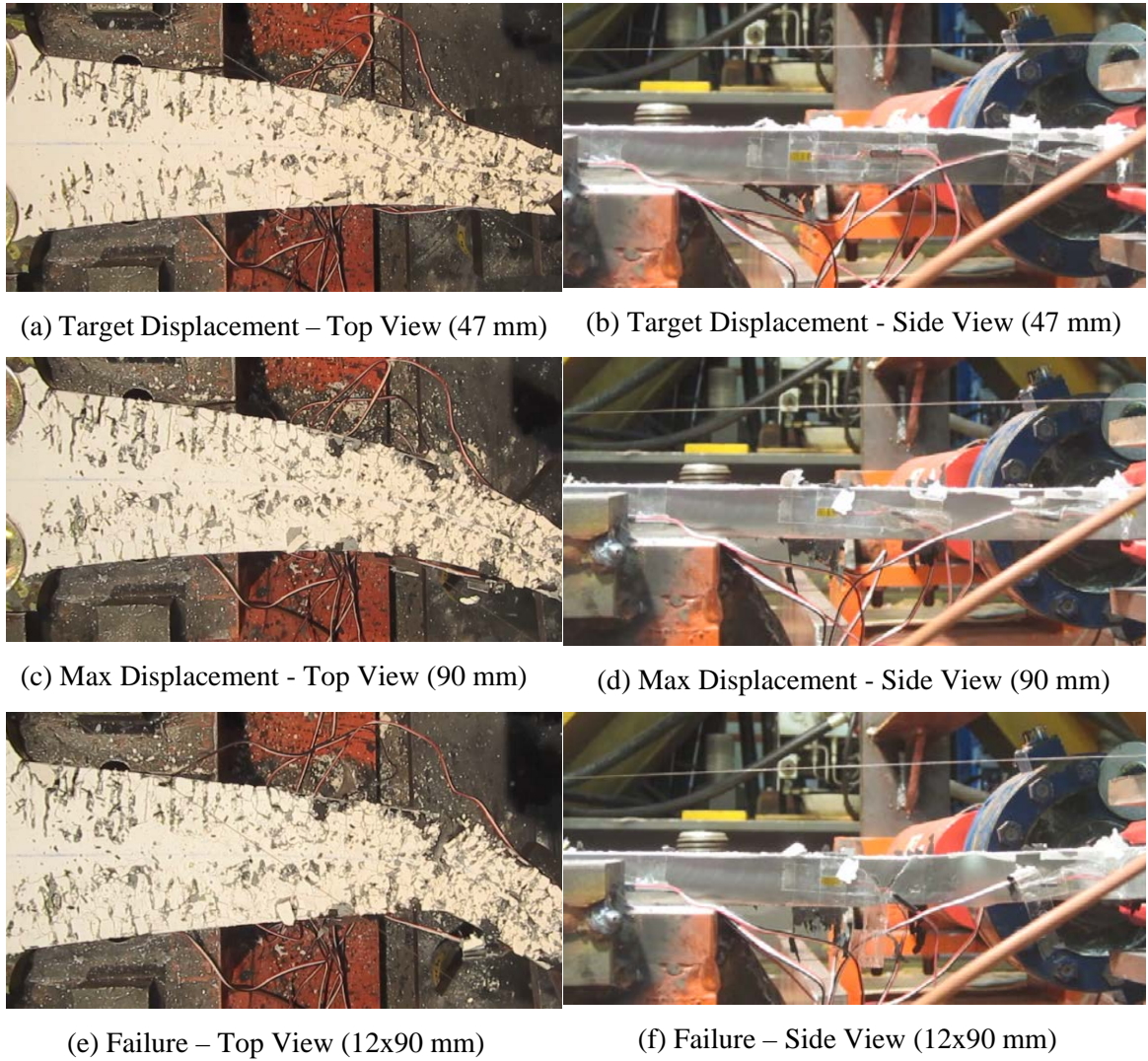


Figure 74 - Test Photos of S-L1-4.3A

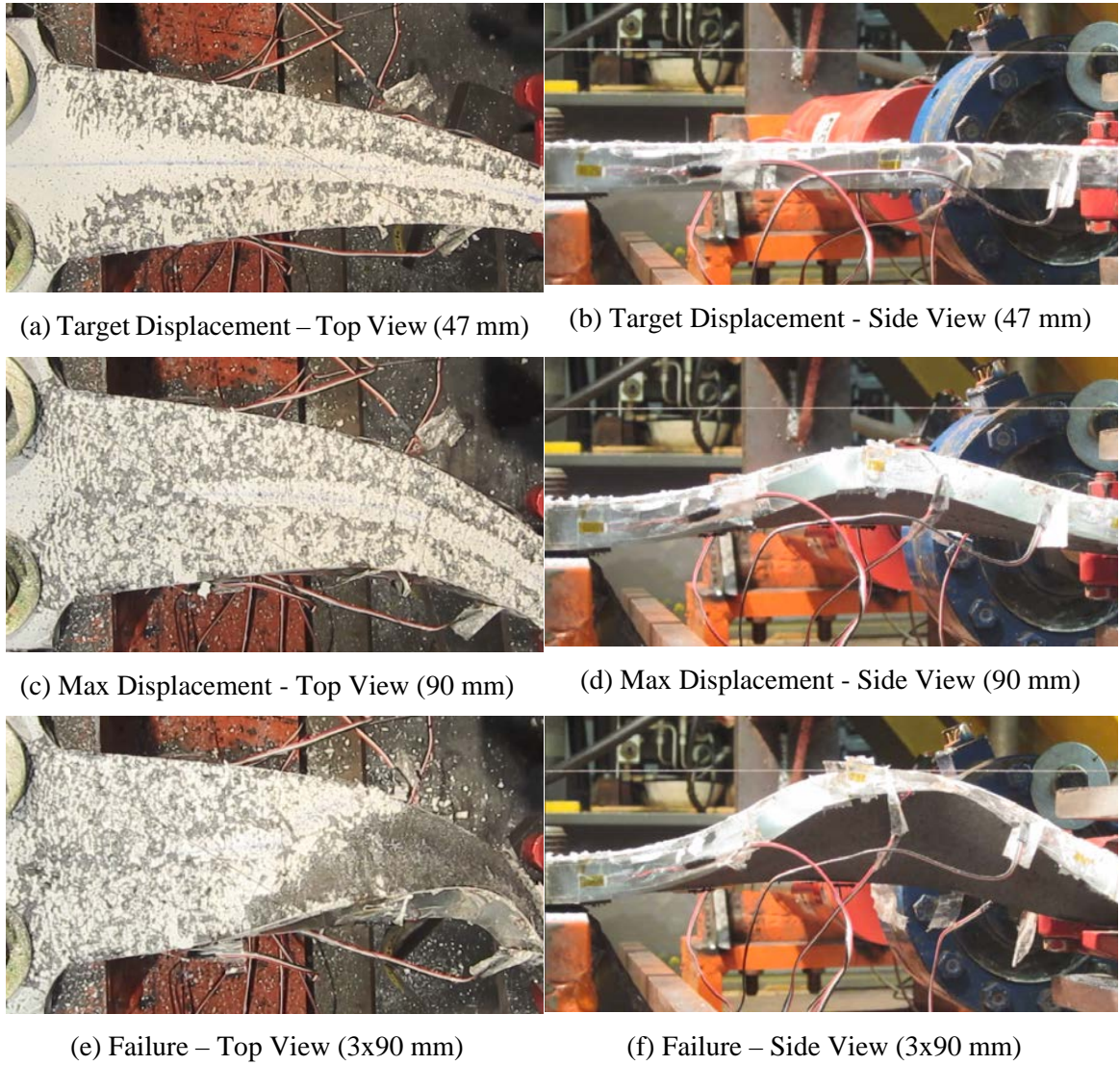


Figure 75 - Test Photos of L-L0.8-6.0

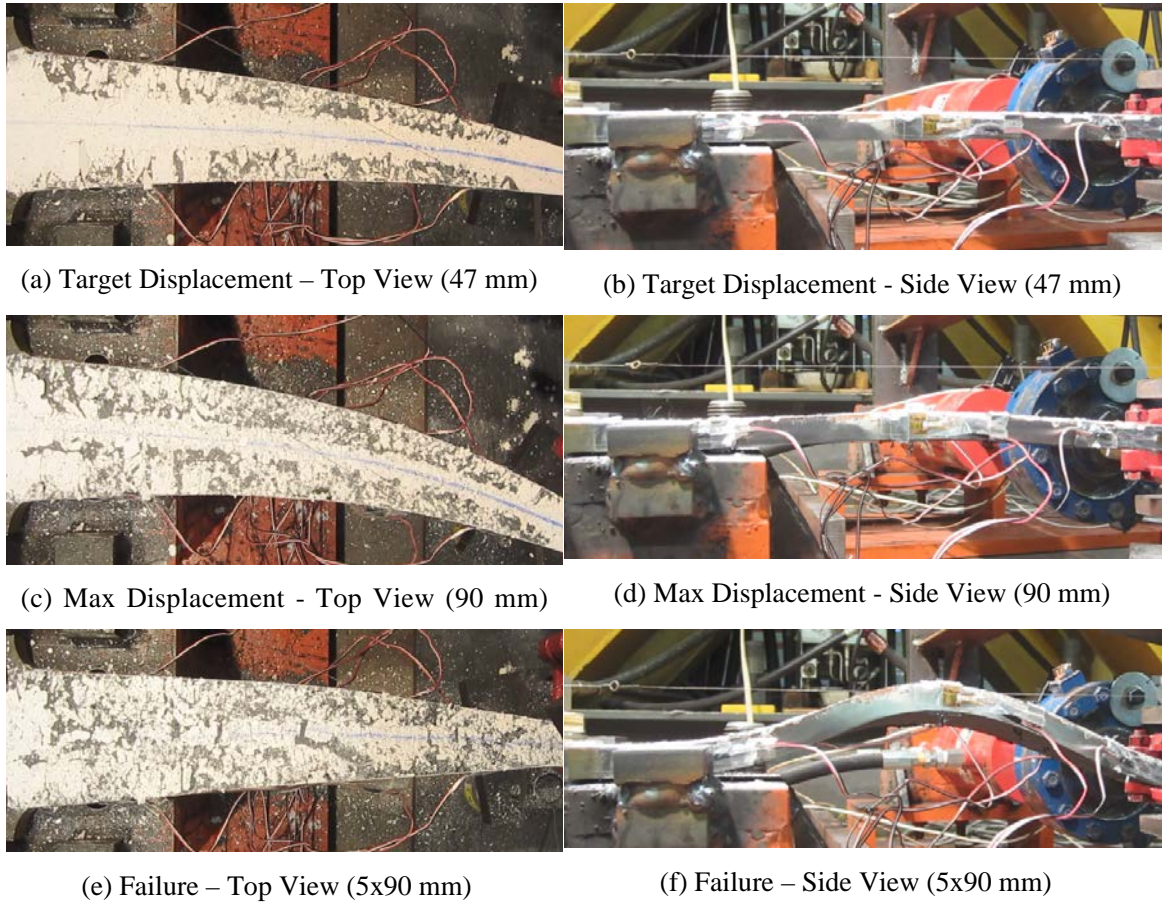


Figure 76 - Test Photos of L-L1.2-6.0

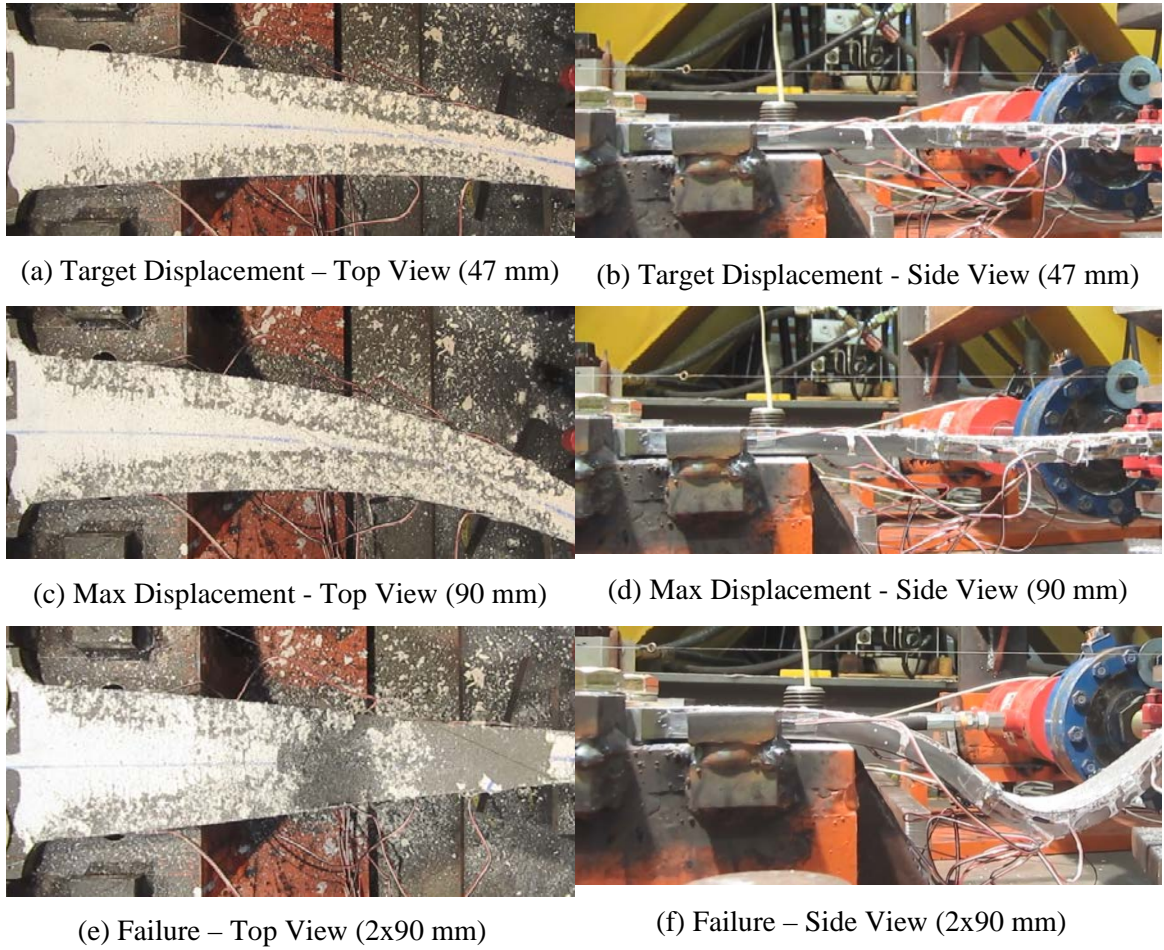


Figure 77 - Test Photos of L-L1.2-6.0A

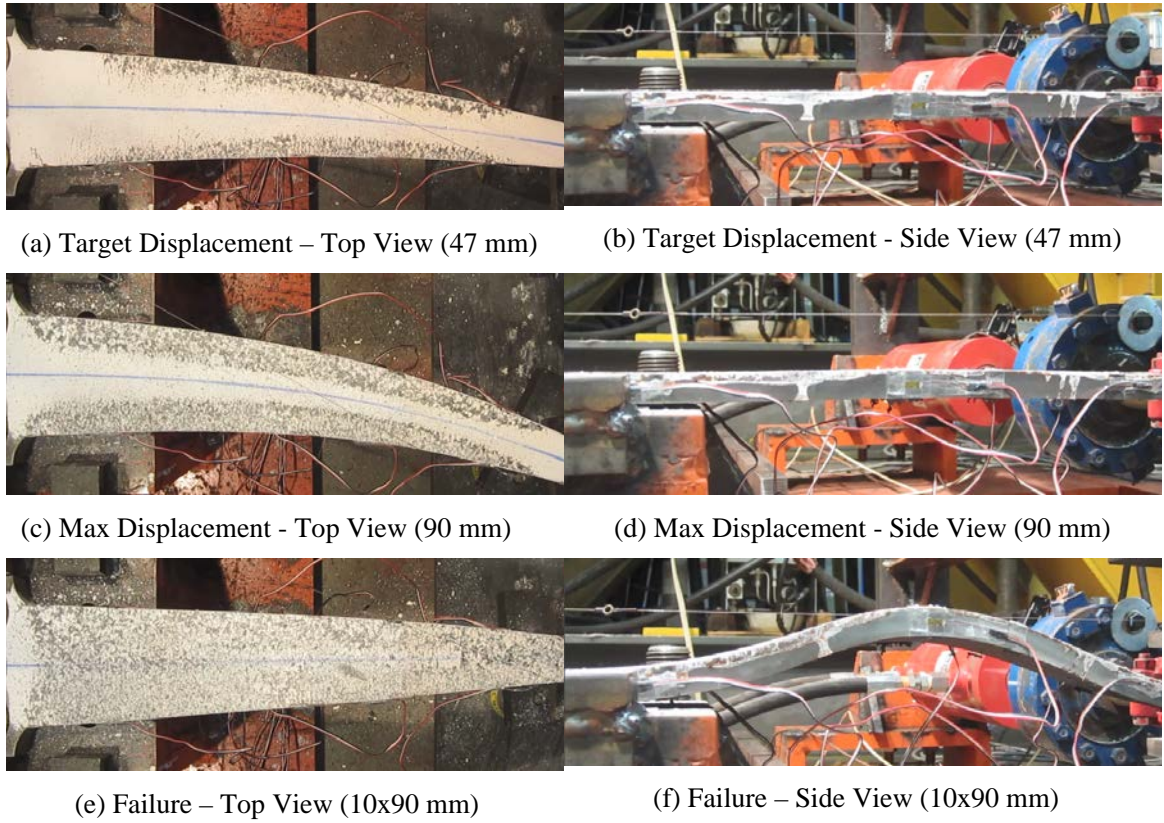


Figure 78 - Test Photos of L-L1.4-6.0

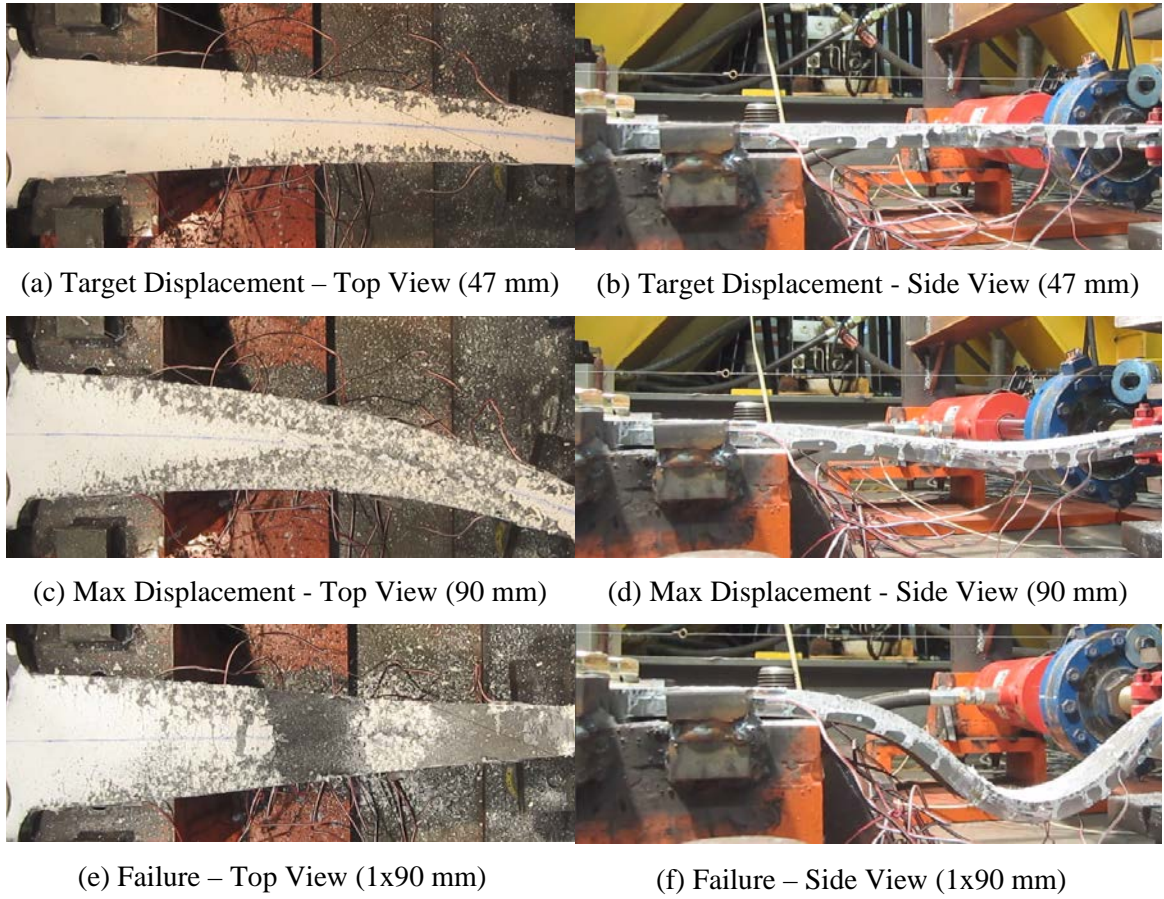


Figure 79 - Test Photos of L-L1.4-6.0A

Appendix E – Strain Gauge Data

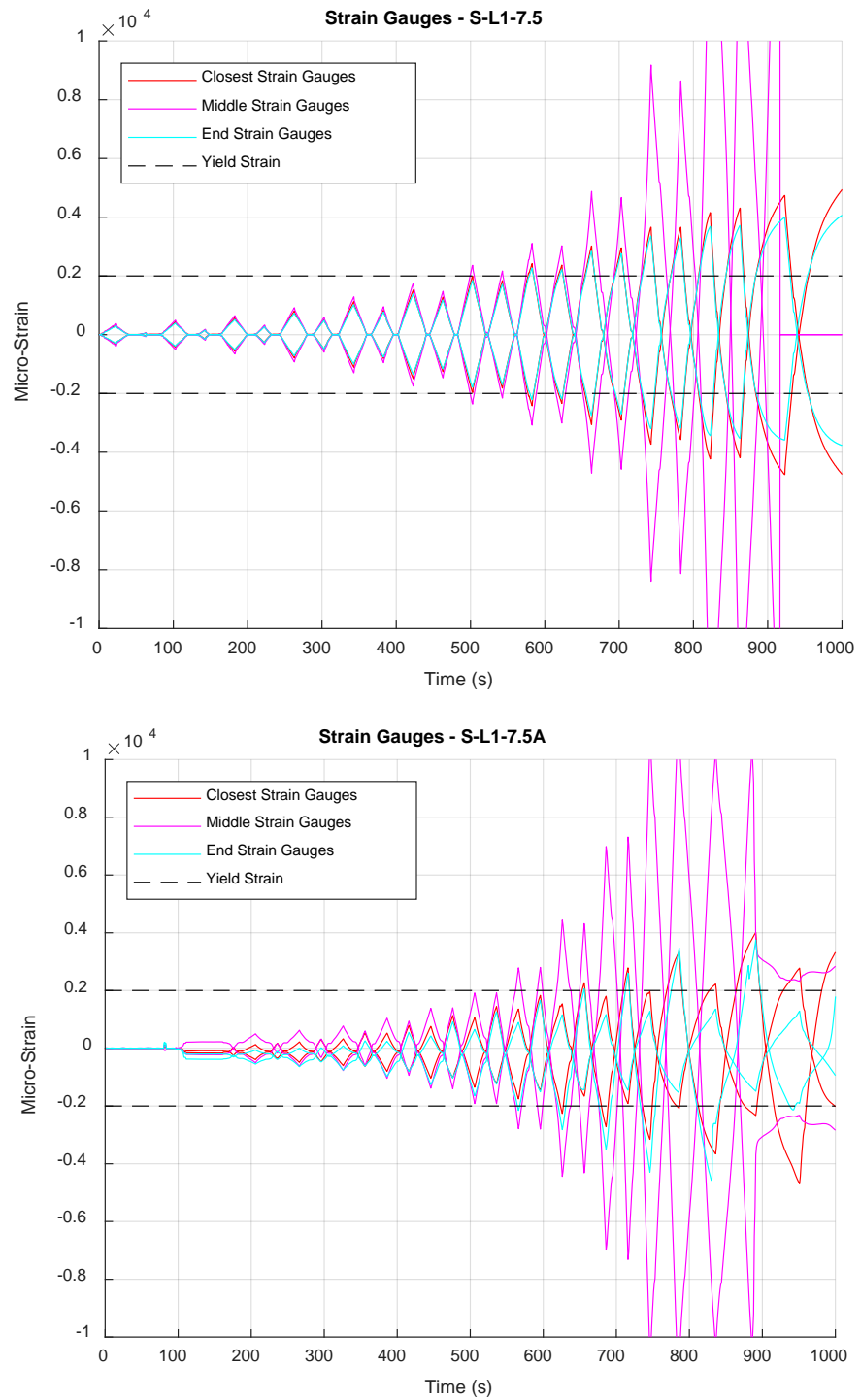


Figure 80 - SG Data for S-L1-7.5 and S-L1-7.5A

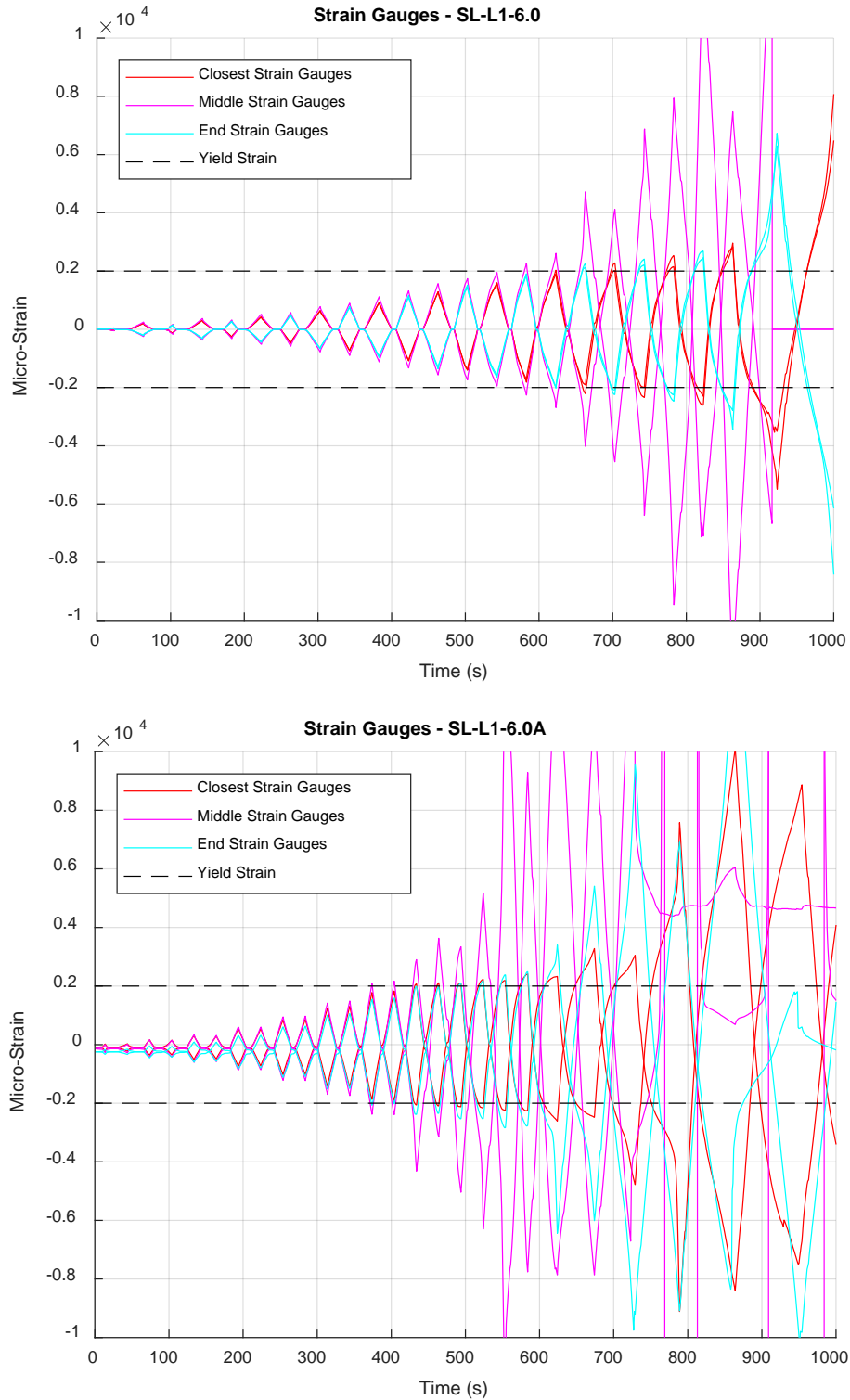


Figure 81 - SG Data for SL-L1-6.0 and SL-L1-6.0A

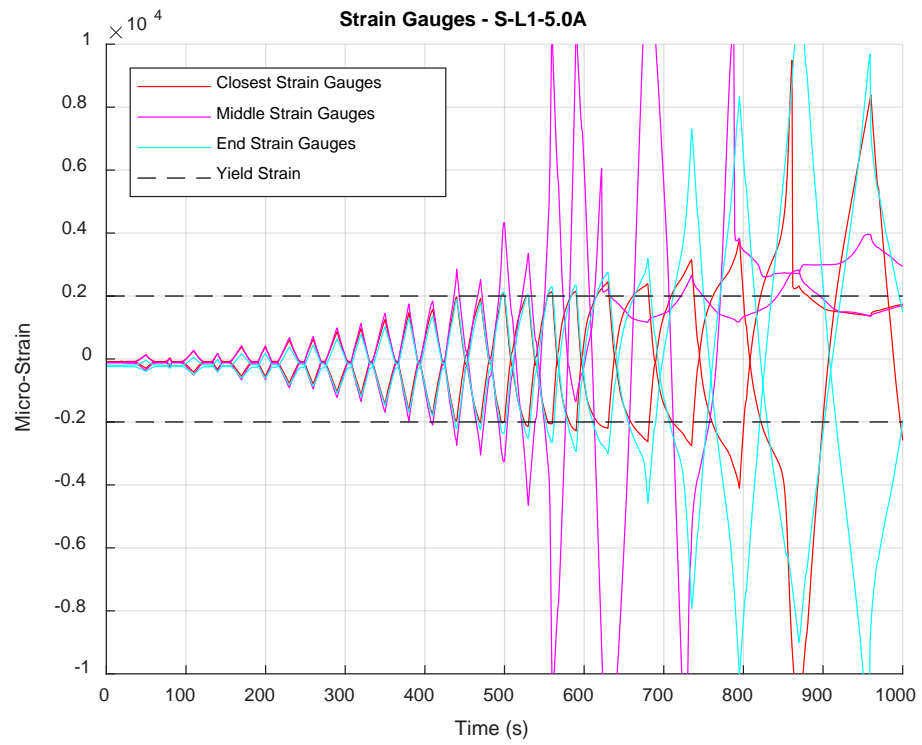
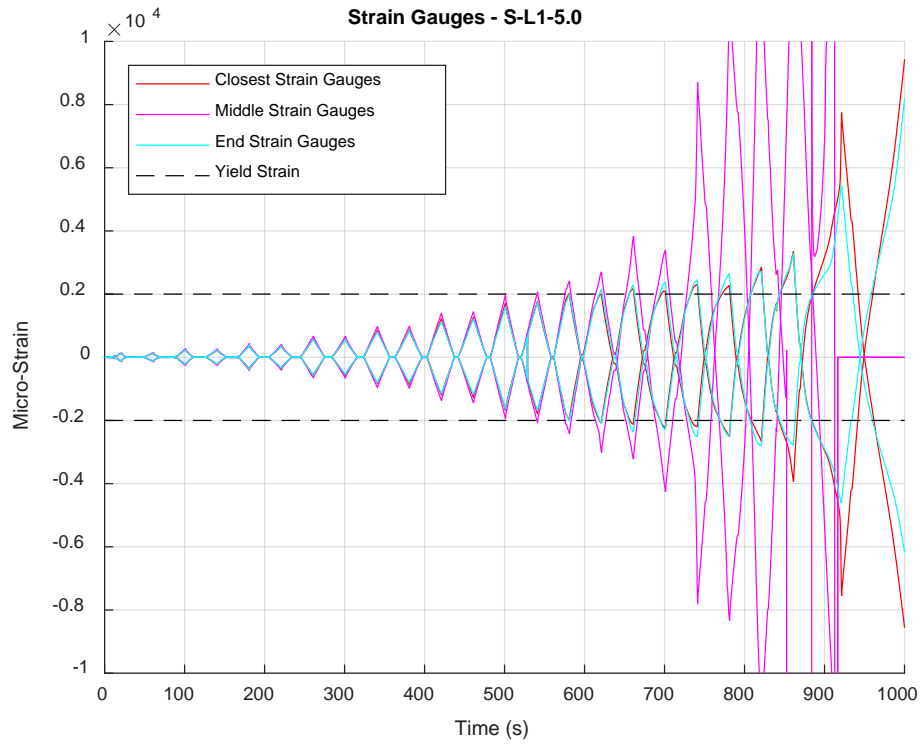


Figure 82 - SG Data for S-L1-5.0 and S-L1-5.0A

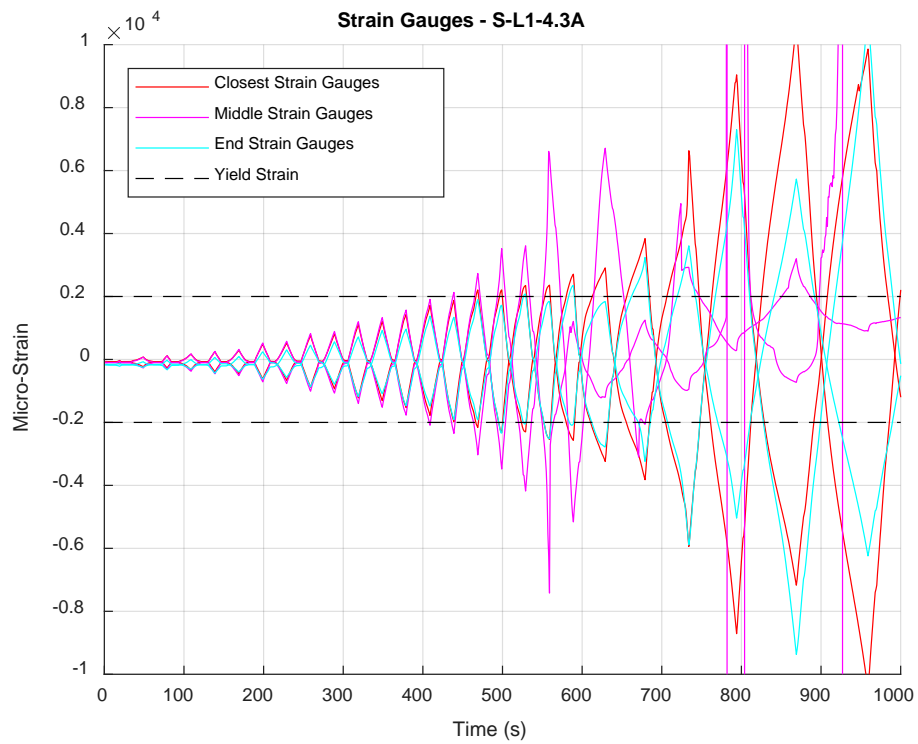
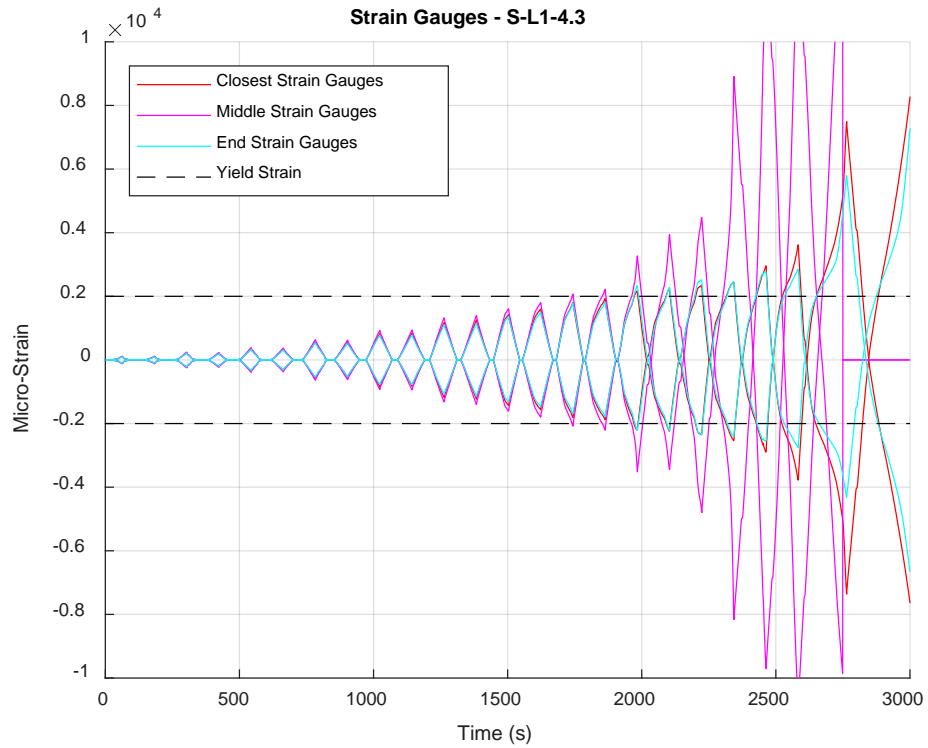


Figure 83 - SG Data for S-L1-4.3 and S-L1-4.3A

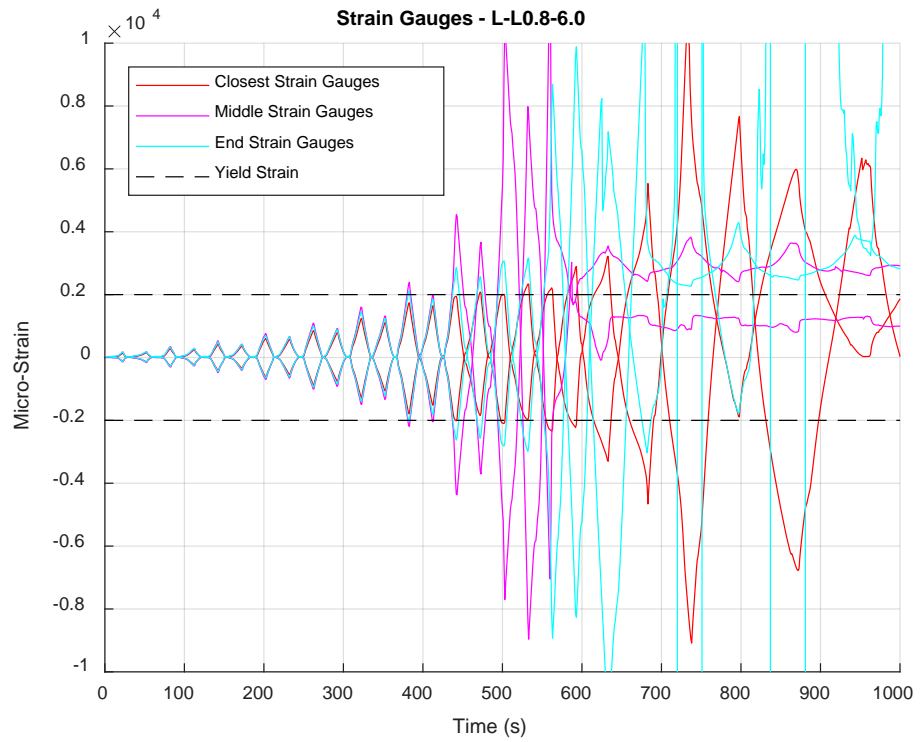


Figure 84 - SG Data for L-L0.8-6.0

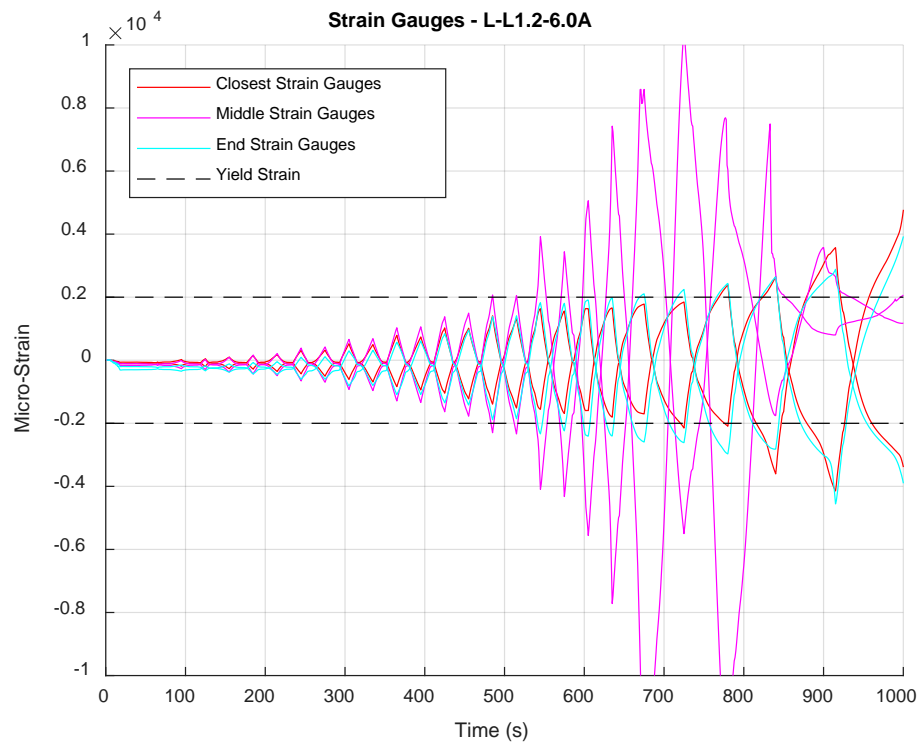
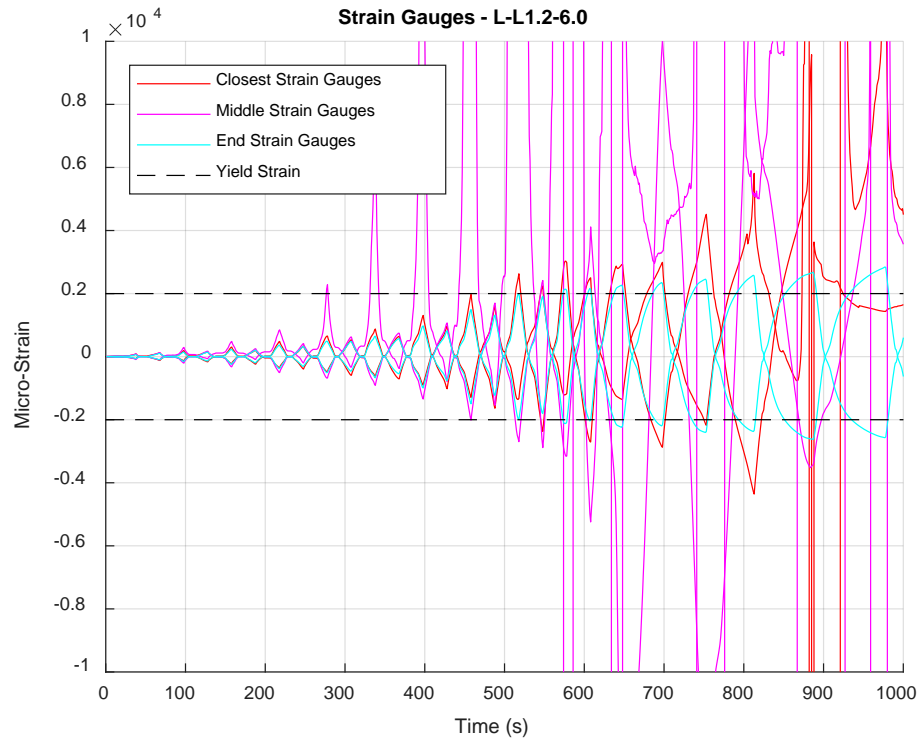


Figure 85 - SG Data for L-L1.2-6.0 and L-L1.2-6.0A

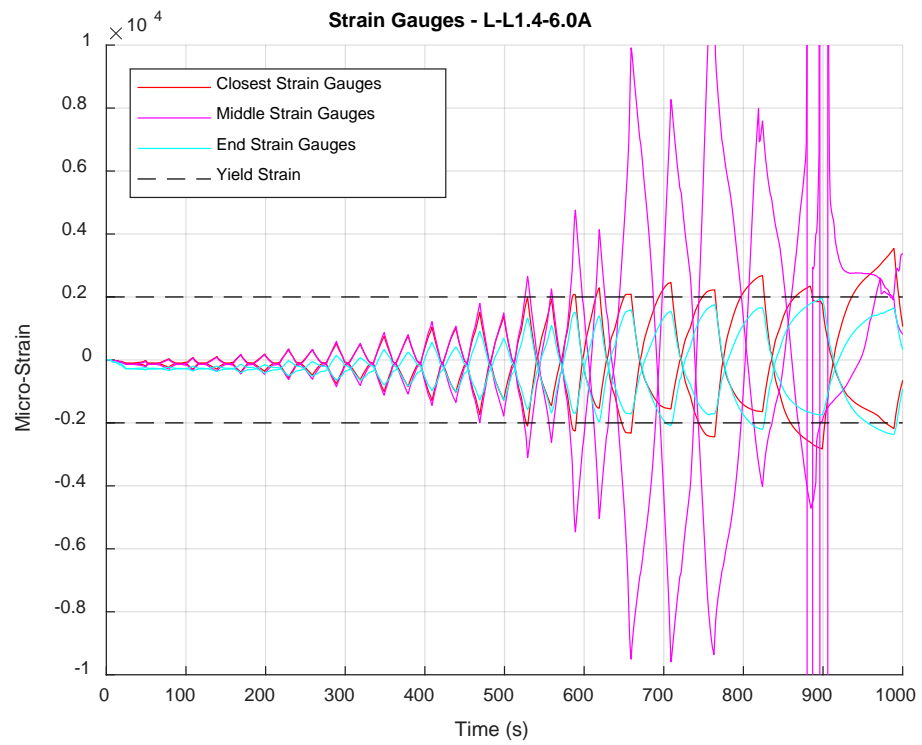
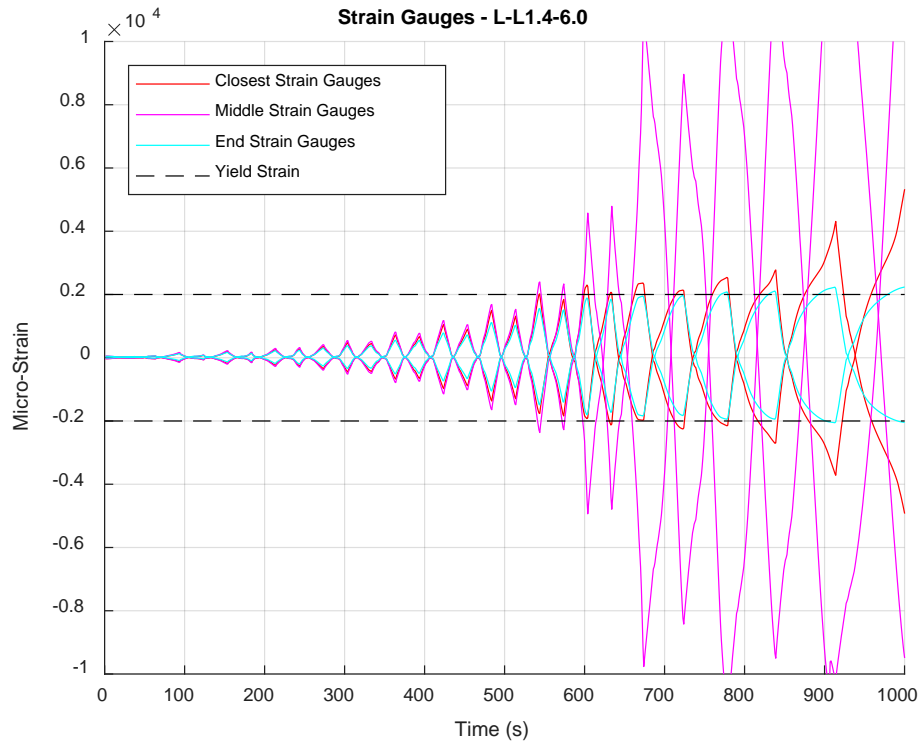


Figure 86 - SG Data for L-L1.4-6.0 and L-L1.4-6.0A

Appendix F – Sample Derivations – Phase I

$$\sigma(x) = \frac{M(x) w(x)/2}{I(x)} = \frac{\left(M_o \frac{x}{L}\right) \left(\frac{(b-a)x}{L} + a\right)/2}{\frac{1}{12} \left(\left(\frac{(b-a)x}{L} + a\right)^3 t\right)}$$

$$\sigma(x) = \frac{6 M_o}{L t} \frac{x}{\left(a - \frac{x(a-b)}{L}\right)^2}$$

- Detail plastic hinge to be away from location of curvature change, $x = 0$, $x = L$.
- Find location and magnitude of maximum bending stress

$$\frac{\partial \sigma(x)}{\partial x} = \frac{\partial \left[\frac{x}{\left(a - \frac{x(a-b)}{L}\right)^2} \right]}{\partial x} = 0;$$

$$x = \frac{-a L}{a - b}$$

- If $x = L/2$, then $a/b = 1/3$
- Sub $x = L/2$ into $\sigma(x)$ to get

$$\sigma_{max} = \frac{3 M_o}{2 (b - a) a t} = \sigma$$

- At yield

$$M_o = M_y = Q_{yt} L = \frac{2 (b - a) a t}{3} \sigma_y$$

- Re-arrange to get

$$Q_{yt} = \frac{2 (b - a) a t}{3 L} \sigma_y$$

- Sub $a/b = 1/3$

$$Q_{yt} = \frac{4}{27} \frac{b^2 t \sigma_y}{L}$$

- Based on assumption that $M_p = 1.5 M_y = (bh^2/4) \sigma_y$

$$Q_{pt} = 1.5 Q_{yt} = \frac{6}{27} \frac{b^2 t \sigma_y}{L}$$

Appendix G – Sample Derivations – Phase II

$$\sigma(x) = \frac{M(x) w(x)/2}{I(x)} + \frac{P}{w(x) t}$$

$$\sigma(x) = \frac{\left(\frac{M_o x}{L}\right) \left(\frac{(b-a)x}{L} + a\right)/2}{\frac{1}{12} \left(\left(\frac{(b-a)x}{L} + a\right)^3 t\right)} + \frac{P}{\left(\frac{(b-a)x}{L} + a\right) t}$$

- Detail plastic hinge to be away from location of curvature change, $x = 0$, $x = L$.
- Find location and magnitude of maximum bending stress

$$\frac{\partial \sigma(x)}{\partial x} = 0;$$

- Assume same as before since the new expression becomes difficult to derive symbolically. The compression stress also accounts for only 5% to 9% of total yield stress in the cases presented in this thesis.

$$x = \frac{-a L}{a - b}$$

- If $x = L/2$, then $a/b = 1/3$
- Sub $x = L/2$ into $\sigma(x)$ to get

$$\sigma_{max} = \frac{3 M_o}{2 (b - a) a t} + \frac{2 P}{(a + b) t} = \sigma$$

- At yield and account for axial contributions to moment but neglecting the axial stress term for simplification and because it is relatively small.

$$M_o = M_{y,a} = Q_{yt,a} L + P \Delta_y = \frac{2 (b - a) a t}{3} \sigma_y$$

- Re-arrange to get

$$Q_{yt,a} = \frac{2 (b - a) a t}{3 L} \sigma_y - \frac{P \Delta_y}{L}$$

- Sub $a/b = 1/3$

$$Q_{yt,a} = \frac{4}{27} \frac{b^2 t \sigma_y}{L} - \frac{P \Delta_y}{L}$$

- Based on assumption that $M_p = 1.5 M_y = (bh^2/4) \sigma_y$

$$Q_{pt,a} = 1.5 Q_{yt,a} = \frac{6}{27} \frac{b^2 t \sigma_y}{L} - \frac{P 1.5 \Delta_y}{L}$$

Appendix H – Full Cyclic FEA Hysteresis Loops

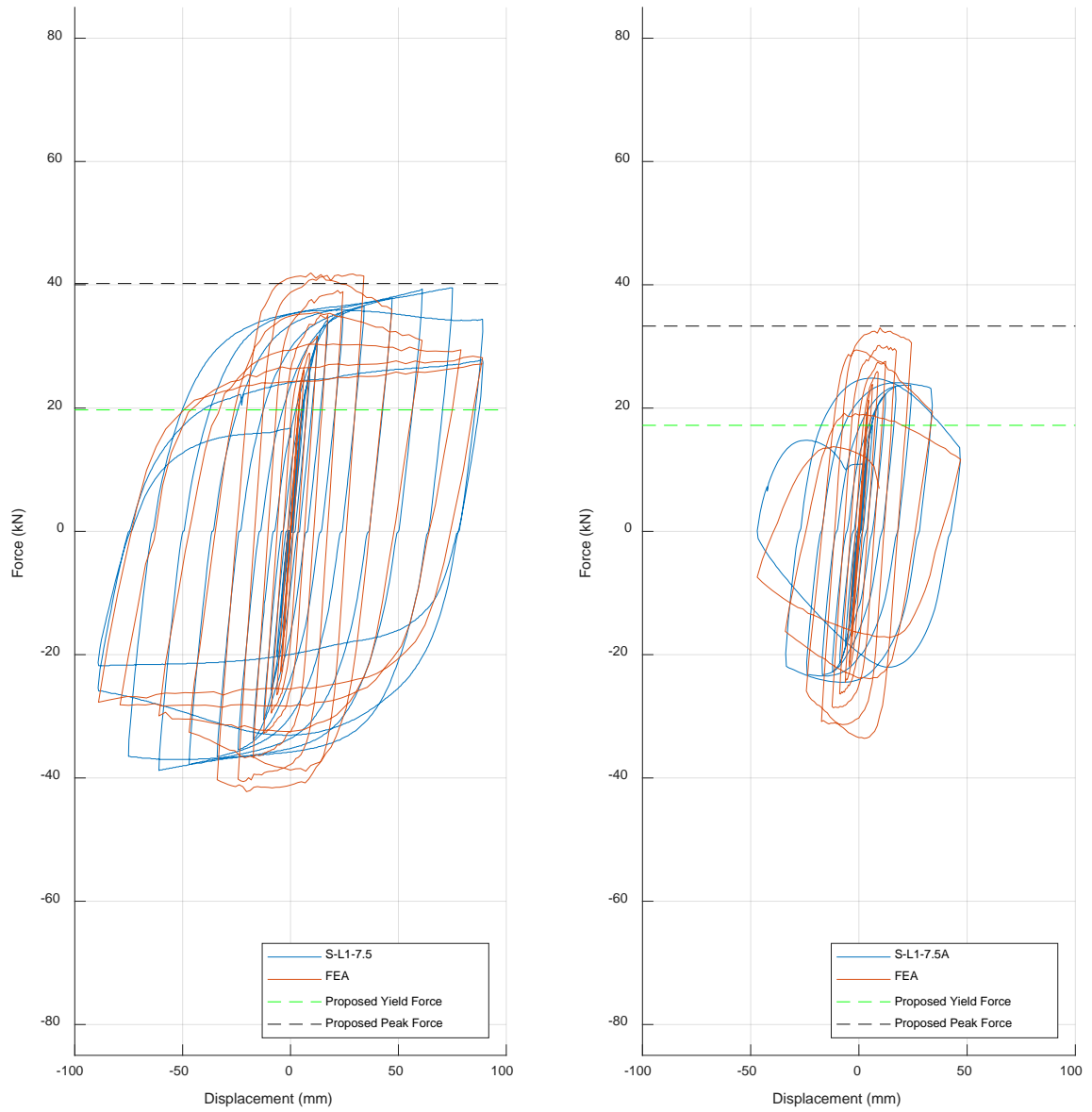


Figure 87 - Hysteresis Plots for S-L1-7.5 and S-L1-7.5A

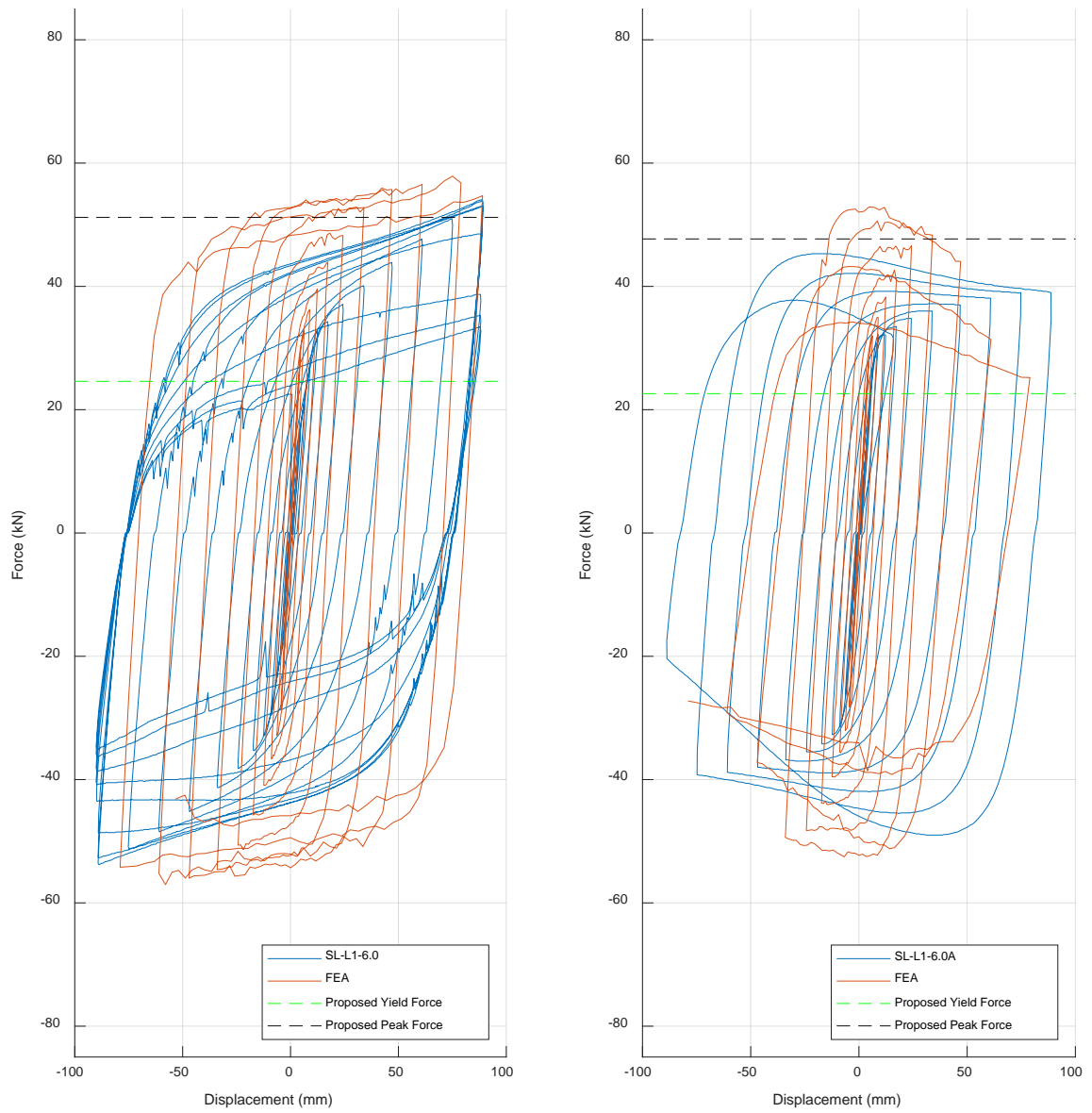


Figure 88 - Hysteresis Plots for SL-L1-6.0 and SL-L1-6.0A

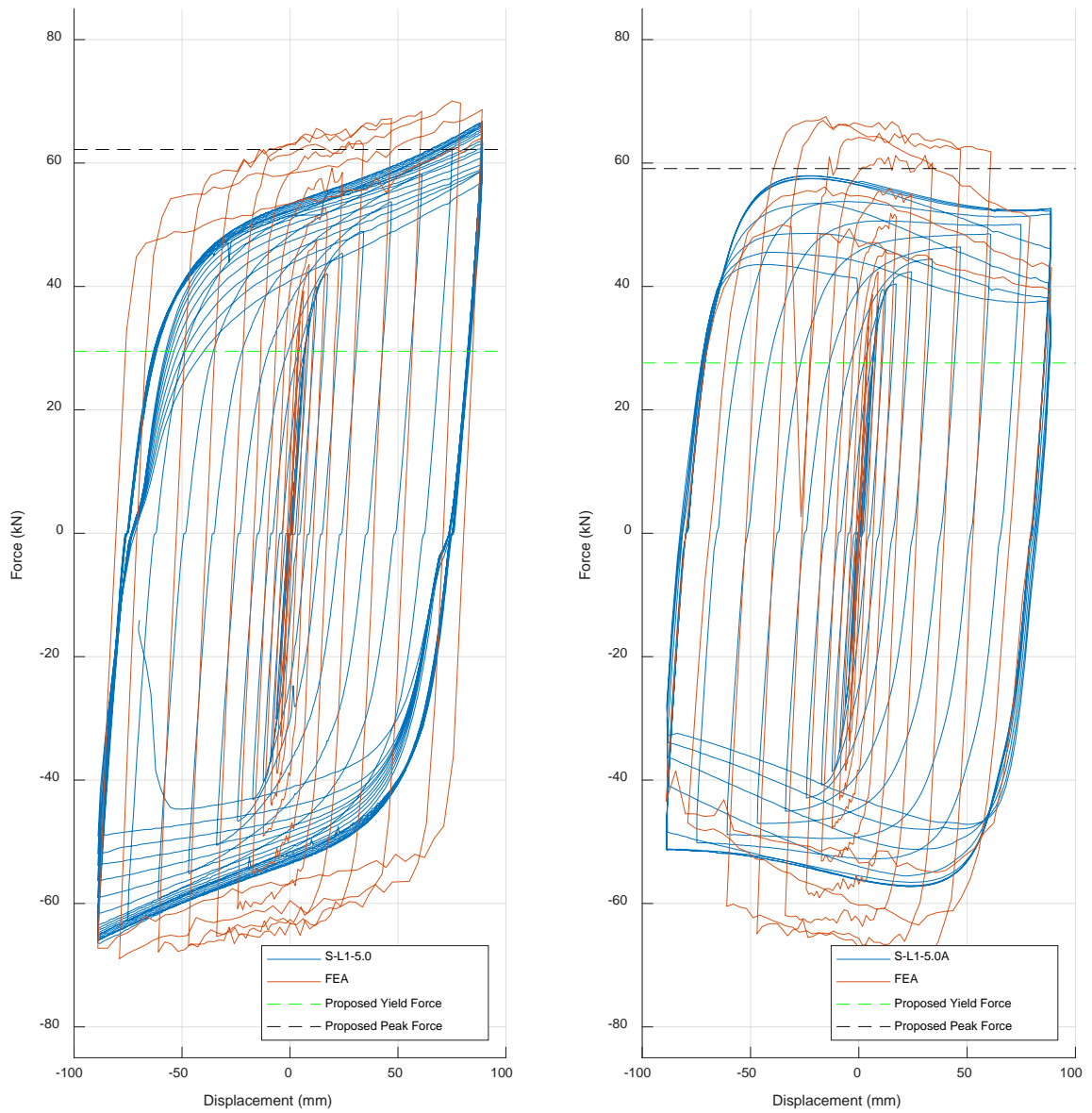


Figure 89 - Hysteresis Plots for S-L1-5 and S-L1-5A

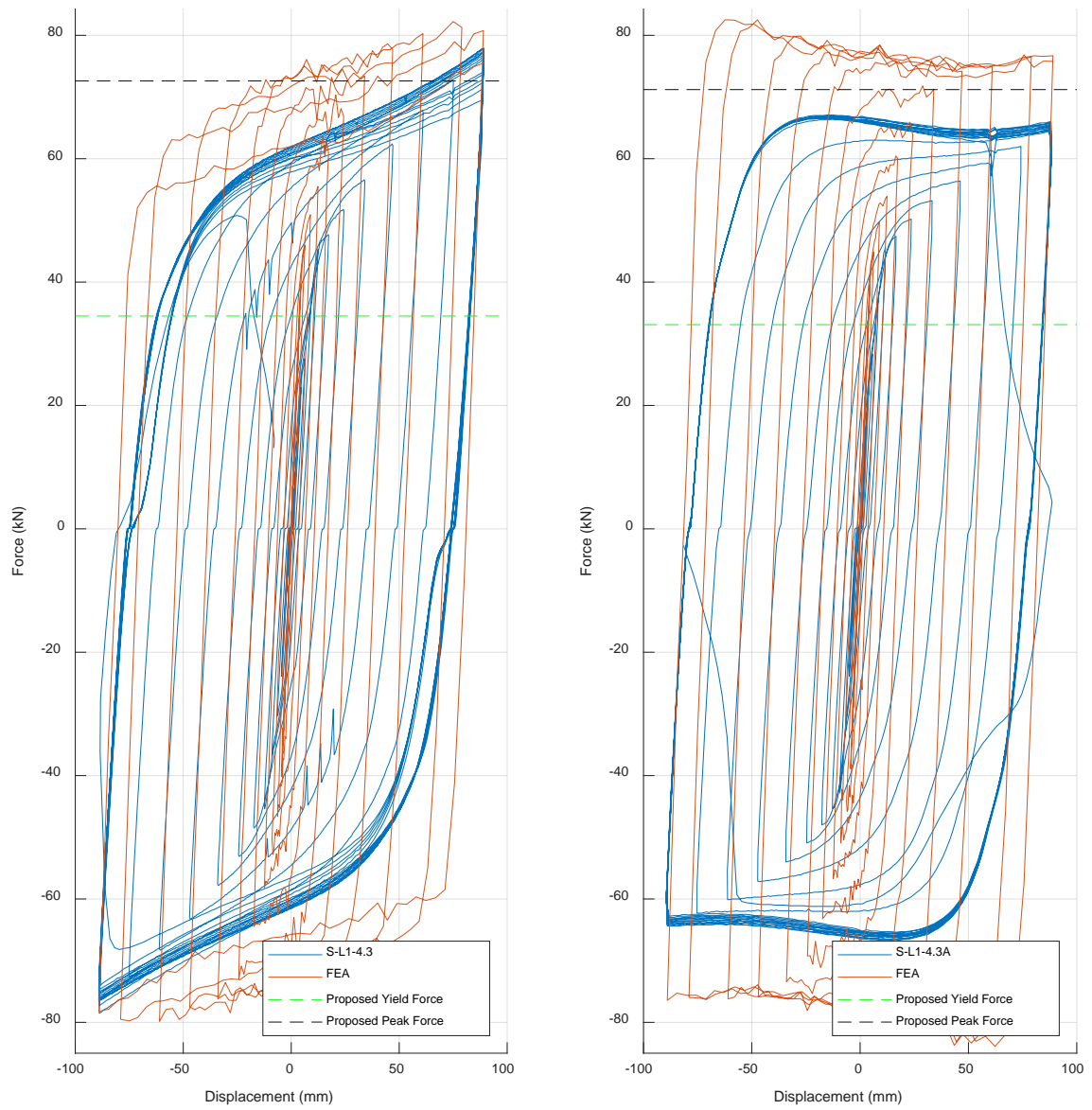


Figure 90 - Hysteresis Plots for S-L1-4.3 and S-L1-4.3A

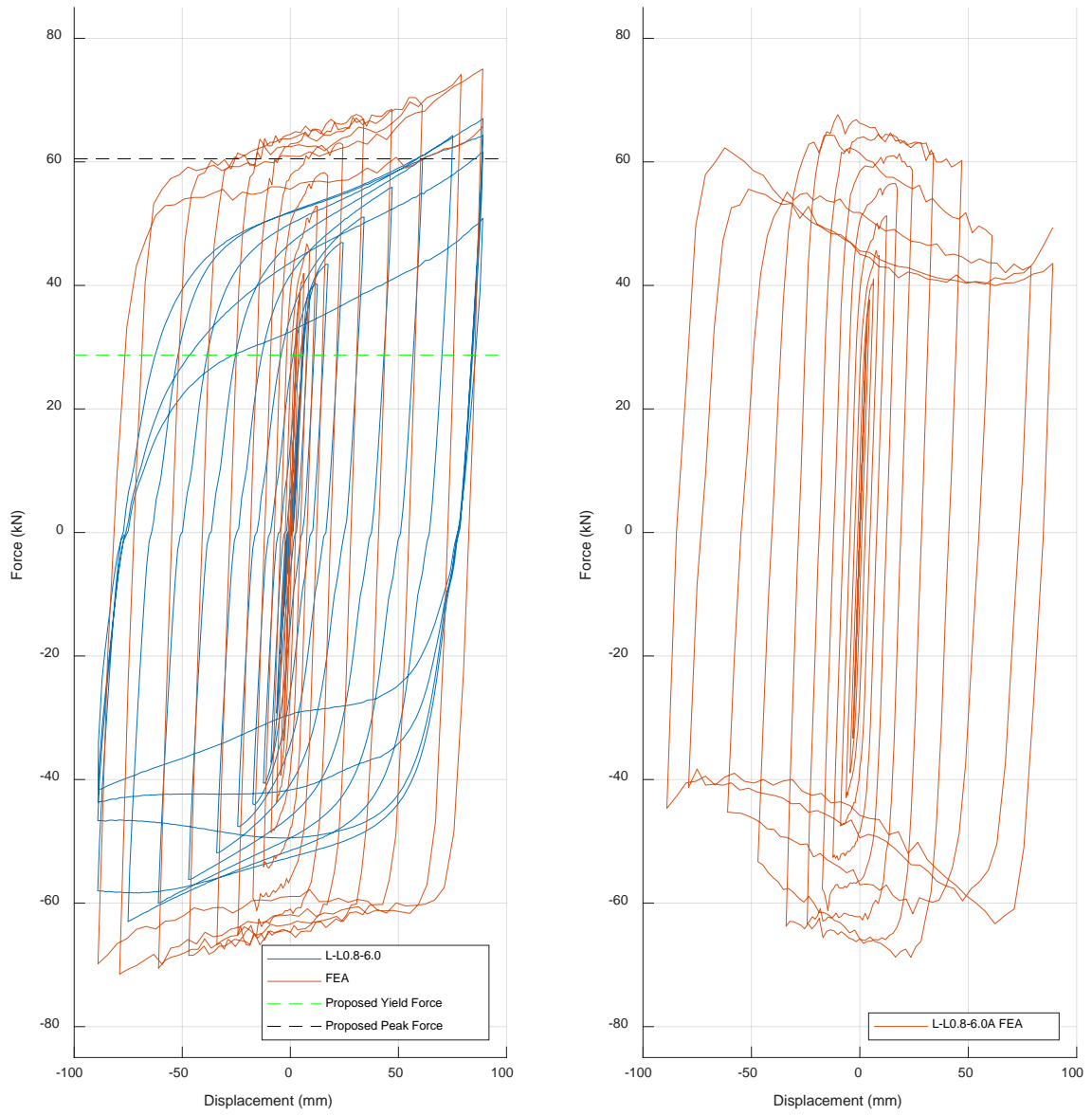


Figure 91 - Hysteresis Plots for L-L0.8-6.0 and L-L0.8-6.0A

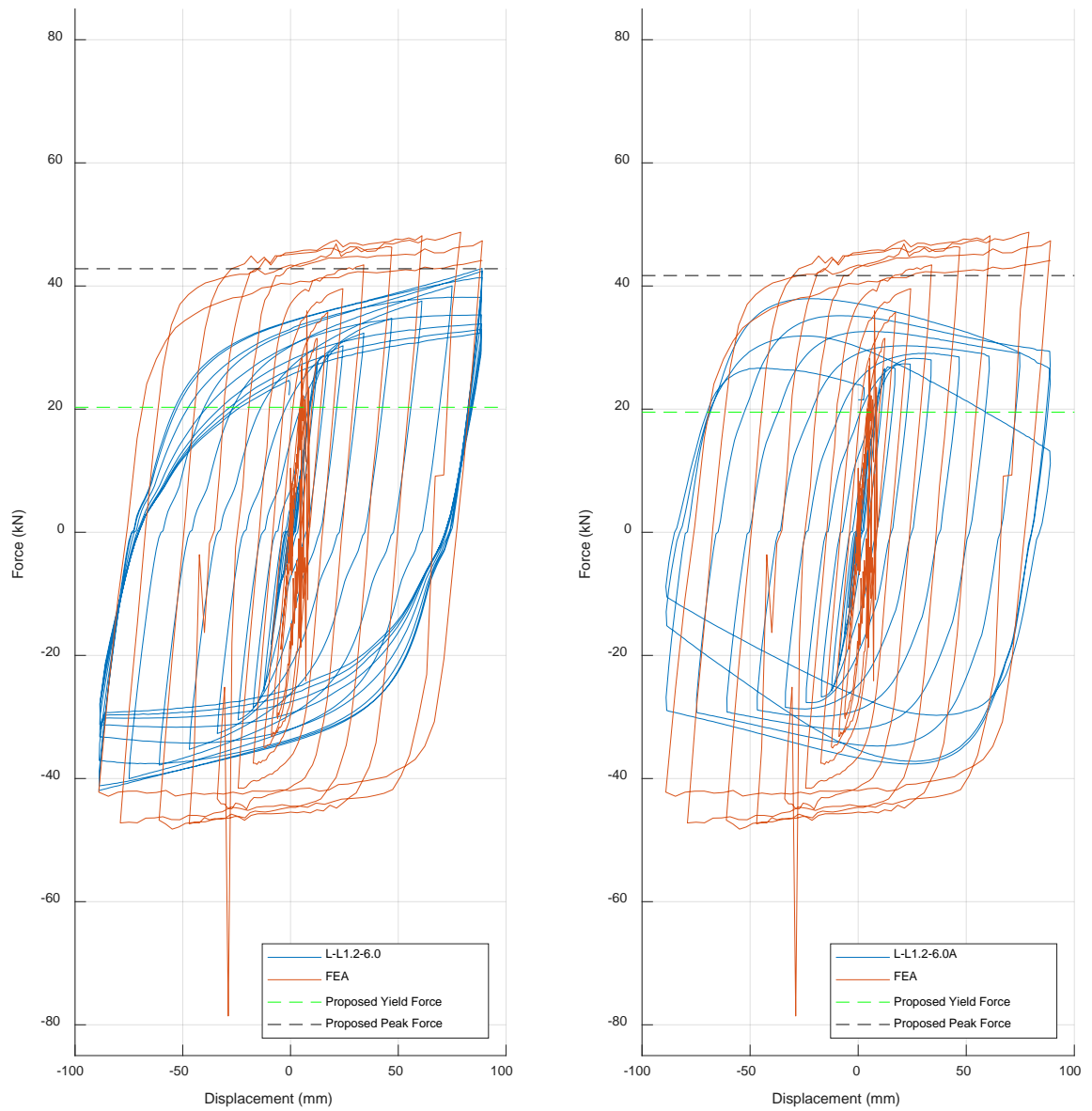


Figure 92 - Hysteresis Plots for L-L1.2-6.0 and L-L1.2-6.0A

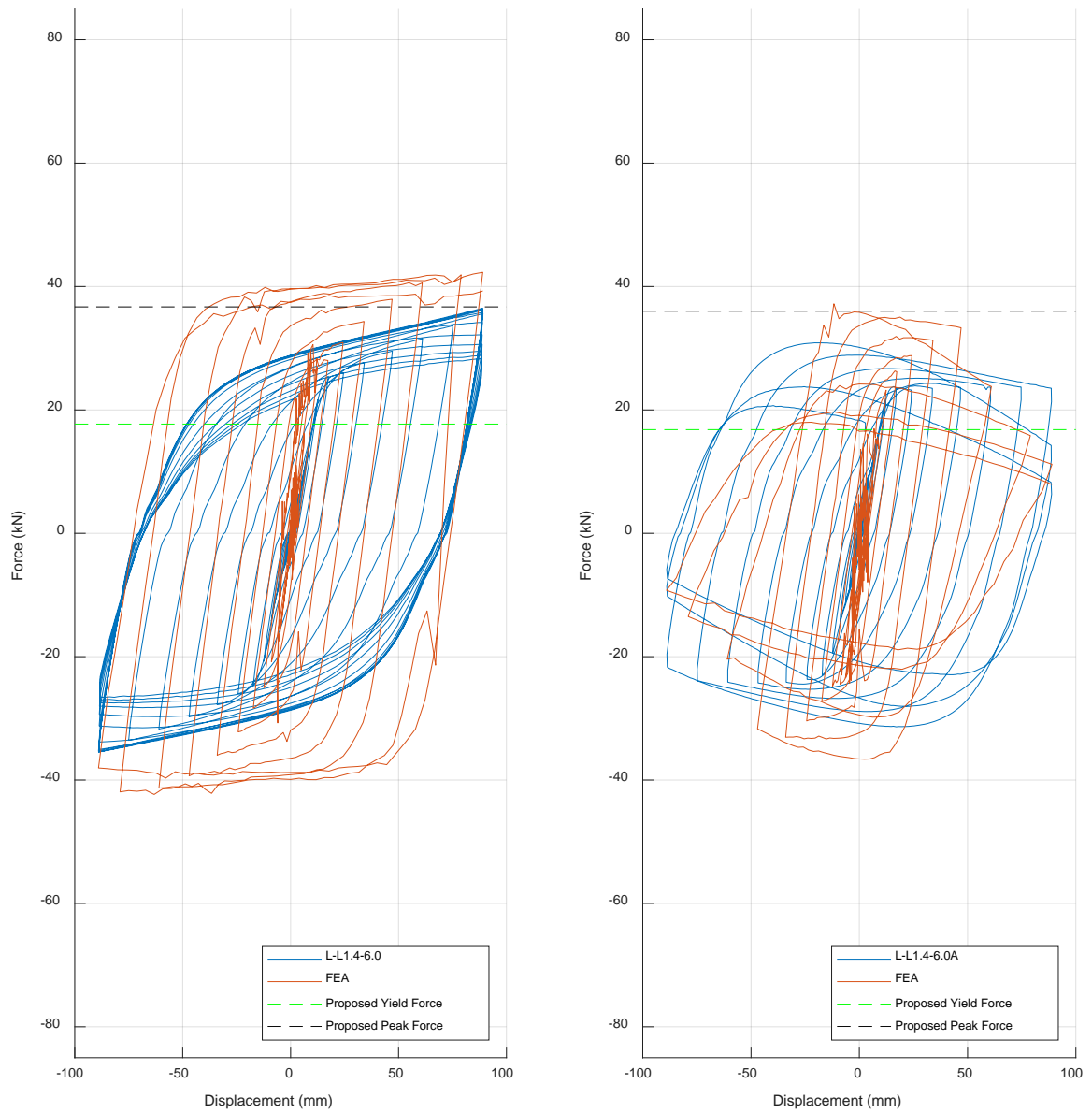


Figure 93 - Hysteresis Plots for L-L1.4-6.0 and L-L1.4-6.0A

Appendix I – Numerical Approximate of the *Phase II* Yield Location

Eq. (6) was plotted for the specimen SL-L1-6.0A in Fig. 94. The damage sequence for this specimen was shown in Fig. 20. The orange line in Fig. 94 shows the location of maximum bending stress obtained through Eq. (6) and corresponds to $x = 0.54L$, while the green line shows the location of maximum bending stress if the considered length was increased from L to h which moves the location closer to $x = 0.06L$. The true location of yield initiation seen in Fig. 94 is roughly $x = 0.67L$. This shows that the approximate method and simplified assumptions used in *Phase II* (described in Appendix G) were inaccurate in determining the location of intended yield initiation and therefore more careful efforts must be placed in the derivation procedures, as discussed in Section 6.5.

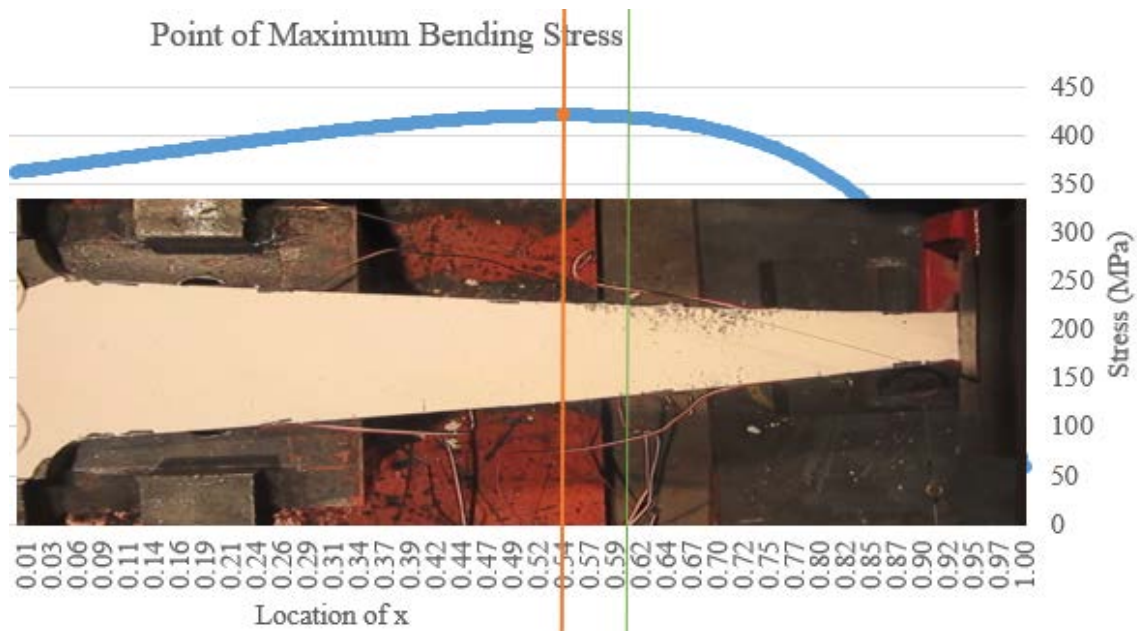


Figure 94 - Approximate Plot of Location of Maximum Bending Stress